Faculty of Maritime Studies
University of Rijeka, Croatia

University of Zagreb
Faculty of Transport
and Traffic Sciences

Royal Institute of Navigation
Science Technology Practice

ISSN 1849-7306

9th Annual Baška GNSS Conference

PROCEEDINGS

Baška, Krk Island, Croatia
10 – 12 May 2015

ISSN 1849-7306

9th Annual Baška GNSS Conference

PROCEEDINGS

Baška, Krk Island, Croatia
10 – 12 May 2015

Published by:
University of Rijeka, Faculty of Maritime Studies Rijeka, Rijeka, Croatia
The Royal Institute of Navigation, London, UK

For the Publisher:
Full Professor Serdjo Kos, Ph. D., FRIN, Faculty of Maritime Studies Rijeka

Publishing Associates:
Captain J.B. Taylor, OBE RN, President, The Royal Institute of Navigation
Capt. Peter Chapman-Andrews, LVO MBE RN, Director, The Royal Institute of Navigation

Editor-in-Chief:
Full Professor Serdjo Kos, Ph. D., FRIN, Faculty of Maritime Studies Rijeka
Associate Professor Renato Filjar, Ph. D., FRIN, Faculty of Maritime Studies Rijeka

Executive Editor:
Marija Šimić Hlača B. Sc., Faculty of Maritime Studies Rijeka

Front-page photo credits:
Associate Professor Renato Filjar, Ph. D., FRIN, Faculty of Maritime Studies Rijeka

Text Formatting:
Tempora, Rijeka

Print:
AKD d.o.o. Zagreb

Address:
Faculty of Maritime Studies Rijeka
Studentska 2
51000 Rijeka
Croatia
Tel: +385 (0)51 338 411
Fax: +385 (0)51 336 755
URL: http://www.pfri.uniri.hr/
E-mail: dekanat@pfri.hr

ISSN 1849-7306

CONTENTS

Faculty of Maritime Studies
University of Rijeka, Croatia

University of Zagreb
Faculty of Transport
and Traffic Sciences

Royal Institute of Navigation
Science Technology Practice

9th Annual Baška GNSS Conference

PROCEEDINGS

Faculty of Maritime Studies
University of Rijeka, Croatia

University of Zagreb
Faculty of Transport
and Traffic Sciences

Royal Institute of Navigation
Science Technology Practice

9th
Annual
Baška GNSS
Conference

CITIZEN SCIENCE FOR GNSS PERFORMANCE MONITORING AND ASSESSMENT

Renato Filjar[1], Nenad Sikirica[2], Renato Alves Borges[3]

[1] Faculty of Maritime Studies, University of Rijeka, Rijeka, Croatia
E-mail: renato.filjar@gmail.com

[2] Polytechnic Hrvatsko Zagorje Krapina, Krapina, Croatia

[3] University of Brasilia, Brasilia, Brazil

ABSTRACT. *Citizen Science is a new form of voluntary involvement of lay-individuals in collection of data (observables) with potential of providing new scientific or engineering insight into and understanding of observed processes. With technology becoming more affordable, the lay-individuals around the world increasingly donate money, effort and time in collecting data with potential of later scientific or engineering analysis. Two case scenarios (of the observation processes conducted by amateur meteorologists and ham radio operators) are presented in order to illustrate the potentials, benefits and pitfalls of such activities. Here the Citizen Science approach is proposed as a partial solution for a chronic lack of field data desperately needed for targeted analysis of GNSS performance monitoring and assessment for a number of GNSS-based applications (the mobile ones in particular) that require Quality of Service established by GNSS performance. An honest account of reasonable expectations from such an activity is given, along with the methods and techniques for data cleaning from measurement noise and error, and open-source software-based data processing. Finally, a call for an initiative for a UN ICG-backed international co-operation on establishing standardised procedures for GNSS Citizen Science data collection, storage (with open access), processing and interpretation is presented, with the aim to provide researchers, engineers, business developers, regulators and general public with a framework for impartial GNSS performance assessment based on field data.*

KEY WORDS: *citizen science, GNSS performance, recommendations, GNSS applications*

1 INTRODUCTION AND MOTIVATION

The increasing number of GNSS applications accross numerous disciplines causes the growing need for GNSS performance assessment in various environments of potential GNSS-based applications [Thomas *et al*, 2011], [Filjar, Desic, and Huljenic, 2004]. Along with the community of professionals actively engaged on the subject, a community of volunteers, both laymen and professionals, emerges, with intention for and interest in collection of valuable GNSS positioning experimental data. In addition, software tools and systems for data science (data statistics and analytics) have become wide-spread and available (either as open-source or commercial alternatives), along with the novel information- and communication technology (ICT) frameworks that allow for collection, aggregation, storage and access to large data sets (cloud services – computing, cloud storage, parallel computing, Internet of Things – IoT, mobile internet etc.) [Nature editorial, 2015], [Crawley, 2013].

Citizen Science (CS) concept [Nature editorial, 2015], [Vetter, 2011], a process in which both laymen and professionals voluntary engage in collection of observation data related to research subject in systematic manner and with the established data qaulity, may be at hand to assist in bridging the gap [Vetter, 2011], [Alabri and Hunter, 2010], [Stevens, 2014]. Here we present a framework for citizen science approach in GNSS data collection, thus establishing the foundation for better understanding of GNSS positioning performance in various use-case scenarios and assessment its impact on quality of service of GNSS-based applications.

The paper is structured as follows. Chapter 2 outlines the problem, and present a brief overview of existing solutions to it. Chapter 3 addresses deployment of the citizen science concept for GNSS observations collection. Chapter 4 discusses the advantages and shortcomings of the citizen science-based GNSS data collection, and outlines common practice recommendations. The paper concludes with conclusion and guidelines for future work, in Chapter 5.

2 PROBLEM DESCRIPTION

Lack of data (raw GNSS observations/position estimates) in various positioning environments limits the accuracy of the GNSS-based applications quality of service definition and assessment [Thomas *et al*, 2011]. Determination of position environment's effects on GNSS-based application's QoS is traditionally based on synergy of various related error models the GNSS application designer presume relevant. Here, the experience and knowledge may produce a more or less QoS

assessment estimate, but robust QoS definition and assessment for many possible application scenarios is deprieved by inability to invoke the effects of the real environment [Petovello, 2015].

Still, the characterisation of positioning environments has advanced recently, growing the pool of knowledge that may assist in the solution of the problem. The technologies in assistance to the knowledge development are briefly presented in the rest of the chapter [Stevens, 2014], [James *et al*, 2014].

2.1 Data science is a discipline targeting hidden and not so obvious knowledge in systems and processes [James *et al*, 2014]. Through data science deplyoment, the statistics inference and statistical learning methods, techniques and tools are applied on the large data sets in order to extract non-apparent patterns, relationships and knowledge about observed process in general [Maindonald and Brown, 2010], [James *et al*, 2014]. Data science deploys data mining concept, an iterative process, presented in Fig 1.

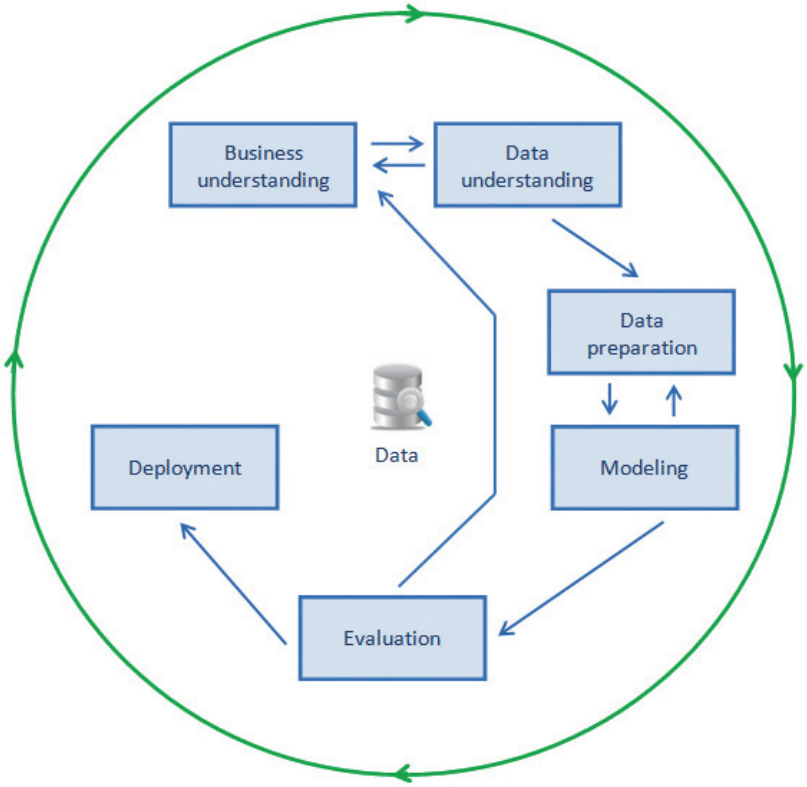

Figure 1 Data science/mining process

2.2 GNSS application development process comprises various development phases [James *et al*, 2014], [Petrovski, 2014], as follows:

– requirements specification,

– definition of users/stakeholders,

– establishment of typical use-case scenatios

– the choice of technolgy to be deployed in the application development,

– definition of the quality of service (including Key Performance Indicators – KPIs), and

– the outcomes of the application provision.

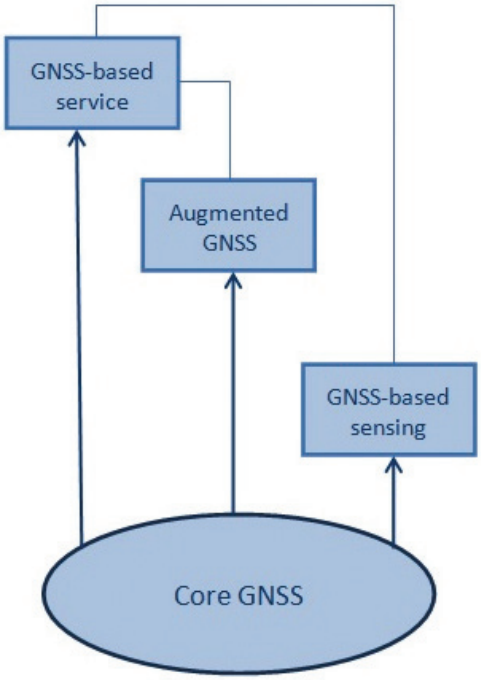

Figure 2 GNSS application development process

The GNSS-based application development process (Fig 2) utilises the core GNSS system for the essential GNSS-based service provision (position, velocity and time estimation based on observations), while the utilisation of the augmented GNSS (additional assistance in clearing the observations from naural and artificial errors) and GNSS-based sensing (reverse engineered utilisation of GNSS not for position

estimation, but for the environment sensing) contribute to the improvement of the essential GNSS-based service [Petrovski, 2014].

2.3 Lack of experimental data. Lack of geographically well-distributed GNSS observations taken in different positioning environments and for different use-case scenarios is a variation of an old problem [Hughes and Hase, 2010]. Analogy can be found in various disciplines, one of them being the weather forecasting data problem [Vasquez, 1998], [Maindonal and Brown, 2010]. Despite a line of good forecasting methods at hand and the respectable computing power available, weather forecasting will fail utterly if the weather parameter observations lack sufficient granularity.

The GNSS systems, such as GPS, utilise the global network of observing stations, as depicted in Fig 3, but with the different aim of operating the core system [Petrovski, 2014], [Sanz Subirana *et al*, 2011]. The GNSS-based application developers require more data related to the expected user equipment, ionospheric dynamics and the effects of local geography [Sanz Subirana *et al*, 2011]. Due to a huge diversity of GNSS applications, large variations of QoS requirements for GNSS applications emerge, especially for those of mobile nature [Filjar, Desic and Huljenic, 2004]. Noise and interference present additional problem, that is hard to resolve by modelling and simulations [Hohnson and Setares, 2003], [Petrovski, 2014]. Facing the choice between the utilisation of a well-populated low-cost sensors network [Filjar, Kos, and Kos, 2010] and sparse and expensive high-quality sensors, the former brings better value for GNSS application developers.

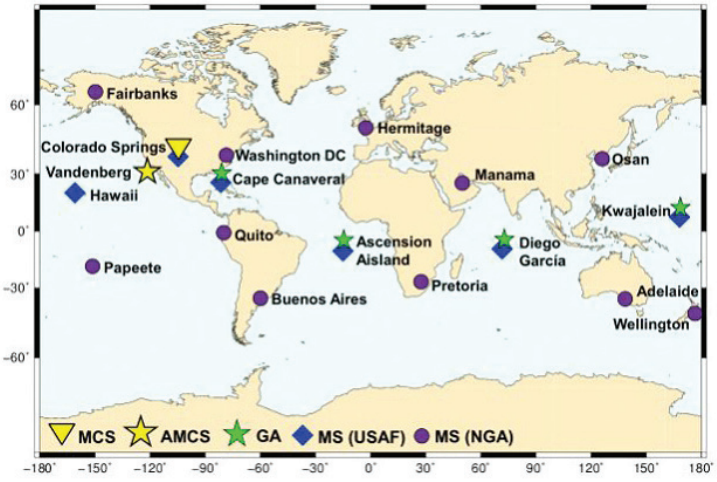

Figure 3 Global network of GPS control segment reference stations – less is not more, actually

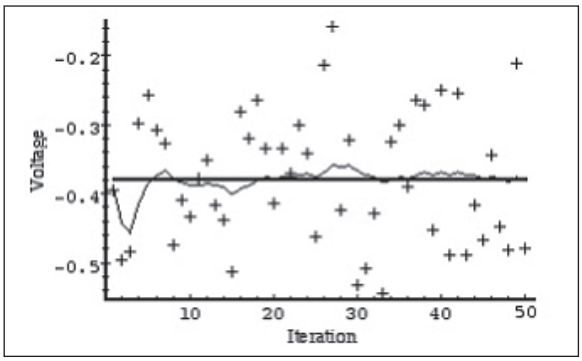

Figure 4 Noise-polluted data still brings information – voltage [mV] measurements in noisy environment taken with 1 s-interval

2.4 Good practices in other disciplines. Citizen science concept is successful in many scientific disciplines, ranging from radiometeorology [Frissell *et al*, 2014], and meteorology and climate, to space science and biology [Nature editorial, 2015]. It deploys a network of low-cost sensors, thus improving geographical distribution of data collection, with essentially continuous monitoring [Rembovski *et al*, 2009]. The collected observations area noisier and of lower quality than with the high-quality and expensive sensors (Fig 4), but provide better spatial granularity, thus improving the understanding of the observed processes.

Finally, data cleaning and filtering may successfuly remove majority of unwanted effects, revealing the information necessary for proper and successful GNSS application's QoS definition [Alabri and Hunter, 2010], [Maindonald and Brown, 2010].

Even disciplines closely related to GNSS operation, such as solar physics, physics of the ionosphere [Frissell *et al*, 2014], geomagnetic physics, meteorology and transport (Fig 5) utilise citizen science concept and offer internet-based open-access repositories for data storage and usage. The examples of a good practices are, as follows:

– International GNSS Service (IGS) (available at: http://www.igs.org/),
– Intermagnet (available at: http://www.intermagnet.org/index-eng.php),
– Space weather & ionospheric data: SPIDR (NOAA, US) (available at: http://spidr.ngdc.noaa.gov/spidr/),
– ESA SSA Space Weather Co-ordination Centre (available at: http://swe.ssa.esa.int/web/guest/service-centre), and

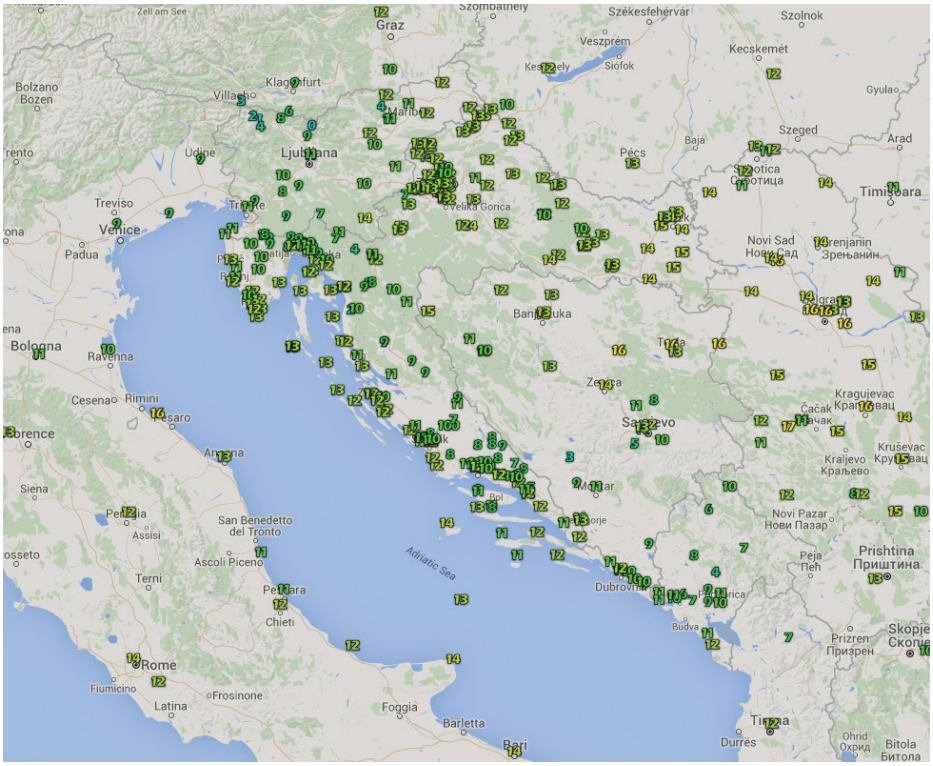

Figure 5 pljusak.com, a Croatian portal for aggregation and visualisation of crowdsorced (citizen-science) meteorological (shown) and traffic (ADS-B and AIS) observations

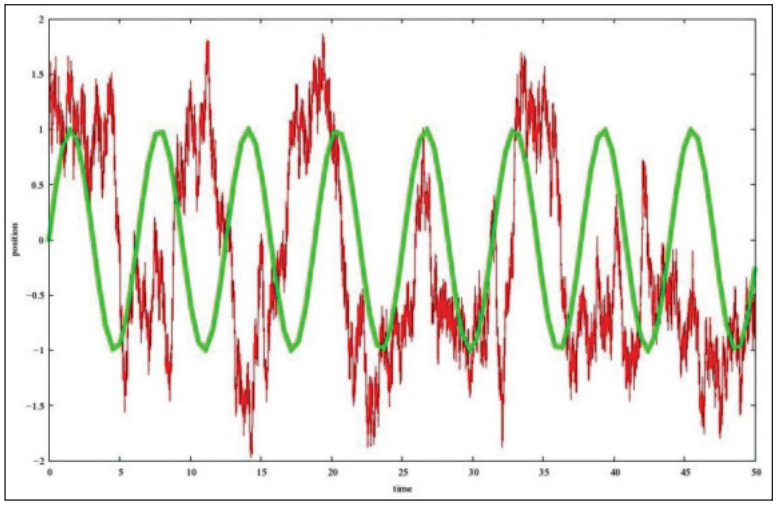

Figure 6 Data cleaning and knowledge extraction algorithms are the components of knowledge extraction process that yield the information (green) from a composite signal (red) polluted by noise and modified by the effets of non-linear systems

– Royal Observatory of Belgium, GNSS Research Group (available at: http://www.gnss.be/Atmospheric_Maps/ionospheric_maps.php)

3 CITIZEN SCINECE CONCPET FOR GNSS PERFORMANCE MONITORING AND ASSESSMENT

Here an approach in GNSS observables collection by volunteers (both laymen and professionals) in compliance with the minimum standards for experimental design, (commercial-grade) equipment utilisation, and quality of collected data is addressed with the aim to establish an open-access database of raw GNSS observations for characterisation of positioning environment, and definition and validation of the appropriate GNSS-based application QoS. Data sets collection, aggregation, cleaning, sorting and storing in standardised formats, with the open access to scientists, engineers, and technology-, strategy-, policy-, and business-developers is facilitated in order the same standards of data collection and management quality and avoid systemic errors and biases.

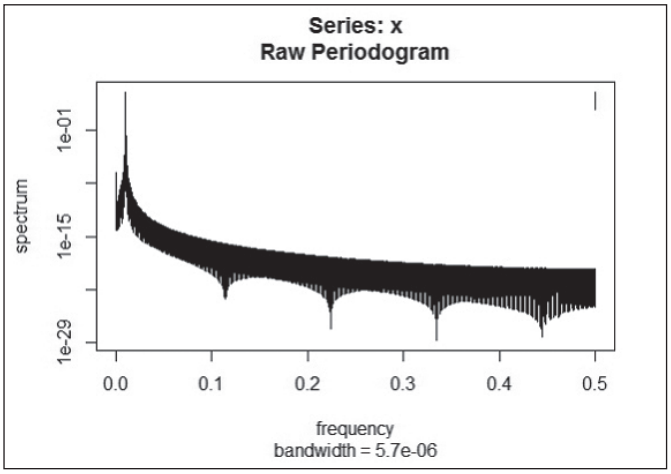

Figure 7 Spectral characterisation as a useful tool for information extraction – a case of AM signal presented against the relative frequency $f/f_{sampling}$

Based on the pool of collected data sets, the advanced services, such as the statistical analysis (Fig 7), error correction and modelling, or assessment of the effect of PNT environment (effects of the ionosphere, multipath etc.) may be offered to interesting parties, thus covering the costs of the system operation [Navipedia, 2016], [Peng, 2015], [Maindonald and Brown, 2010], [Petrovski, 2014]. Finally, the research in

methodology of GNSS data processing and utilisation of some advanced concept in signal processing and data modelling, such as stochastic resonance, may be turned into benefit for the GNSS performance assessment.

4 DISCUSSION

A common practice procedure is essential for framework establishment for useful GNSS observations collection and analysis. The common practices procedure is outlined in this chapter through a set of recommendations.

Still, the citizen science approach in collection of GNSS observations is exposed to a number of deplyoment challenges, addressed in this chapter as well.

4.1 Common practice recommendations

4.1.1 Establishment of the observation standards for Citizen Science-based GNSS performance monitoring and assessment.

4.1.2 Establishment of a catalogue/database of use-cases per targeted classes of applications (navigation: air, maritime, road, personal; non-navigation: ITS, LBS, timing and synchronisation, emergency services, agronomy and forestry etc.).

4.1.3 Setting standards for data collection based on best practices (IGS) and characteristics of commercial-grade equipment.

4.1.4 Setting standards for data storage, organise it, and operate it with the open-access principle deployed.

4.1.5 Setting standards for data access (incl. common data formats, data and system protection).

4.1.6 Setting standard procedures for data cleaning and error correction (where required).

4.1.7 Advising on and recommending the GNSS data processing methodology.

4.1.8 Facilitating international co-operation and data analysis results exchange.

4.2 Deployment challenges

Deployment of the citizen science approach in GNSS observations collection faces technology and organisational challenges. Technology challenges encompas:

– categorisation of different positioning environments,

– categorisation of GNSS-based applications (both navigational and non-navigational),
– challenges related to data and services hosting,
– standardisation of GNSS data collection procedures (incl. recommendation for GNSS equipment commonly used for GNSS applications in consideration),
– definition of GNSS data cleaning and normalisation methodology,
– challenges of GNSS data storage, and GNSS data access,
– methodology definition for GNSS data processing, and error corrections, modelling and processing, that will preserve the information on positioning environment but reduce the unwanted impact of measurement process, and
– data and system protection.

The organisational challenges comprise:

– Project management
– Reliable funding, and
– Definition of the means of co-operation.

Considering the expected world-wide interest among data providers and data users, and the importance of data for GNSS-based application developments, a co-ordination of the project by the UN International Committee on GNSS, with support given by core GNSS system operators and GNSS receiver manufacturers can be considered an over-all framework for establishing an open-access database of GNSS observables

5 CONCLUSION AND FUTURE WORK

GNSS operation and GNSS-based services increasingly requires knowledge of GNSS PNT performance in various deployment environments and conditions. An initiative is presented to establish a scientific & engineering – grade database of citizen science experimental observations to be used for GNSS PNT performance assessment in various conditions and environments, thus facilitating responsible, elegant and QoS-guaranteed GNSS-based applications development. The initiative as an international co-operation effort that yields the system and reliable data accessible openly.

REFERENCES

[1] Alabri, A and Hunter, J. (2010). Enhancing the Quality and Trust of Citizen Science Data. *Proc of 2010 Sixth International Conference on e-Science* (8 pages).

[2] Crawley, M.J. (2013). The R Book. John Wiley & Sons, Ltd. Chichester, UK.

[3] Filjar, R, Desic, S, and Huljenic, D. (2004). Satellite Positioning for LBS: A Zagreb Field Positioning Performance Study. *J of Navigation*, **57**, 441–447. doi: 10.1017/S0373463304002851

[4] Filjar, R, Kos, T, Kos, S. (2010). Low-cost space weather sensors for identification and estimation of GNSS performance space weather effects. *Proc of NAV10 Conference* (on CD-ROM). London, UK.

[5] Frissell, N.A., E.S. Miller, S.R. Kaeppler, F. Ceglia, D. Pascoe, N. Sinanis, P. Smith, R. Williams, and A. Shovkoplyas (2014). Ionospheric Sounding Using Real-Time Amateur Radio Reporting Networks. *Space Weather*, **12**, 651–656. doi:10.1002/2014SW001132.

[6] Hughes, I.G, and Hase, T.P.A. (2010). Measurements and their Uncertainties: A practical guide to modern error analysis. Oxford University Press. Oxford, UK.

[7] Hohnson, Jr, C.R, and W.A. Sethares (2003). Telecommunications Breakdown: Concepts of Communication Transmitted via Software-Defined Radio. Prentice Hall. Upper Saddle River, NJ.

[8] James, G, Witten, D, Hastie, T, and Tibshirani, R. (2014). An Introduction to Statistical Learning with Applications in R. Springer Science+Business Media. New York, NY. Available at: http://www-bcf.usc.edu/~gareth/ISL, accessed on 15 January, 2016.

[9] Maindonald and Braun. (2010). Data Analysis and Graphics Using R (3rd edition). Cambridge University Press. Cambridge, UK.

[10] Nature editorial. (2015). Rise of the citizen scientist. Nature, **524**, 265. Available at: http://bit.ly/1TSHBOC, accessed on 15 January, 2016. doi:10.1038/524265a

[11] Navipedia web-site. European Space Agency (ESA) in partnership with UN OOSA. Available at: http://www.navipedia.net

[12] Peng, R.D. (2015). Exploratory Data Analysis with R. Leanpub. Victoria, BC.

[13] Petovello, M. (2015). What are the actual performances of GNSS positioning using smartphone technology? *Inside GNSS*. Available at: http://www.insidegnss.com/auto/novdec14-SOLUTIONS.pdf, accessed on 15 January, 2016.

[14] Petrovski, I.G. (2014). GPS, GLONASS, Galileo, and Beidou for Mobile Devices: From Instant to Precise Positioning. Cambridge University Press. Cambridge, UK.

[15] Rembovski, A. *et al*. (2009). Radio Monitoring: Problems, Methods, and Equipment. Springer Science+Business Media. New York, NY.

[16] Sanz Subirana, J, Juan Zornoza, J.M, and Hernandez-Pajares, M. (2011). GNSS Data Processing – Volume I: Fundamentals and Algorithms. Euroepan Space Agency. Nordwijk, the Netherlands.

[17] Stevens, M. *et al*. (2014). Taking Participatory Citizen Science to Extremes. *Pervasive Computing*, April – June 2014, 20–29.

[18] Thomas, M. *et al.* (2011). Global Navigation Space Systems: reliance and vulnerabilities. The Royal Academy of Engineering. London, UK. Available at: http://bit.ly/1vrIenu, accessed on 10 February, 2016.

[19] Vasquez, T. (1998). International Weather Watchers Observer Handbook. Weather Graphics. Available at: http://www.weathergraphics.com/dl/obsman.pdf, accessed on 15 January, 2016.

[20] Vetter, J. (2011). Introduction: Lay Participation in the History of Scientific Observation. *Science in Context*, **24**(2), 127–141. Available at: https://arizona.openrepository.com/arizona/bitstream/10150/344544/1/intro.pdf, accessed on 15 January, 2016.

Faculty of Maritime Studies
University of Rijeka, Croatia
University of Zagreb
Faculty of Transport
and Traffic Sciences
Royal Institute of Navigation
Science Technology Practice
9th
Annual
Baška GNSS
Conference

REAL-TIME IONOSPHERIC ERROR CORRECTION IN SINGLE FREQUENCY GNSS POSITIONING USING NEQUICK 2

A. Kashcheyev, B. Nava, Y.O. Migoya Orue', S.M. Radicella

The Abdus Salam International Centre for Theoritical Physics (ICTP), Trieste
E-mail: anton.kascheev@gmail.com

ABSTRACT. *The main source of positioning error in single frequency GNSS receivers is due to the delay introduced by the ionosphere on the signals propagating through it. Therefore to mitigate the ionospheric effects and to improve the accuracy of the position determination, these widely used receivers have to estimate the ionospheric range delay using an appropriate model.*

In this paper an evaluation of NeQuick 2 capabilities to mitigate ionospheric range errors in single-frequency point positioning has been performed taking into account possible real-time applications. NeQuick 2 is the latest version of the NeQuick ionosphere electron density model developed in the International Centre for Theoretical Physics (ICTP), Italy with the collaboration of the Institute for Geophysics, Astrophysics and Meteorology of the University of Graz, Austria. It is a climatological model that uses monthly average values of solar activity expressed by the 12-month running mean sunspot number R_{12} as a driver. To pass from climatology to ionospheric weather the daily solar radio flux $F_{10.7}$ is used as a solar activity input parameter. In this particular study $F_{10.7}$ of the previous day is used in order to employ NeQuick 2 in a real-time mode.

As a reference for the performance analysis the following procedure to correct ionospheric range errors is selected. Global Ionospheric Maps (GIMs) provided by Center for Orbit Determination (CODE) are utilized to compute ionospheric range delay using the thin shell approximation at a suitable height and a mapping function (SBAS-like approach). For evaluation purposes, a comparison of the suggested method is done with the GPS ionospheric correction algorithm.

To assess the performance of the proposed algorithms on a global scale, the validation tests have been performed using data from a set of stations distributed worldwide with the focus on low latitudes. To extend the analysis to different ionospheric conditions, data for geomagnetically quiet and disturbed periods corresponding to different levels of solar activity and different seasons have been used. The results of the statistical analyses are presented in terms of average and standard deviation of the relevant errors.

KEY WORDS: *GNSS, positioning, ionospheric model, NeQuick*

1 INTRODUCTION

The GNSS signals are affected when passing through the ionosphere. The ionosphere can change various signal parameters such as group delay/phase advance, amplitude and polarization [1]. It has been known as a main source of errors for GNSS users after removal of the Selective Availability (SA) in the year 2000. The ionospheric range error varies from a few to tens of meters [2]. However, since the ionosphere is a dispersive medium (the ionospheric influence depends on the signal frequency) it is possible to eliminate most of this error using the ionosphere free linear combination in dual frequency receivers. Nevertheless, to improve positioning accuracy for single frequency receivers, which dominate the market, it is necessary to estimate the ionospheric impact using an appropriate model.

The Navstar Global Positioning System (GPS) uses the Klobuchar ionospheric model [3] to mitigate ionospheric effects. It is estimated to reduce ionospheric range error by about 50% in root mean square (RMS) worldwide. The BeiDou Navigation Satellite System uses an ionospheric model based on Klobuchar model that is designed to improve accuracy for northern hemisphere users in the Asia-Pacific region. However, it exhibits a degraded performance outside this area [4]. The European satellite navigation system Galileo uses NeQuick for Galileo (NeQuick G) algorithm. This algorithm is designed to correct at least 70% of the ionospheric code delay worldwide [5]. The updated coefficients for these ionospheric models are broadcast from the corresponding satellites in the navigation message.

Another option, based on the thin-shell approximation at an assumed height, is to map the ionosphere using data from a network of GPS base stations. The Wide Area Augmentation System (WAAS), the European Geostationary Navigation Overlay System (EGNOS) and the Multi-functional Satellite Augmentation System (MSAS) provide local ionospheric maps for different regions of the world by sending the information via geostationary satellites. All the methods described above are designed to be used in real-time applications.

The Global Ionospheric Maps (GIMs) are produced by various international GNSS service analysis centers: Jet Propulsion Laboratory (JPL), Center for Orbit Determination in Europe (CODE), Polytechnic University of Catalonia (UPC) and others and are available in the Internet with different latencies (from minutes to days). The global accuracy of these TEC maps is several TECU depending on the local time, solar cycle, season and location of available GPS receivers [6].

In this paper an alternative way of mitigating ionospheric errors in single-frequency point positioning is suggested. The NeQuick 2 [7] model is used to estimate ionospheric range delays using solar radio flux $F_{10.7}$ of the day before to drive the model, thus taking into account possible real-time applications. The results of the performance analysis of the proposed method are compared to those obtained with the GPS correction algorithm and with the method based on the thin shell approximation using GIMs (SBAS like approach) taken as a reference. The estimation of the performance of the suggested methods is done on a global scale using data from a set of GPS receivers distributed worldwide with the focus on low latitude regions. To understand the sensitivity of the method to diverse ionospheric conditions, data for more than one solar cycle has been used including geomagnetically quiet and disturbed periods. The results of the statistical analyses are presented in terms of average and standard deviation of the relevant errors.

2 METHODOLOGY

Ionospheric model

In this study the NeQuick-2 model has been used to model ionospheric range delays in order to mitigate the corresponding errors in single frequency real-time positioning applications. NeQuick 2 is the latest version of the NeQuick ionosphere electron density model developed at the Aeronomy and Radiopropagation Laboratory of the Abdus Salam International Centre for Theoretical Physics (ICTP) - Trieste, Italy with the collaboration of the Institute for Geophysics, Astrophysics and Meteorology of the University of Graz, Austria. The NeQuick is a quick-run ionospheric electron density model particularly designed for transionospheric propagation applications. To describe the electron density of the ionosphere above 90 km and up to the peak of the F2 layer, the NeQuick uses a profile formulation, which includes five semi-Epstein layers with modeled thickness parameters. Three profile anchor points are used: the E layer peak, the F1 peak and the F2 peak, that are modeled in terms of the ionosonde parameters foE, foF1, foF2 and M(3000)F2. These values can be modeled or experimentally derived. A semi-Epstein layer represents the model topside with a height-dependent thickness parameter empirically determined. The basic inputs of the NeQuick model are: position and time; the output is the electron concentration at the given location and time. It is a climatological model and uses monthly average values of solar activity expressed by the 12-month running mean sunspot number R_{12} as a driver. To pass from climatology to ionospheric weather the daily

solar radio flux $F_{10.7}$ is used as a solar activity input parameter. In this particular study $F_{10.7}$ of the day before is used in order to be able to use NeQuick 2 in a real-time mode.

Positioning algorithm

In this paper the GNSS-Lab Tool suite (gLAB) open source software [8] has been used to calculate positioning errors. The gLAB is an advanced interactive educational multipurpose package for GNSS data processing and analysis. This tool performs a precise modelling of the GNSS observables at the centimeter level, allowing GPS standard and precise point positioning (SPP, PPP). It is capable of reading a variety of standard formats such as Receiver Independent Exchange Format (RINEX), Solution (Software/technique) Independent Exchange Format (SINEX) and others. The gLAB is flexible, able to run under Linux and Windows operating systems (OS) and it is made freely available by European Space Agency (ESA) to Universities and GNSS professionals. It is programmed in C and Python languages and is divided in three main software modules: the data processing core (DPC), the data analysis tool and the graphical user interface (GUI). The DPC implements all the data processing algorithms and can be executed in command line. The DAT provides a plotting tool for the data analysis. The GUI consists of different graphic panels for a user friendly managing of both the DPC and DAT. Both the DPC and DAT modules may be used independently of the GUI, including them in batch files to automatically process GNSS data. By default the gLAB allows using no ionospheric correction or Klobuchar model to account for the ionospheric contribution in single point positioning (SPP). In order to use NeQuick 2 and GIM correction algorithms the DPC module has been modified. The additional correction algorithms implemented are: global ionospheric maps, NeQuick 2 using $F_{10.7}$ of the day before, NeQuick 2 using sun spot number (SSN) of the day before and standard NeQuick 2 that uses R_{12}. In this paper only the results for the method based on NeQuick 2 with $F_{10.7}$ of the day before are presented.

GNSS data set

The data of 24 stations from the IGS network [9] have been selected: 10 low-latitude, 7 mid-low latitude and 7 mid-latitude stations in terms of modip (Fig. 1). The period of 14 years (from 2001 to 2014) has been chosen for this study. The selected period includes the peak of the solar activity in the Solar Cycle 23 (year 2001-2002) and the deep minimum in the Solar Cycle 24 (year 2008-2009). The precise locations of the selected stations have been obtained from a SINEX file publicly available on the IGS web site.

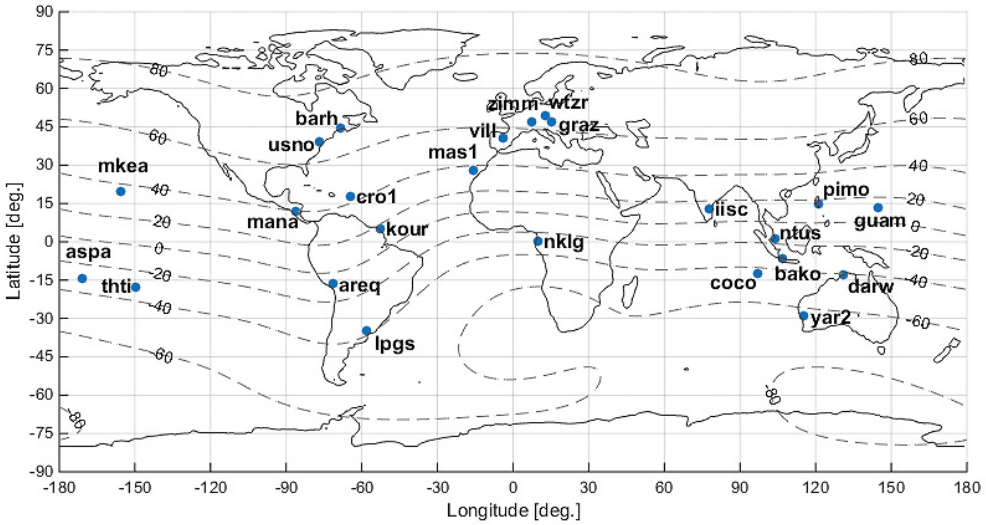

Figure 1 Location of the GNNS stations selected for the performance analysis. The dashed lines are modip isolines.

The global ionospheric maps with two hours time interval computed by CODE have been chosen. GIMs are generated on a daily basis using data from GNSS stations of the IGS and other institutions. The vertical total electron content (VTEC) is modeled in a solar-geomagnetic reference frame using a spherical harmonics expansion. Piece-wise linear functions are used for representation in the time domain. More details about the processing of CODE global ionospheric maps can be found in [10].

Methodology

The SPP solution has been computed for each RINEX file from the data set. The number of the RINEX files used amounted to more than 1.2e5. The 15 minute time interval and 5° elevation mask have been selected, thus, taking into account data gaps for some of the selected receivers, the total number of processed links amounted to 1e7. The output message of the gLAB software contains North, East and Height errors in the position calculation. In this paper the results of the statistical analyses of the height errors only are presented because they are the more significant ones.

3 RESULTS AND DISCUSSION

The average and standard deviation of the height error for the period from 2001 to 2014 are presented on the Fig. 2 for each single station considered in the present study. It is clearly seen that all the correction algorithms are correcting the average and reducing the dispersion of the height error. In general, the NeQuick model is outperforming Klobuchar model in average and standard deviation, while GIM CODE is better than NeQuick in dispersion but not in average, especially for the low latitude stations, where GIM CODE exhibit bigger ionospheric residual errors. The standard deviation for mid-low latitude stations is comparable or higher than for low latitude that could be explained by the presence of big electron density and TEC gradients in the ionospheric equatorial anomaly crests.

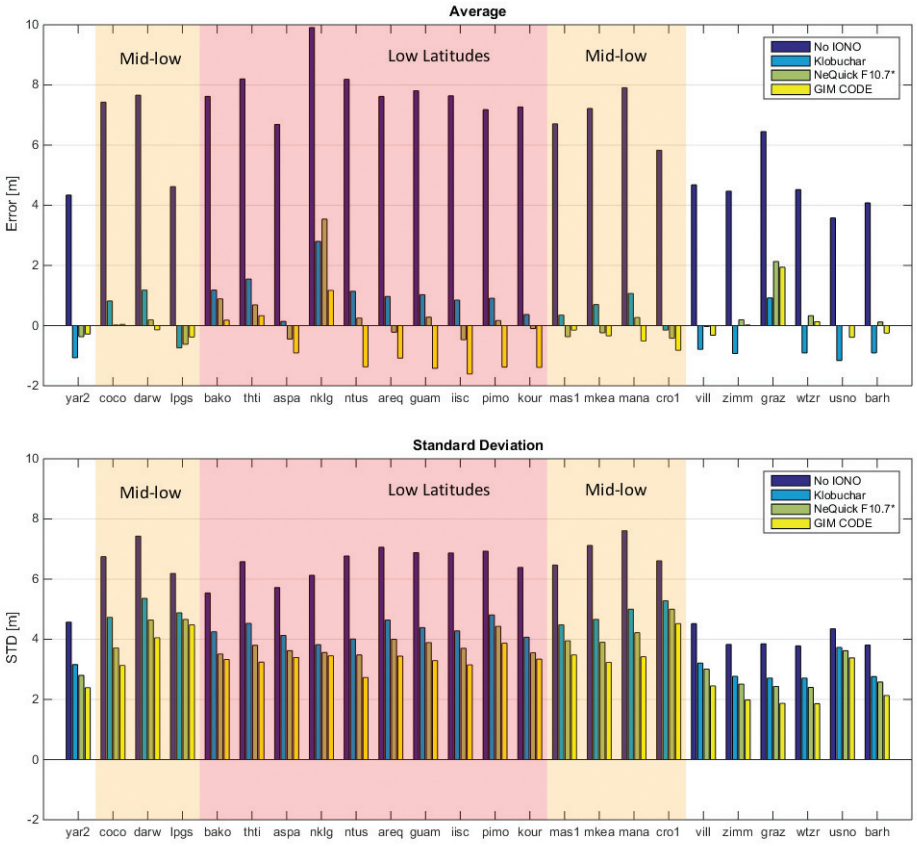

Figure 2 The average and standard deviation of the height error for the period from 2001 to 2014, computed using different correction alghoritms: no ionospheric correction, Klobuchar model, NeQuick driven by the $F_{10.7}$ of the day before and CODE GIM. Stations are sorted by modip.

Figures 3 and 4 contain height error with 15 minutes time interval (A) and monthly averaged (B) of the two stations for the period from the year 2001 to 2014. The first is a low-latitude station thti (lat = -17.58°, lon = 210.39°) and the second is a mid-latitude station wtzr (lat = 49.14°, lon = 12.88°). Orange lines on the plots represent the running mean sunspot number R_{12}. It could be noted that the error is following the solar activity: increases during the periods of maximum solar activity and decreases during the solar activity minimum. Another feature of the error behavior is a seasonal oscillation with maxima during equinoxes and minima during solstices. From the monthly averaged plots it is clear that no model can fully mitigate the ionosphere effects, especially during periods of high solar activity.

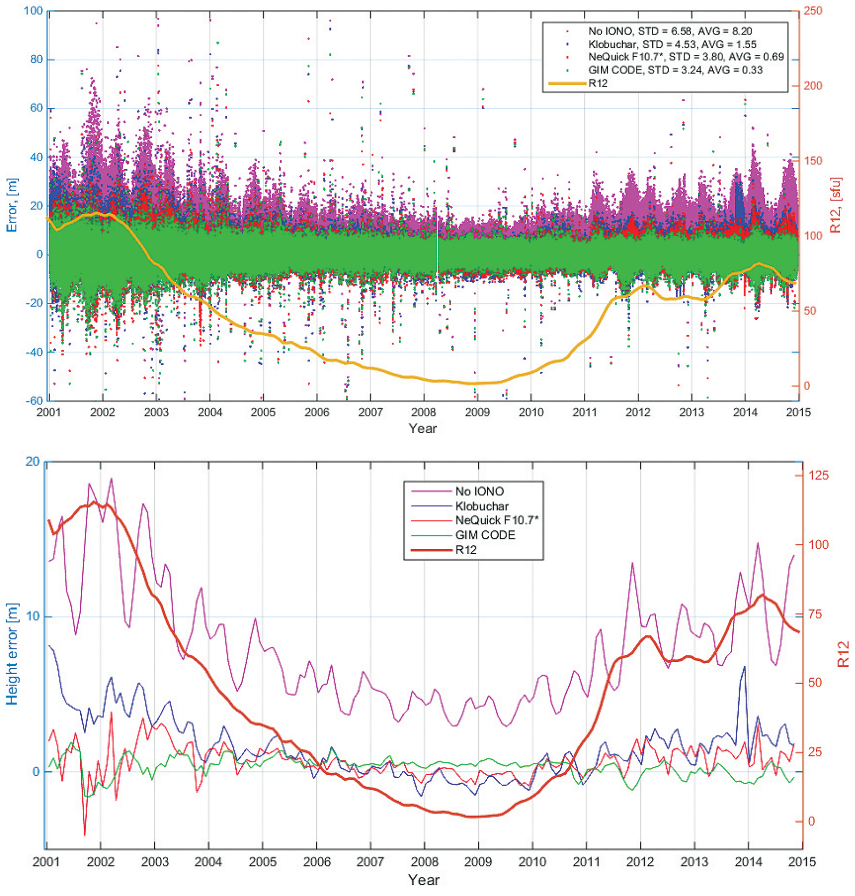

Figure 3 The height error every 15 minutes (A) and monthly averaged (B) for the station thti (lat = –17.58°, lon = 210.39°) computed using different correction alghoritms: no ionospheric correction, Klobuchar model, NeQuick driven by the $F_{10.7}$ of the day before and CODE GIM. The orange line represents R_{12} index.

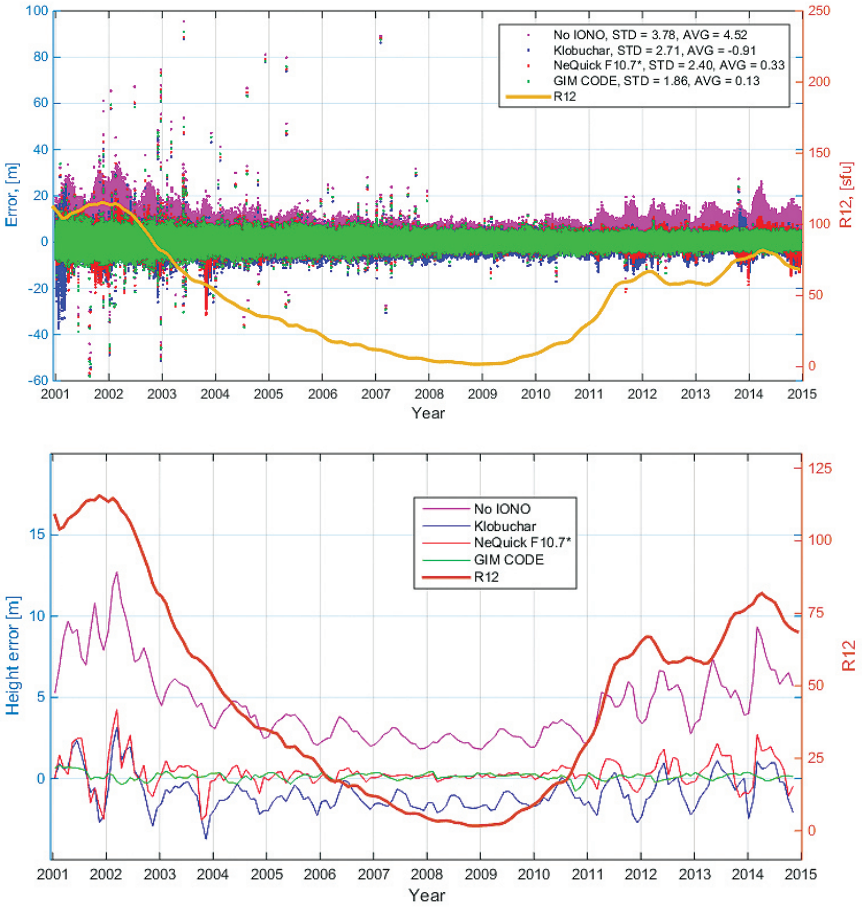

Figure 4 The height error every 15 minutes (A) and monthly averaged (B) for the station wtzr (lat = 49.14°, lon = 12.88°) computed using different correction alghoritms: no ionospheric correction, Klobuchar model, NeQuick driven by the $F_{10.7}$ of the day before and CODE GIM. The orange line represents R_{12} index.

Figures 5 and 6 show daily and seasonal distribution of the height error for the low latitude station guam (lat = 13.59°, lon = 144.87°) during the periods of the high (year 2002) and low (year 2009) solar activity correspondingly. Figures 7 and 8 show the same error statistics but for the mid-latitude station zimm (lat = 46.88°, lon = 7.47°), year 2002 and 2008. The color scales of the plots are not identical in order to display possible error patterns. It can be noticed that the behavior of the uncorrected error has clear seasonal and daily variations. The error increases in post mid-day hours and is higher in equinoxes than in solstices.

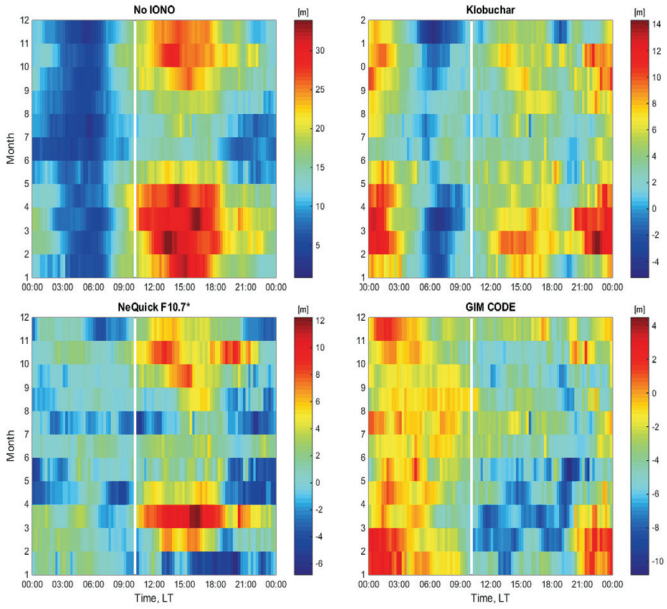

Figure 5 The daily and seasonal distribution of the height error for the station guam (lat = 13.59°, lon = 144.87°), year 2002 (high solar activity).

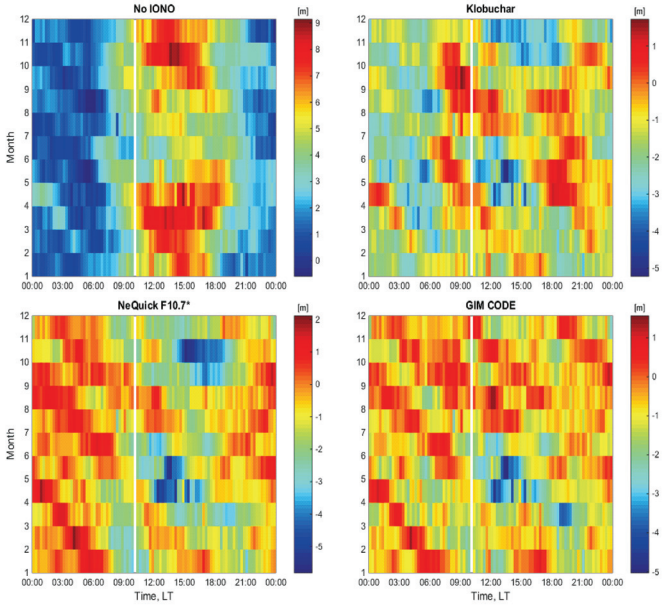

Figure 6 The daily and seasonal distribution of the height error for the station guam (lat = 13.59°, lon = 144.87°), year 2009 (low solar activity).

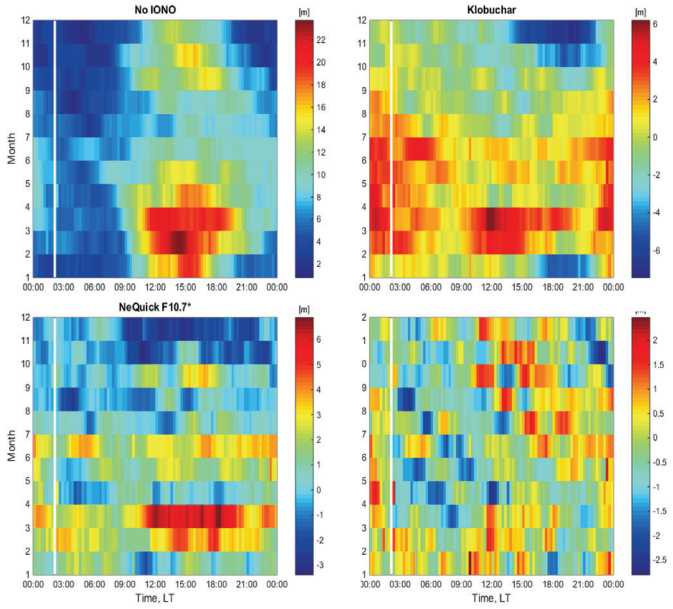

Figure 7 The daily and seasonal distribution of the height error for the station zimm (lat = 46.88°, lon = 7.47°), year 2002 (high solar activity).

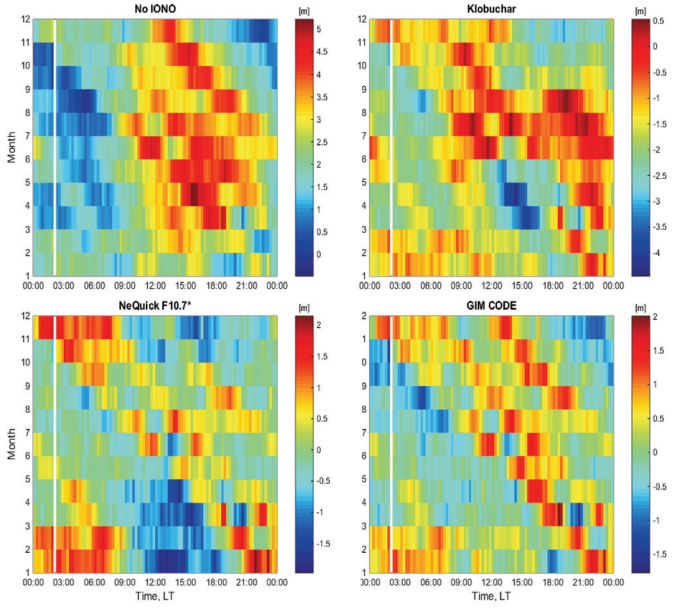

Figure 8 The daily and seasonal distribution of the height error for the station zimm (lat = 46.88°, lon = 7.47°), year 2008 (low solar activity).

During the period with high solar activity (Fig. 5,7), NeQuick model has similar pattern to uncorrected error, meaning that the model does not fully correct the positioning error induced by the ionosphere.However, Klobuchar and GIM CODE underestimate ionospheric influence mainly during night hours. In the period of the low solar activity (Fig. 6, 8) the seasonal variations of the uncorrected error are not that evident, especially for the low latitude station (Fig. 8). None of the correction algorithms show a regular pattern.

To analyze the model performance under diverse ionospheric conditions in terms of geomagnetic activity, all the data has been classified in four ranges according to the value of disturbance storm time (Dst) index (Table 1). Figure 9 shows variations of the Dst and R_{12} indices during the whole period in question. Figure 10-13 and 14-17 contain average and standard variation of the height errors obtained for each of the classified geomagnetic activity range. The plots contain data of 24 stations for the period from 2001 to 2014. It is clearly seen that the average and the standard deviation of the error depend on geomagnetic activity. In average the NeQuick method outperforms Klobuchar algorithm in most of the cases (Fig. 10-12) except during super storms (Fig. 13). Moreover, at the same time it outperforms the GIM CODE technique for low latitude stations. However, in terms of dispersion, it corrects better only during quiet days or moderate storms (Fig. 14, 15). Considering that models like NeQuick are not specifically designed to reproduce the ionosphere behaviour during geomagnetic disturbed periods, further studies will be carried out to better interpret these specific results.

Table 1 Magnetic storm classification

Super storms	Dst < –200 nT
Intense storms	–200 nT ≤ Dst < –100 nT
Moderate storms	–100 nT ≤ Dst < –50 nT
Quiet to minor storms	–50 nT ≤ Dst

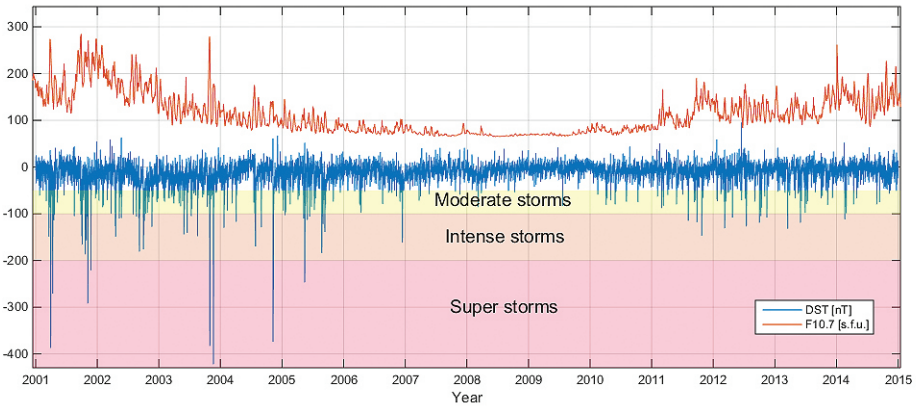

Figure 9 Dst and $F_{10.7}$ indices. Years 2001 – 2014.

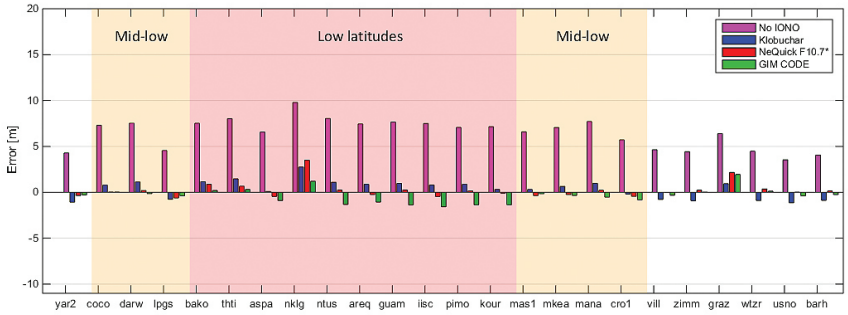

Figure 10 Quiet days (Dst ≥ –50 nT). The average height error for the period from 2001 to 2014, computed using different correction alghoritms: no ionospheric correction, Klobuchar model, NeQuick driven by the $F_{10.7}$ of the day before and CODE GIM. Stations are sorted by modip.

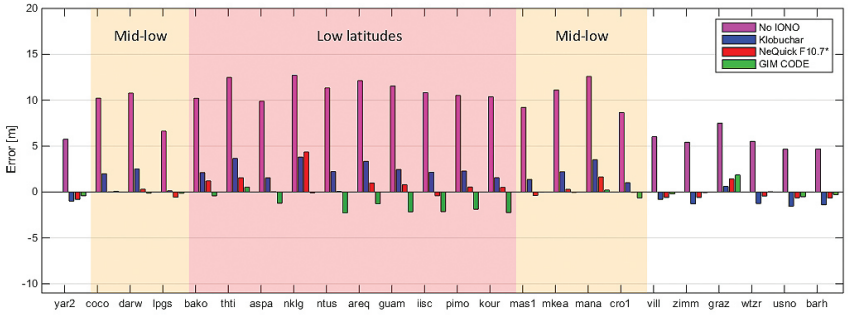

Figure 11 Moderate storms (–50 nT > Dst ≥ –100 nT). The average height error for the period from 2001 to 2014, computed using different correction alghoritms: no ionospheric correction, Klobuchar model, NeQuick driven by the $F_{10.7}$ of the day before and CODE GIM. Stations are sorted by modip.

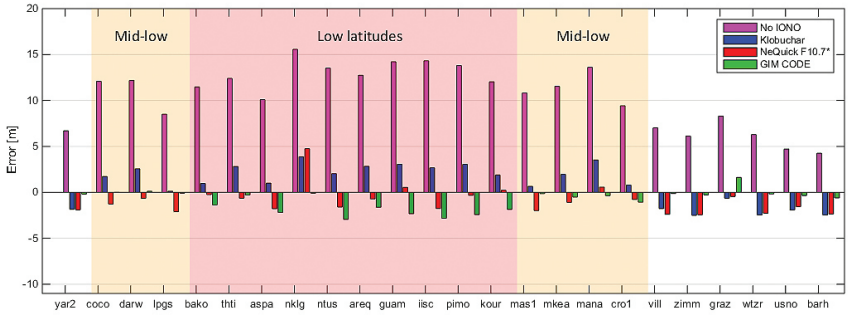

Figure 12 Intense storms (–100 nT > Dst ≥ –200 nT). The average height error for the period from 2001 to 2014, computed using different correction alghoritms: no ionospheric correction, Klobuchar model, NeQuick driven by the $F_{10.7}$ of the day before and CODE GIM. Stations are sorted by modip.

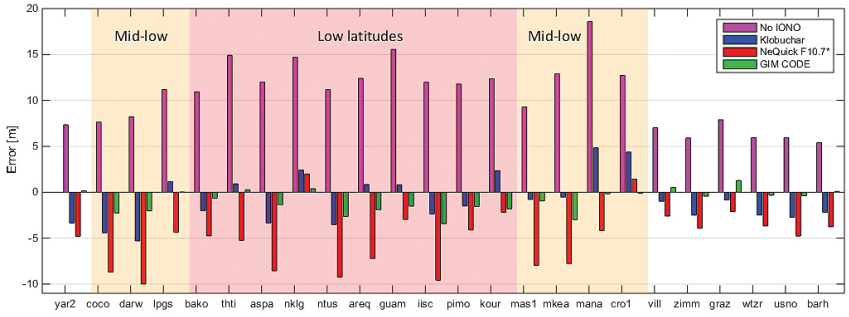

Figure 13 Super storms (Dst ≥ –200 nT). The average height error for the period from 2001 to 2014, computed using different correction alghoritms: no ionospheric correction, Klobuchar model, NeQuick driven by the $F_{10.7}$ of the day before and CODE GIM. Stations are sorted by modip.

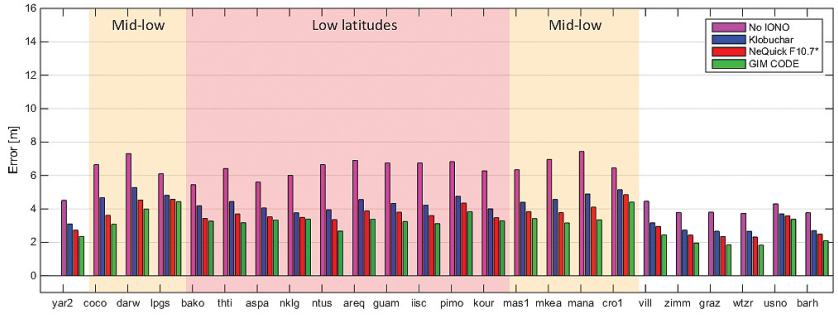

Figure 14 Quiet days (Dst ≥ –50 nT). The standard deviation of the height error for the period from 2001 to 2014, computed using different correction alghoritms: no ionospheric correction, Klobuchar model, NeQuick driven by the $F_{10.7}$ of the day before and CODE GIM. Stations are sorted by modip.

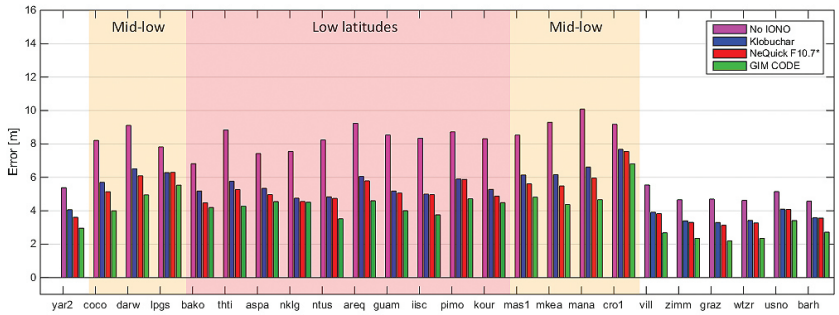

Figure 15 Moderate storms (–50 nT > Dst ≥ –100 nT). The standard deviation of the height error for the period from 2001 to 2014, computed using different correction alghoritms: no ionospheric correction, Klobuchar model, NeQuick driven by the $F_{10.7}$ of the day before and CODE GIM. Stations are sorted by modip.

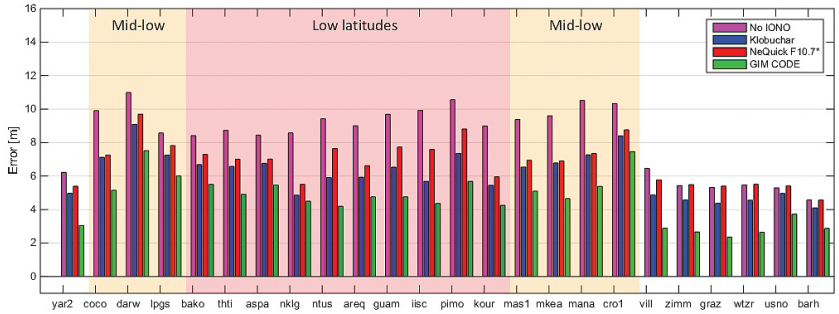

Figure 16 Intensive storms (–100 nT > Dst ≥ –200 nT). The standard deviation of the height error for the period from 2001 to 2014, computed using different correction alghoritms: no ionospheric correction, Klobuchar model, NeQuick driven by the $F_{10.7}$ of the day before and CODE GIM. Stations are sorted by modip.

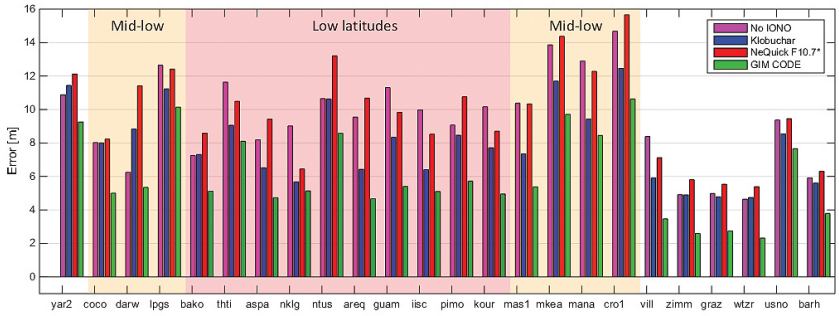

Figure 17 Super storms (Dst ≤ –200 nT). The standard deviation of the height error for the period from 2001 to 2014, computed using different correction alghoritms: no ionospheric correction, Klobuchar model, NeQuick driven by the $F_{10.7}$ of the day before and CODE GIM. Stations are sorted by modip.

4 CONCLUSIONS

In this paper an evaluation of the NeQuick 2 capabilities to mitigate ionospheric range errors in single-frequency point positioning has been performed taking into account possible real-time applications. The comparison of the suggested algorithm has been done with other existing methods: without correcting ionosphere and using Klobuchar model. As a reference the correction method based on the use of the CODE vertical TEC maps with the thin shell approximation has been considered.

This study has shown that the ionospheric correction algorithm relying on NeQuick 2 model with a $F_{10.7}$ index of the day before can be used as an alternative to existing methods. In most of the cases the suggested method compensates the ionospheric delay better than the Klobuchar model, however (as expected) bigger errors arise during periods of very high geomagnetic activity. The performance of the GIM CODE algorithm in most of the cases is better than that of NeQuick. However, as far as real time applications are concerned, the advantage of NeQuick is that it uses only one parameter ($F_{10.7}$ of the day before) to drive the model. This parameter could be distributed among the GNSS users.

The possible future work is to improve the performance of the ionospheric correction algorithm based on NeQuick 2 model during periods of high solar and geomagnetic activities.

Acknowledgments

Authors are grateful to the International GNSS Service (IGS) for the GNSS data available. We acknowledge the use of geomagnetic data and services provided by World Data Center for Geomagnetism, Kyoto [11]

REFERENCES

[1] Davies, K. (1990). Ionospheric Radio, Peter Peregrinus Ltd, London.

[2] Klobuchar, J.A. (1996). Ionospheric Effects on GPS, In: Global Positioning System: Theory and Applications, Vol I, Parkinson, B.W. & Spilker, J.J., pp. 485–515, American Institute of Aeronautics & Astronautics, ISBN 156347106X.

[3] Klobuchar, J.A. (1987). Ionospheric time-delay algorithm for single frequency GPS users. IEEE Trans Aerospace Electron Syst AES 23(3):325–331.

[4] CSNO (2012). BeiDou Navigation Satellite System Signal In Space Interface Control Document – Open Service Signal B1, Version 1.0, China Satellite Navigation Office, Dec 2012.

[5] Prieto-Cerdeira, R.; Pérez, R.O.; Breeuwer, E.; Lucas-Rodriguez R.; Falcone M. (2014). Performance of the Galileo Single-Frequency Ionospheric Correction During In-Orbit Validation. GPS world 06/2014; 25(6):53–58.

[6] Hernandez-Pajares, M.; Juan, J. M.; Sanz J. et al. (2009). The IGS VTEC maps: a reliable source of ionospheric information since 1998, Journal of Geodesy, vol. 83, no. 3-4, pp. 263–275, 2009.

[7] Nava, B.; Coïsson, P.; Radicella, S.M. (2008). A new version of the NeQuick ionosphere electron density model, J. Atmos. Sol. Terr. Phys., 70, 1856–1862, doi: 10.1016/j.jastp.2008.01.015.

[8] Sanz, J.; Rovira-Garcia, A.; Hernandez, M.; Juan, J.; Ventura-Traveset, J.; Lopez, C.; Hein, G. (2012). The ESA/UPC GNSS-Lab Tool (gLAB): An advanced educational and professional package for GNSS data processing and analysis. 6th ESA Workshop on Satellite Navigation Technologies Multi-GNSS Navigation Technologies. Proceedings ISBN: 978-1-4673-2010-8, doi: 10.1109/NAVITEC.2012.6423100. Noordwijk, the Netherlands. December 2012.

[9] Dow, J.M.; Neilan, R.E.; Gendt, G. (2005). The International GPS Service (IGS): Celebrating the 10th Anniversary and Looking to the Next Decade. Adv Space Res 36(3):320–326. doi:10.1016/j.asr.2005. 05.125, 2005.

[10] Schaer, S. (1999). Mapping and Predicting the Earth's Ionosphere Using the Global Positioning System, Dissertation, Astronomical Institute, University of Berne, Berne, Switzerland, 25 March 1999.

[11] http://wdc.kugi.kyoto-u.ac.jp/wdc/Sec3.html

Faculty of Maritime Studies
University of Rijeka, Croatia

University of Zagreb
Faculty of Transport
and Traffic Sciences

Royal Institute of Navigation
Science Technology Practice

9th
Annual
Baška GNSS
Conference

DISCREPANCIES BETWEEN PREDICTED AND FINAL IGS IONOSPHERIC MAPS IN THE NORTHERN ADRIATIC REGION

Serdjo Kos, Mate Barić, David Brčić

Faculty of Maritime Studies, University of Rijeka, Croatia
E-mail: mbaric@pfri.hr

ABSTRACT. *The IGS VTEC maps represent a reliable source of ionospheric information in areas where TEC dynamics cannot be measured directly. Among various IGS products, predicted and measured VTEC are given on daily basis in corresponding standardised data formats. The aim of this research was the study of ionospheric dynamics in the Northern Adriatic region based on provided VTEC maps. VTEC dynamics, both predicted and measured, were gathered during year 2012. Daily VTEC dynamics were analysed, introducing existence of three types of prevalent daily VTEC patterns. The local daily patterns were detected both with predicted and measured VTEC maps, although particular pattern and value differences were observed. Differences (residuals) between predicted and measured VTEC values in 2012 for all 366 days were calculated. Residual values were analysed and compared with solar and geomagnetic activity, aiming at possible relation between space weather events and residual values' patterns. Depending on season and daily patterns, residuals can be obtained and predicted VTEC behaviour can be corrected. In relation to daily VTEC fluctuations with space weather activity, season and daytime, predicted VTEC values could be improved for predicting GPS position errors within considered area.*

KEY WORDS: *Global Positioning System, International GNSS Service, Ionospheric VTEC maps, Total Electron Content, Northern Adriatic region*

1 INTRODUCTION

International GNSS Service (IGS) provides databases of predicted and measured Vertical Total Electron Content (VTEC) values in form of Global Ionospheric Maps (GIM). The aim of this research was to determine possible causes of discrepancies which cause differences between predicted and final VTEC maps. VTEC, both predicted and final were gathered and residuals were compared. VTEC data are provided for every day of year, with 2-hours daily time resolution. Data are given for positions from equator to North/South Pole every 2.5° of latitude and from W 180°/E 180° every 5° in longitude. For the purpose of the research, geographical position located in Northern Adriatic (45°N/015°E) was used. Obtained daily residuals from specified position were divided by seasons and singled out according to high space weather activity, providing background for the predicted VTEC correction. The correction is introduced by suggested model for days with high residuals and *Kp* index (representing disturbances in the horizontal component of the geomagnetic field) to reduce error margin. Daily fluctuations of predicted VTEC will be more accurate and in future used for predicting GPS position errors.

2 BACKGROUND

Data for GNSS is standardized and following formats are used. Reader Independent Exchange Format (RINEX) is used for GPS and GLONASS observations. Format consists of six ASCII file types: observation data, navigational message, meteorological data, GLONASS navigational message, GEO navigational message, satellite and receiver clock date. IONEX format is used for exchanging two and three dimensional TEC maps in specific geographical grid, containing interpolated data for areas not covered with IGS stations. In the IONEX format, ionosphere maps are given in earth-fixed reference frame, representing specific epoch in ionosphere. Single layer maps are allowed but three dimension maps are also included (Schaer and Gurtner, 1998). IONEX TEC maps latency is from 9 to 16 days (final product) and 1 to 2 days (rapid TEC). ANTEX files are used for defining profiles of antennas. There are three offsets, north, east and vertical, and changes in antenna phase centre which is a function of signal elevation and azimuth. Values are given in five degree interval from 0° to 90° for elevation and for azimuth from 0° to 360° (Dawidowicz, 2010).

Propagating through the space between antennas, transmitted positioning signal is affected by the ionosphere resulting in the code delay/phase advance, 1 ns of delay

being equal to 2.85×10^{16} el/m^2 of the total electron content unit (TECU) (Parkinson and Spilker, 1996). The delay can be measured by multi-frequency (usually dual) GPS receiver, providing codes (P_1/P_2) and carrier phase (L_1/L_2) differences.

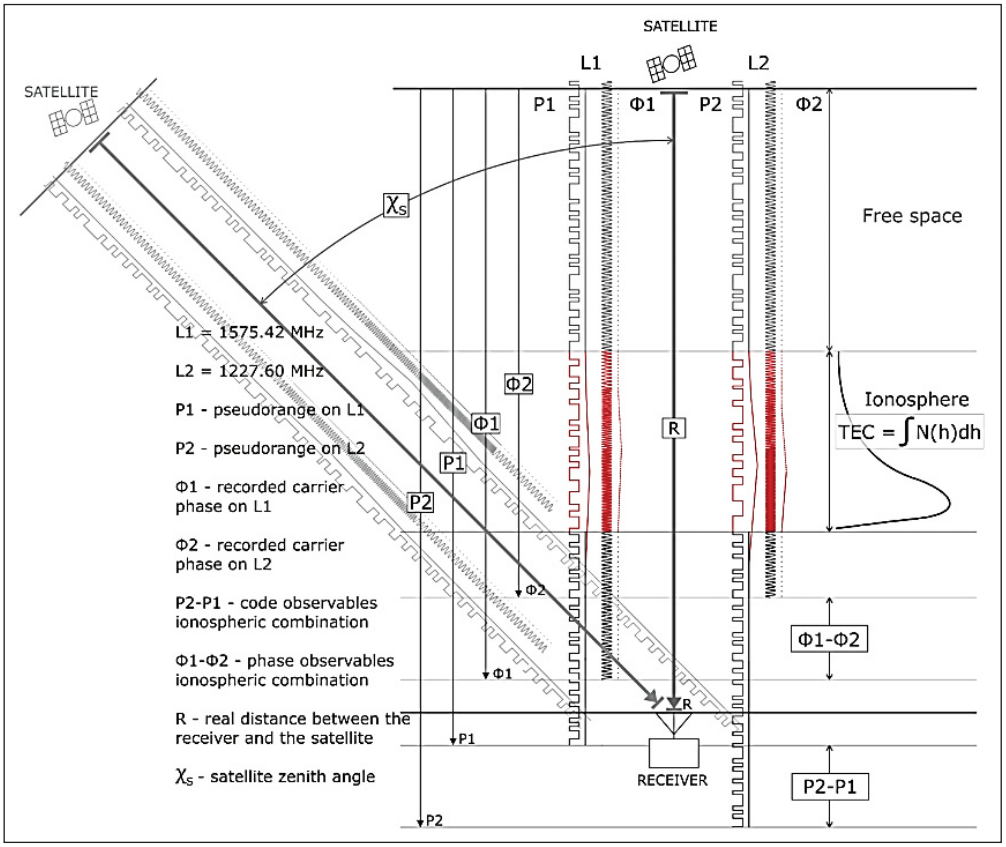

Figure 1 Determination of the total electron content using dual frequency GPS code and phase measurements

Free electrons produce a delay in the pseudo-range and an advance in the carrier phase (ionospheric divergence). One TEC unit produces a delay of 0.163 meters on L_1, and 0.267 m on L_2. Every excess of 10 cm of pseudorange on L_1–L_2 corresponds to 1 TEC unit, or:

$$TEC_\rho = \frac{\rho_{L2} - \rho_{L1}}{0.104 TEC} \qquad (1)$$

ρ – pseudorange measurements [m]

If carrier phase is used to determine TEC it is necessary to convert phase from radians to meters (Dyrud *et al*, 2008):

$$TEC_{\phi} = \frac{-\phi_{L2} + \phi_{L1}}{0.104TEC} \quad \textbf{(2)}$$

ø – carrier phase (converted from radians to meters)

Determining TEC from GPS observations along transmitted signal, between satellite and receiver, mathematically can be expressed:

$$TEC = \int_{xr}^{s} \rho(\theta, \phi, h) ds \quad \textbf{(3)}$$

where ρ represents ray-path between satellite and receiver and the integral is along a straight ray path between receiver and satellite locations **(**Mannuci *et al*, 1999**)**.

Ionosphere is defined as "ionosphere shell", two dimension surface defined by ionosphere profile peaks (Komjathy and Langley, 1996). Shell height is assumed to be 350 km above sea level. The ray path represents slant TEC (STEC), a TEC on the path of the transmitted signal. However, recently shell height is assumed to be 450 km where roughly is the median height of electron density for typical daytime profile, and because height of 350 km reduces the TEC determining accuracy **(**Mannuci *et al*, 1998**)**.

Use of coarse tomographic (VOXEL) model with two layers allows better determination of TEC. In the thin layer model the ionosphere delay is only a function of a pierce point. The voxel model has an implicit horizontal gradient (Hernandez-Pajares *et al*, 2002).

Global TEC maps have to be interpolated, because IGS stations do not cover certain Earth areas. One way of interpolating is by individual triangular tiles. Each tile is regarded as a rigid plate, so global TEC distribution is approximated by piecewise bilinear TEC gradients. Three vertices of each tile are separated roughly 800 km. First step of constructing function is creating a great circle which passes through vertex *A* and measurement point *E*, that are intersects on opposite side at point *D*. TEC at point *D* is derived from distance weighted interpolation of the TEC at the vertices *B* and *C*:

$$V_D = \frac{DC}{BC} V_B + \frac{BD}{BC} V_c \quad \textbf{(4)}$$

Fraction represents distance between vertices and V_B, V_C is TEC at vertices *B* and *C*. TEC at point *E* is derived similarly **(**Mannuci *et al*, 1998**)** by expression:

$$V_E = \frac{ED}{AD} V_A + \frac{AE}{AD} V_D \qquad \textbf{(5)}$$

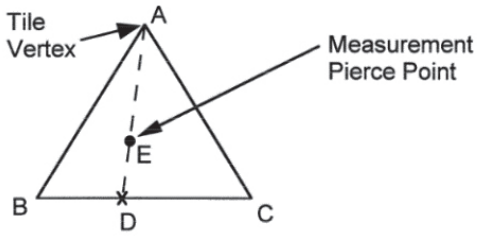

Figure 2 Determination of the GIM TEC within a tile (Mannuci *et al*, 1998)

Also, for interpolation, the Gaussian radial biases function is used; when the weights are Gaussian function of the distance between the data points to the point of interpolation is desired. Also, International Reference Ionosphere (IRI) model (Bilitza, 2002) can be applied as a reference ionospheric model to carry out the interpolation for determining global TEC maps (Hernandez-Pajares *et al*, 2002). To determine interpolation accuracy, data is compared with TEC maps from TOPEX measurement, with dual altimeters.

Predicted VTEC maps are available through prediction model which is developed in the frame of IONEX maps. Prediction is available for 2 days in advance. Prediction of VTEC is based on GIM maps and the use of Linear Regression combined with the Discrete Cosine Transform (LRDCT method) (Hernandez-Pajares *et al*, 2009). The model is trained by using final VTEC maps, while the prediction is done by rapid VTEC maps due to availability of data on server. Prediction is done by expressing every IONEX map in local time as an expansion of cosines function with certain amplitudes defined by DCT coefficients, referred as C in equation 6:

$$Cp,q = \alpha p \alpha q \sum_{m=0}^{M-1} \sum_{n=0}^{N-1} x_{m,n} \cos\frac{\pi(2m+1)p}{2M} \cos\frac{\pi(2n+1)p}{2N}, \qquad \textbf{(6)}$$
$$0 \le p \le M-1, 0 \le q \le N-1$$

x being the input matrix derived from each IGS GIM map, *p* and *q* being latitude and longitude spatial frequency components, and *M* and *N* being the row and

```
     1.0            IONOSPHERE MAPS     MIX                 IONEX VERSION / TYPE
cmpcmb v1.2          GRL/UWM             2-aug-12 23:38      PGM / RUN BY / DATE
ionex file containing IGS COMBINED Ionosphere maps           COMMENT
global ionosphere maps for day 200, 2012                     DESCRIPTION
IONEX file containing the COMBINED IGS TEC MAPS and DCBs     DESCRIPTION
      IONEX files of the following IAACs were combined: cod  DESCRIPTION
                                                        esa  DESCRIPTION
                                                        jpl  DESCRIPTION
                                                        upc  DESCRIPTION
Contact address: Andrzej Krankowski                          DESCRIPTION
                 Geodynamics Research Laboratory             DESCRIPTION
                 University of Warmia and Mazury (GRL/UWM)   DESCRIPTION
                 Oczapowski St. 1                            DESCRIPTION
                 10-957-Olsztyn, POLAND                      DESCRIPTION
                 e-mail:  kand@uwm.edu.pl                    DESCRIPTION
                                                             DESCRIPTION
  2012     7    18     0     0     0                        EPOCH OF FIRST MAP
  2012     7    19     0     0     0                        EPOCH OF LAST MAP
  7200                                                       INTERVAL
    13                                                       # OF MAPS IN FILE
  COSZ                                                       MAPPING FUNCTION
     0.0                                                     ELEVATION CUTOFF
combined TEC calculated as weighted mean of input TEC values OBSERVABLES USED
   420                                                       # OF STATIONS
    32                                                       # OF SATELLITES
  6371.0                                                     BASE RADIUS
     2                                                       MAP DIMENSION
   450.0 450.0   0.0                                        HGT1 / HGT2 / DHGT
    87.5 -87.5  -2.5                                       LAT1 / LAT2 / DLAT
  -180.0 180.0   5.0                                       LON1 / LON2 / DLON
    -1                                                       EXPONENT
TEC values in 0.1 tec units;  9999, if no value available    COMMENT
DCB values in nanoseconds, reference is Sum_of_SatDCBs = 0   COMMENT
DIFFERENTIAL CODE BIASES                                     START OF AUX DATA
   G01   -10.795      0.061                                  PRN / BIAS / RMS
   G02     5.955      0.011                                  PRN / BIAS / RMS
   G03    -2.288      0.019                                  PRN / BIAS / RMS
   G04    -1.289      0.050                                  PRN / BIAS / RMS
   G05     1.203      0.238                                  PRN / BIAS / RMS
   G06    -1.954      0.026                                  PRN / BIAS / RMS
   G07     1.691      0.078                                  PRN / BIAS / RMS
   G08    -2.714      0.059                                  PRN / BIAS / RMS
   G09    -1.633      0.027                                  PRN / BIAS / RMS
   G10    -3.729      0.135                                  PRN / BIAS / RMS
   G11     2.365      0.011                                  PRN / BIAS / RMS
   G12     2.488      0.074                                  PRN / BIAS / RMS
   G13     1.791      0.030                                  PRN / BIAS / RMS
    1                                                        START OF TEC MAP
  2012     7    18     0     0     0                        EPOCH OF CURRENT MAP
    87.5-180.0 180.0   5.0 450.0                            LAT/LON1/LON2/DLON/H
  109  109  109  109  109  109  109  109  109  109  109  108  108  108  108  107
  106  105  105  104  104  103  102  102  101  101  100   99   98   98   98   97
   97   97   96   96   95   95   95   95   95   95   96   96   96   97   97   97
   98   98   99   99  100  100  101  102  102  102  103  104  104  105  105  106
  106  107  107  107  108  108  108  108  109
    85.0-180.0 180.0   5.0 450.0                            LAT/LON1/LON2/DLON/H
  118  118  119  119  119  119  120  120  120  119  119  118  118  117  116  115
  114  113  112  111  110  108  107  105  104  102  101  100   98   97   96   95
   94   93   92   92   91   91   91   92   92   93   93   94   95   96   97   97
   98   99  100  101  102  103  104  105  106  106  107  108  109  109  110  112
  112  113  114  115  115  116  117  118  118
    82.5-180.0 180.0   5.0 450.0                            LAT/LON1/LON2/DLON/H
  126  127  127  128  129  129  130  130  129  129  129  128  127  126  126  125
  124  123  121  119  116  115  112  111  108  106  103  101   99   97   95   93
   92   91   90   90   90   90   90   91   92   93   94   96   97   99  100  101
  102  103  105  106  107  108  109  110  111  111  112  113  113  115  116  117
  118  119  120  121  122  123  124  125  126
    80.0-180.0 180.0   5.0 450.0                            LAT/LON1/LON2/DLON/H
  133  134  136  137  139  139  140  140  140  140  140  139  138  137  136  134
  132  130  129  126  123  121  119  115  112  109  107  105  102  100   98   96
   94   93   92   92   92   92   92   93   94   96   97   99  101  103  105  107
  108  109  110  112  113  115  115  116  116  116  117  117  118  119  120  121
  123  124  125  126  128  129  130  131  133
    77.5-180.0 180.0   5.0 450.0                            LAT/LON1/LON2/DLON/H
  137  140  141  144  146  147  148  148  149  149  148  147  145  143  142  141
  139  137  135  132  129  126  122  120  116  114  111  108  105  104  101   99
   98   96   96   96   95   96   96   97   99  101  102  104  107  109  111  112
  114  115  117  118  120  120  121  121  121  120  120  120  121  122  122  124
  125  126  127  129  131  132  134  136  137
    75.0-180.0 180.0   5.0 450.0                            LAT/LON1/LON2/DLON/H
  140  142  144  147  149  151  152  154  155  154  153  152  151  150  148  145
  143  139  138  135  132  128  125  121  119  116  114  111  109  106  104  103
  101  100  100  100  100  100  101  102  104  105  107  110  112  114  116  118
  119  120  122  122  123  123  123  123  122  121  121  122  122  122  122  123
  124  126  128  129  132  133  136  138  140
    72.5-180.0 180.0   5.0 450.0                            LAT/LON1/LON2/DLON/H
  139  142  144  146  149  152  154  156  157  157  157  156  155  152  150  147
  143  141  138  135  132  129  125  122  119  116  114  112  110  107  106  104
  104  103  102  102  103  103  104  104  107  109  110  112  115  117  119  121
  122  123  124  124  124  123  123  122  121  121  121  121  121  121  121  121
  123  124  127  129  131  133  135  137  139
    70.0-180.0 180.0   5.0 450.0                            LAT/LON1/LON2/DLON/H
  138  140  142  145  147  150  153  156  158  158  159  158  156  154  151  148
  144  141  137  133  130  127  124  120  118  115  113  111  109  107  106  105
```

Figure 3 IONEX data format

column size of x. After that linear regression is applied to each coefficients. The predicted value of each DCT coefficient C is obtained using equation:

$$Cp,q[t_0+v]=w_0+\sum_{u=1}^{U} w_u * Cp,q[t_0-u+1] \quad (7)$$

In equation, t_0 is the time index of the last input GIM map, v is the number of maps ahead, w_0 and w_u are the regression coefficients over time and U is the number of GIM maps which were backwards taken into account. Obtained regression coefficients are applied to the prediction set. Prediction model can be fed by additional physical information, such as Solar Radio flux *SFD*, Sunspot number *SSN*, *Kp* index and ionospheric parameter *GEC* (Global Electron Content) (Hernandez-Pajares *et al*, 2009). Example of IONEX data is presented on Figure 3.

The IONEX data, both predicted and final were extrapolated for the specific location, as presented further. The elaborated position is situated in the Northern Adriatic Area, being the subject of space weather research during recent years (Filjar *et al*, 2009; Filjar *et al*, 2011; Filjar *et al*, 2013; Brčić *et al*, 2014).

3 NORTHERN ADRIATIC GIM OBSERVABLES

VTEC data were collected and analysed for years 2011 and 2012, after which the year 2012 was selected for further research. Measurements were gathered for the specific position in the Area (Figure 4), providing highest VTEC values and daily VTEC fluctuation.

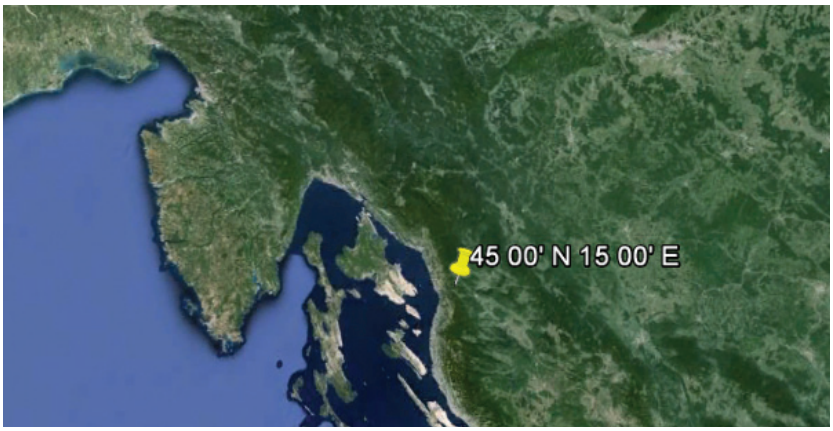

Figure 4 GIM Northern Adriatic position, latitude 45° N/longitude 015°E

The greatest VTEC value (45.7) was detected on 67th day at 12 UTC. 95% of VTEC over 40.0 was detected at 12 UTC where the Sun was at its culmination point. For 2012 average VTEC was 17.4.

Three different types of daily patterns of VTEC were detected. First type of pattern is when the peak of VTEC occurs in midday (approx. 12 UTC). This known type of daily fluctuation is most common and in 366 analysed days occurs during 254 days (approx. 69 %), and it is already defined in the standard GPS ionospheric delay model (Klobuchar, 1987). It is noticeable that first-type fluctuation occurs during winter, spring and fall when the sun was away from position where data was gathered.

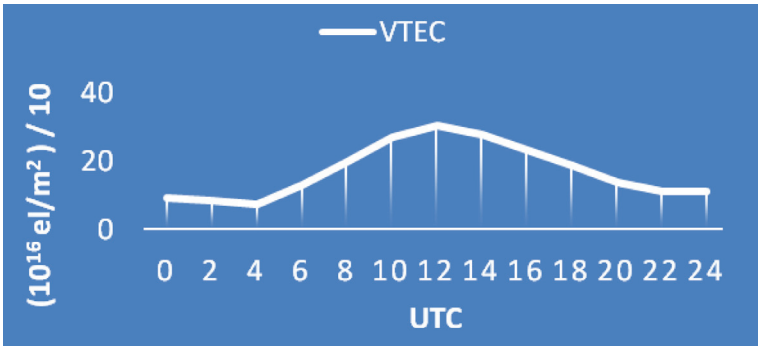

Figure 5 Daily pattern of TEC for day 74, 2012

Second type of daily pattern is marked with two VTEC peaks during the day. First peak occurs at approximately 12 UTC followed by the second at 18 UTC. In analysed years this type of daily fluctuation occurred during 99 days (27%), mostly during May, June, July, August and September.

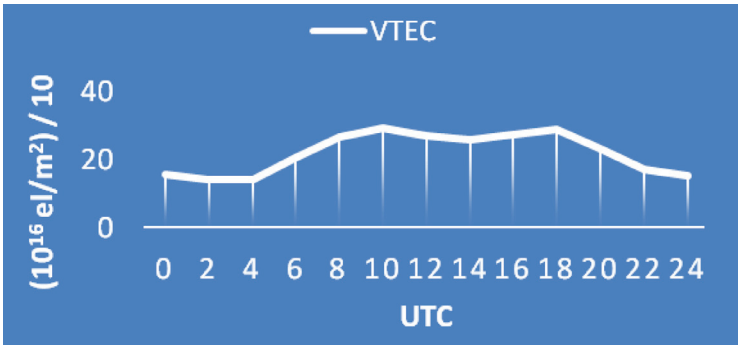

Figure 6 Daily pattern of TEC for day 191, 2011

Third type of daily pattern has three peaks, occurring before, at and after the Sun's culmination.

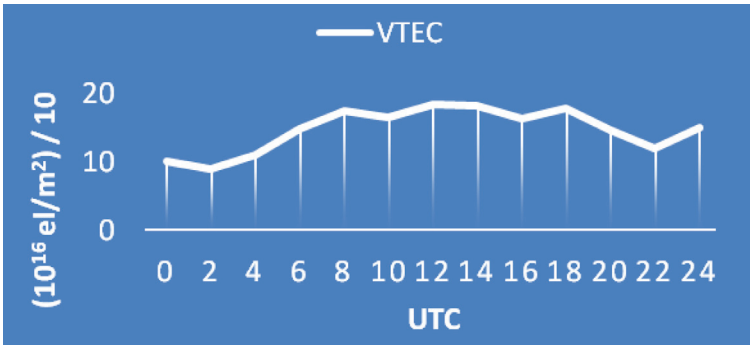

Figure 7 Daily pattern of TEC for day 190, 2011

Annual occurrence of identified VTEC daily pattern types is shown in Table 1.

Table 1 Distribution of three types of daily fluctuation pattern by each month during 2012

Month	Fluctuation pattern type		
	1	2	3
Jan	31	0	0
Feb	24	5	0
Mar	26	5	0
Apr	28	2	0
May	8	21	2
Jun	8	16	6
Jul	9	18	4
Aug	11	20	0
Sep	22	7	1
Oct	29	2	0
Nov	30	0	0
Dec	28	3	0
Total	254	99	13

The additional pattern types in the Northern Adriatic region were already detected during the previous research (Brčić *et* al, 2014; Filjar *et al*, 2011), with current exploration being confirmation of local ionospheric delay anomalies. The following chapter deals with predicted and final VTEC analyses obtained through year 2012.

4 ANALYSIS OF VTEC RESIDUALS

By comparing measured and predicted VTEC it is possible to determine residuals (RE), i.e. differences between real (RV) and predicted (PV) VTEC:

$$RE = RV - PV \tag{8}$$

It is evident that residuals can be positive and negative. Using statistical tools and equations deviation and variation of residuals can be determined. The average absolute deviation from the arithmetic average is 21.05, variance is 920.06 and standard deviation is 30.33. Positive residuals occurred on 1727 measurements, negative residuals on 2577 measurements and there were no residuals on 88 measurements. The biggest deviation of predicted VTEC from final VTEC was +20.0, occurring on day 67 at 12 UTC, and –15.8 on day 115 at 10 UTC, respectively. To properly compare final and predicted TEC data were divided into four groups by seasons.

In winter there were 89 days with 1068 VTEC measurements. In that time period there were 10 days with second type of daily VTEC pattern. Data is shown in Figure 8.

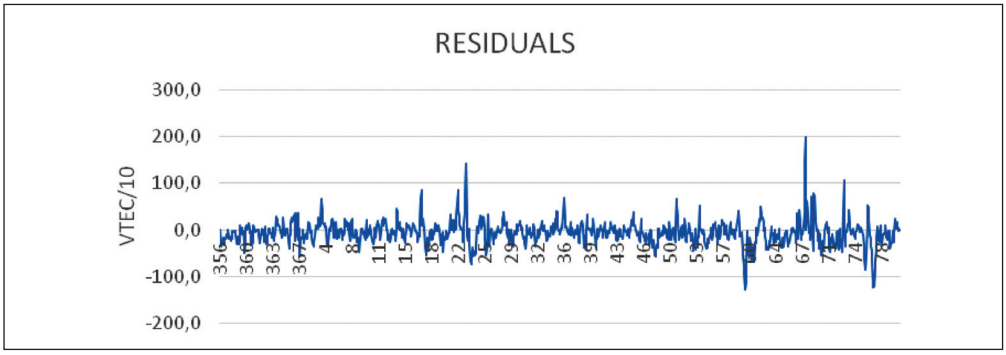

Figure 8 VTEC residuals from December 22nd 2011 to March 20th 2012

In spring there were 91 days with 1092 measurements of VTEC. As shown in Figure 9 it can be seen that residuals are positive, which means that final VTEC was greater than predicted. In this period second and third type of daily VTEC pattern occurred during 39 days.

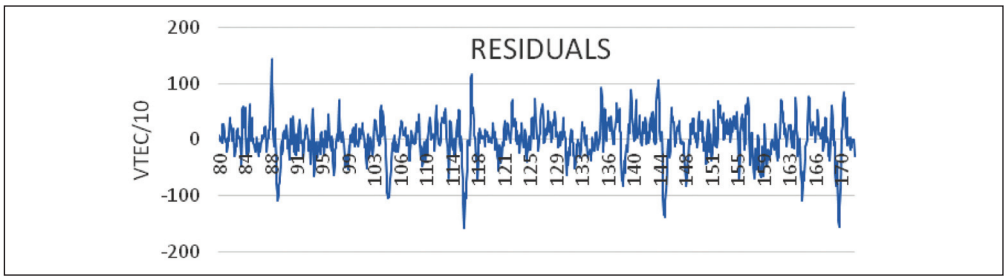

Figure 9 VTEC residuals from March 21st to June 21st 2012

In summer there were 106 days with 1272 VTEC measurements. In that time period second and third type of daily TEC pattern occurred on 57 days or 54% of time. Residuals for this time period are shown in Figure 10.

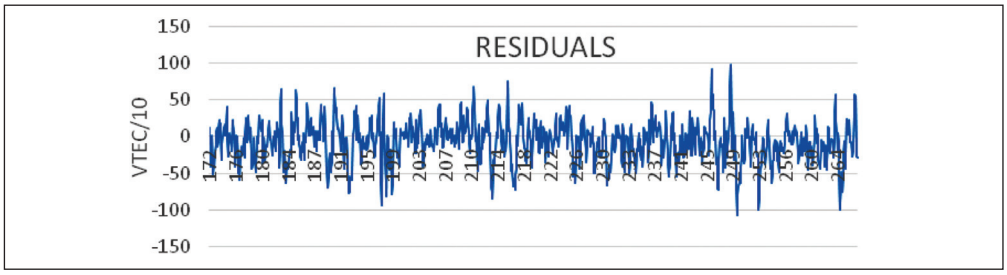

Figure 10 VTEC residuals from June 22nd to September 23rd 2012

In autumn there were 87 days with 1044 VTEC measurements. In that time period second and third type of daily VTEC pattern occurred only on 5 days, so on 94% of days was first type of TEC daily pattern. In Figure 11 are shown data of VTEC residuals for autumn.

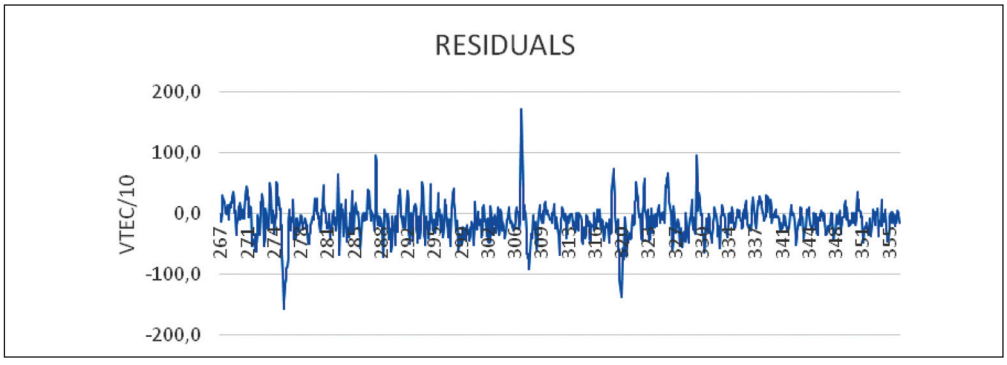

Figure 11 VTEC residuals from September 24th to December 21st 2012

In 2012 there were seven days with very high VTEC and high residuals, respectively. These days were chosen for further analysis. Geomagnetic indices (*Kp*, *Dst*[1] and *dBdtF*[2]) were involved, as well as solar SFD parameter (SPIDR 2014, WDC 2014). To get a better picture about residuals one day before and after was also selected and analysed. In most of selected days *Kp* index went over 4 approximately 12 h after large residuals were detected, meaning that final VTEC was high and predicted VTEC (PTEC) was not. The result was that other day *Kp* index was low (under 4) and the residuals were also high (now negative). That means that predicted VTEC was high and final VTEC was not. Also at the time of high Final VTEC (FTEC) spike of *dBdtF* was also detected. Results are shown in Figure 12.

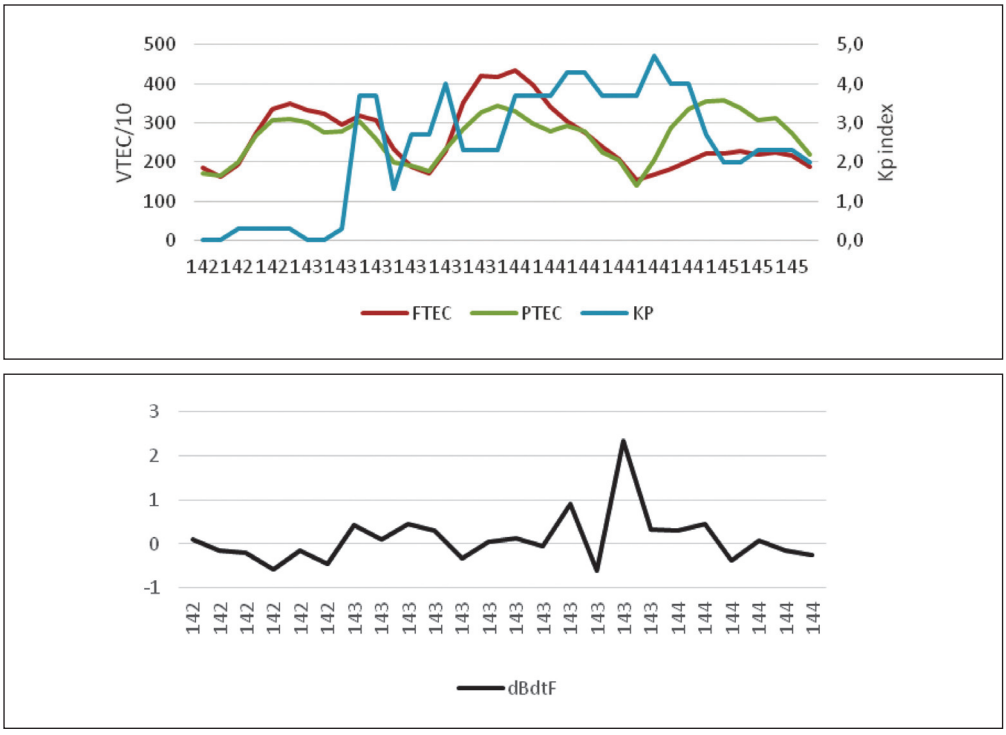

Figure 12 Final VTEC, Predicted VTEC, Residuals, Kp index and dBdtF for days 142 to 145, 2012

Mentioned indices were used for the classification tree model generation. First task was to determine possible correlation between parameters, by using Pearson correlation:

$$r = \frac{n(\sum xy) - (\sum x)(\sum y)}{\sqrt{\left[n\sum x^2 - (\sum x)^2\right]\left[n\sum y^2 - (\sum y)^2\right]}} \quad \textbf{(9)}$$

The raw scores are centred by subtracting out the mean of each variable, and the sum of cross-products of the centred variables is accumulated. The denominator adjusts the scales of the variables to have equal units. This equation describes *r* as the centred and standardized sum of cross-product of two variables and that the absolute value of the numerator is less than or equal to the denominator. Therefore, the limits of ±1 are established for *r* (Rodgers *et al*, 1988).

A dendrogram is a tree-structured graph used to visualize the result of a hierarchical clustering calculation. The horizontal distance between nodes shows the correlation, in a manner that grater the distance between nodes means less correlation and smaller the distance between nodes means greater correlation. On figure 13, hierarchical dendrogram is shown, indicating measurable correlation between Final VTEC and *Kp* index.

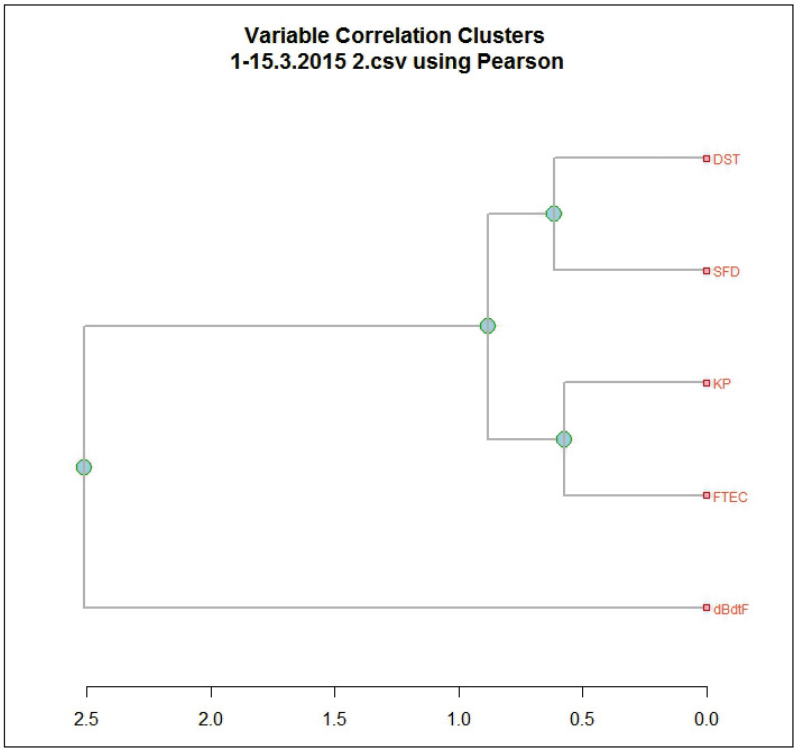

Figure 13 Correlation between model parameters (dendrogram)

In the decision tree model (Figure 14), Final VTEC was set as target variable. The used dataset was filtered for days with $Kp > 4$. The model consists of one root and one node. The input parameter in the root is *Kp* index. The first rule was to determine if the Kp index is lower or higher than 5. If is higher the Final VTEC will be around 30.5, otherwise *DST* has to be determined. The rule in this node is *DST* value, and depending on that value Final VTEC is determined. This is just basic model with few input parameters and more detailed analysis should be done to have better VTEC prediction. In Table 2, parameters of the presented model are presented.

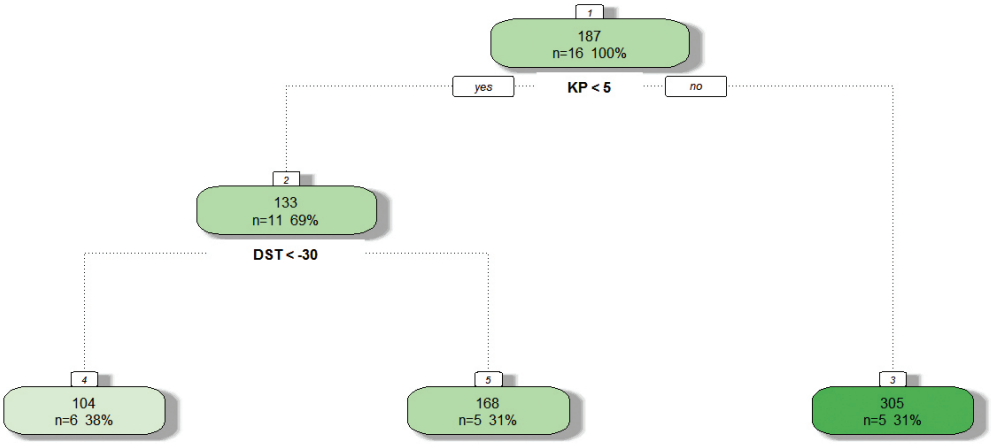

Figure 14 Decision tree model for predicting Final VTEC

Table 2 Decision tree model parameters

	Complexity parameter [*cp*]	**Number of terminal splits [*nsplit*]**	**Relative error [*rel error*]**	**Cross validation error [*xerror*]**	**Standard deviation [*xstd*]**
1	0.59976	0	1.00000	1.19471	0.46881
2	0.06628	1	0.40024	0.86386	0.22802
3	0.01000	2	0.33396	0.92670	0.22762

The evaluation of the model showed 61.38% of accuracy in terms of observed versus predicted values, presented in form of pseudo R-square coefficient of determination (Figure 15), meaning that the residual error on days with Kp index over 4 can be reduced by half. Predicted VTEC which is available 9–16 hours before Final VTEC maps will have reduced error by 50% and will give more reliable results in other models where used.

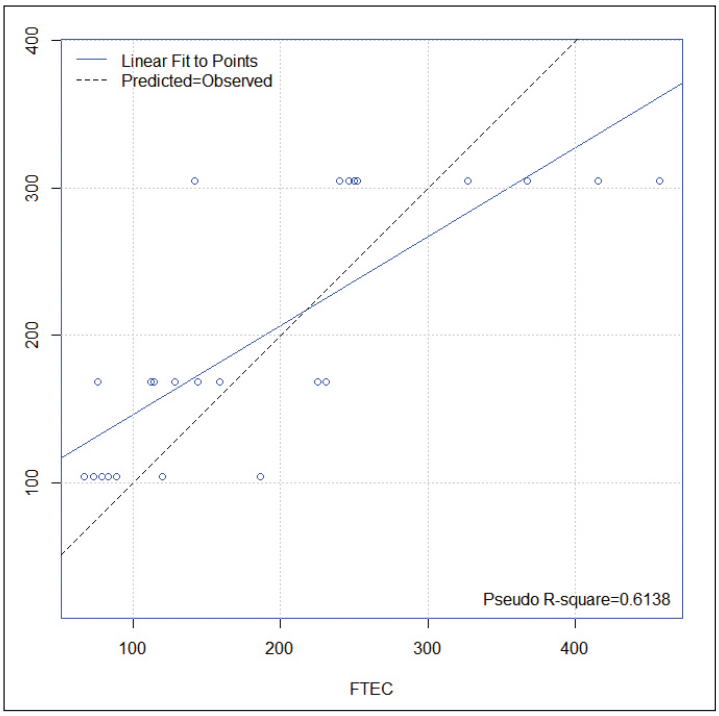

Figure 15 Decision tree model accuracy testing

5 CONCLUSION

In the proposed paper, discrepancies between final and predicted VTEC were analysed by obtaining residuals through year 2012. Comparison showed that the largest residuals were detected during increased solar and geomagnetic activity. Residuals are result of inaccuracy of the prediction model, not as a mistake, but due to delayed geomagnetic activity data. The geomagnetic component in the model gives prediction of increased VTEC day after the geomagnetic activity started, resulting in high predicted VTEC and low final VTEC. One of recognised key factors is the *Kp* index, analysis of which showed that discrepancies were significantly high in times of increased geomagnetic activity. The correction model was introduced by elaborating features of geomagnetic and solar activity and by isolating days with increased *Kp* index (> 4). The proposed model gives corrected predicted VTEC in form of residuals reduction.

IONEX total electron content analyses confirmed various ionospheric delay daily patterns in the Northern Adriatic region, with GIM VTEC acting as an independent

source of ionospheric data. Besides usual, Klobuchar-like ionospheric delay pattern, the Northern Adriatic region experiences different VTEC daily behaviour which, so far, can be categorised as two additional pattern types. Each type occurs in specific annual time period (season) and under the similar space weather activity level. Specific regularities can be identified from the collected data; however more extensive validation is necessary in terms of solar cycle and space weather activity levels, as well as extending the analyses on other areas. The proposed research acts as a continuation of geomagnetic and ionospheric environment exploration over the Northern Adriatic area, with contribution to understanding of local ionospheric dynamics. The future work should consist of further predicted and final VTEC analyses over complete GIM grid of the region, as well as IGS stations VTEC data, with the aim of broader insight of ionospheric influences on satellite positioning signals.

Acknowledgments

The presented research was conducted within the project entitled Research into the Correlation of Maritime Transport Elements in Maritime Traffic: Satellite navigation segment, supported by the University of Rijeka, Republic of Croatia.

REFERENCES

[1] Bilitza, D. (2002). Ionospheric Models for Radio Propagation Studies. In: Stone, W. R. (ed.) Review of Radio Science 1999–2002. New York: John Wiley & Sons.

[2] Brčić, D., Filjar, R. and Kos, S. (2014). On identification of local GPS ionospheric delay anomaly in the Adriatic Sea area. Proceedings of the 34th International Conference on Transportation Systems (KoREMA), pp. 112–115. Dubrovnik, Croatia, 5–9.11.2014.

[3] CDDIS. The Crustal Dynamics Data Information System. (2014). GNSS Atmospheric Products/Ionosphere. [Online] Available at: http://1.usa.gov/1zQJirj (02.05.2014)

[4] Dawidowicz, K.(2011). Comparison of using relative and absolute PCV corrections in short baseline GNSS observation processing. Artificial Satellites 46.1, pp. 19–31.

[5] Dyrud, L. et al. (2008). Ionospheric measurement with GPS: Receiver techniques and methods. Radio Science, 43.6, pp. 1–11.

[6] Filjar, R., Brčić, D. & Kos, S. (2013). Single-frequency Horizontal GPS Positioning Error response to a moderate Ionospheric storm over Northern Adriatic. In: Weintrit, A. (ed.): Advances in Marine Navigation, pp. 49–56. Boca Raton: CRC Press.

[7] Filjar, R., Kos, S. and Brčić, D. (2011). Local model of quiet space weather GPS ionospheric delay for the area of Northern Adriatic. [unpublished] 5th GNSS Vulnerabilities and Solutions Conference. Baška, 23–25.05.2011. London: The Royal Institute of Navigation.

[8] Filjar, R., Kos, T. & Kos, S. (2009). Klobuchar-Like Local Model of Quiet Space Weather GPS Ionospheric Delay for Northern Adriatic. Journal of Navigation, 62.3. pp. 543–554.

[9] Hernandez-Pajares, M., et al. (2002). Combining GPS measurements and IRI model values for space weather specification. Advances in Space Research, 29.6, pp. 949–958.

[10] Hernández-Pajares, M., et al. (2009). The IGS VTEC maps: a reliable source of ionospheric information since 1998. Journal of Geodesy 83. 3-4, pp. 263–275.

[11] Klobuchar, J.A. (1987). Ionospheric Time-Delay Algorithm for Single-Frequency GPS Users. IEEE Transactions on Aerospace and Electronic Systems, 23.3, pp. 325–331.

[12] Komjathy, A., Langley, R.B. (1996). The effect of shell height on high precision ionospheric modelling using GPS. Proceedings of the 1996 IGS Workshop International GPS Service for Geodynamics (IGS). Vol. 203.

[13] Lee Rodgers, J., Nicewander, A. (1988). Thirteen ways to look at the correlation coefficient. The American Statistician 42.1, pp. 59–66.

[14] Mannucci, A.J., et al. (1998). Global mapping technique for GPS-derived ionospheric total electron content measurements. Radio science 33.3, pp. 565–582.

[15] Mannucci, A.J., et al. (1999). GPS and ionosphere. Review of Radio Science 1996–1999, pp. 625–665.

[16] NGDC SPIDR. National Geophysical Data Center's Space Physics Interactive Data Resource. (2014). [Online] Available at: http://1.usa.gov/10EEcPt (03.05.2014)

[17] Parkinson, B. W., Spilker, J.J. (eds.) (1996). Global Positioning System: Theory and Applications. Volume I. Washington, DC: AIAA.

[18] Schaer, S., Werner G. and Feltens, J.(1998). IONEX: The ionosphere map exchange format version 1. Proceedings of the IGS AC workshop, Darmstadt, Germany. Vol. 9. No. 11.

[19] WDC Kyoto. World Data Center for Geomagnetism. (2014). [Online] Available at: http://bit.ly/1wNdOP9 (01.12.2014)

Faculty of Maritime Studies
University of Rijeka, Croatia
University of Zagreb
Faculty of Transport
and Traffic Sciences
Royal Institute of Navigation
Science Technology Practice
9th
Annual
Baška GNSS
Conference

ANALYSIS OF IONOSPHERIC DISTURBANCE OVER EUROPEAN MIDDLE LATITUDES

Tomislav Kos, Josip Vuković, Frane Šižgorić

University of Zagreb, Faculty of Electrical Engineering and Computing, Zagreb, Croatia
E-mail: tomislav.kos@fer.hr

ABSTRACT. *The paper analyses variability of the ionospheric Total Electron Content (TEC) over European middle latitudes, obtained from Global Navigation Satellite Systems (GNSS) observations. Although characteristics of the ionospheric activity at middle latitudes are usually well modelled compared to low and high latitudes, models usually do not take into account the local irregularities and response very slowly to fast developing ionospheric disturbances. To detect ionospheric irregularities and obtain information of ionospheric gradients, we used the TEC rate of change (ROT) and calibrated vertical TEC (VTEC) data. For observation of spatial behaviour of ionospheric fluctuations we used TEC data from several GNSS stations situated in the same geographical area. A tool for geographical representation of VTEC values and the TEC rate of change (ROT) was developed. Produced graphical and numerical representation was used for preliminary analyses of ionospheric fluctuations over middle latitudes during the periods of low and high geomagnetic activity.*

KEY WORDS: *GNSS, ionosphere, Total Electron Content, ROT, ionospheric disturbance*

1 INTRODUCTION

The Sun is constantly radiating electromagnetic waves over a range of frequencies. There is considerable variability of the radiation during increased solar activity periods in extreme ultraviolet, X-ray and radio wavelengths. During these periods the Sun is also generating high-energy solar particles and the solar wind (Bothmer, 2007). The ionising radiation, the ionised particles and the plasma interact with the Earths' magnetosphere and ionosphere, causing a variety of effects on Global Navigation Satellite Systems (GNSS) and other engineered systems. The consequences are disturbances called geomagnetic storms. The impact of the ionosphere is predominantly emphasised in the storm periods. The ionosphere affects the propagation of radio waves and the operation of GNSS systems, inducing range errors in GNSS generated navigation solutions. During particularly active periods, solar radio bursts at GNSS frequencies can also cause loss of lock in GNSS receivers due to increase in radio interference. Solar radio bursts are coincident with the solar flares and can last for a few minutes to a few tens of minutes. Plasma particles associated with the coronal mass ejections cause perturbations to the ionospheric electron density over large portions of the globe and cause large scale structures (hundreds of km) and gradients in the ionosphere. Small-scale structures (< 1 km) are also generated and these cause rapid changes in amplitude and phase of the signals (scintillation) (Carrano and Groves, 2007).

Ionospheric delay is a dominant error source in GNSS positioning. Ionospheric disturbances and changes in the Total Electron Content (TEC) determine the first order ionospheric induced range error. TEC also describes the background state of the ionosphere. Although a number of ionospheric models have been proposed in order to tackle the impact of the ionospheric delay on GNSS positioning accuracy, those models usually do not take into account local irregularities in the ionosphere and response very slowly to fast developing disturbances. TEC spatial and temporal gradients can significantly influence GNSS performance and increase the error in absolute, as well as in relative positioning.

2 TEC FLUCTUATIONS MONITORING USING GNSS DATA

International GNSS Service (IGS) operates a global network of GNSS tracking stations and data analysis centres to provide GNSS data and derived data products essential for Earth science research, positioning, navigation and timing (PNT) applications and education. IGS monitoring stations provide GNSS observation data sets with time resolution of 30 s. Dual-frequency GNSS receivers measure

two observables for each tracked satellite: carrier-phase observables and code-delay observables at each frequency (Shagimuratov et al, 2013). The process of levelling carrier-phase to code-delay observables is affected by inter-frequency biases (IFB) produced by the receiver and satellite hardware. The process of estimation and removal of IFB is often called TEC calibration. We used Ciraolo calibration procedure that requires the observation and navigation Receiver Independent Exchange Format (RINEX) files from the day before and the day after the observed day (Ciraolo et al, 2007). Such a data set contains full satellite arches and is used in the process of carrier-phase to pseudorange levelling in order to get TEC results as accurate as possible, avoiding the occurrence of negative TEC.

Knowing the amount of ionospheric error does not only allow its removal in order to minimize positioning error, but also allows monitoring of the ionospheric conditions on the signal paths. In the data processing, a single shell approximation of the ionosphere with a height of 350 km was used. In such approximation, the total amount of TEC is considered to be located on a point where the signal from a satellite, on its way to a receiver, cuts the presumed thin shell. That point is called Ionospheric Piercing Point (IPP) and the amount of associated vertical TEC (VTEC) describes the ionospheric conditions on the points' coordinates (Wang et al, 2014).

Spatial information on ionospheric gradients can be obtained differentiating the TEC values measured on different IPP coordinates in the same time epoch. This method presumes the TEC calibration in order to have values between different satellite-receiver pairs comparable. Another method of deriving gradient information is differencing TEC of a certain satellite between adjacent time epochs. This method can provide temporal and shorter distance gradients, it is not necessary to use calibrated TEC values as only relative variations are considered, but the temporal and spatial variations cannot be separated. The product of this method is called TEC Rate Of Change (ROT) and expressed in TEC unites per minute for each satellite (Mayer et al, 2008).

3 SELECTED IONOSPHERIC CONDITIONS AND EXPERIMENT SETTINGS

The idea of the study was to examine spatial and temporal dynamics of ionosphere, represented by TEC and ROT. Periods with quiet and disturbed ionospheric conditions were selected to define the correlation between different geomagnetic

parameters and the occurrence of large gradients. For the analysis we chose an event with high geomagnetic disturbance on 17 March 2015, known as 2015 St. Patrick's Day Storm, caused by coronal mass ejection from the Sun. Kp index, designed to measure solar particle radiation by its magnetic effects, during that day reached the value of 8 on its quasi-logarithmic scale from 0 to 9 (SWPC, 2015). We compared the behaviour of the TEC values in European middle latitudes for quiet and disturbed day to detect irregularities in the ionosphere during the disturbance. Chosen quiet day was 15 March, in order to avoid seasonal ionospheric variations. Figure 1 shows the Kp index values for the selected event, with sudden increase after 3 a.m., long lasting maximum of almost 12 hours and a decrease on the following day.

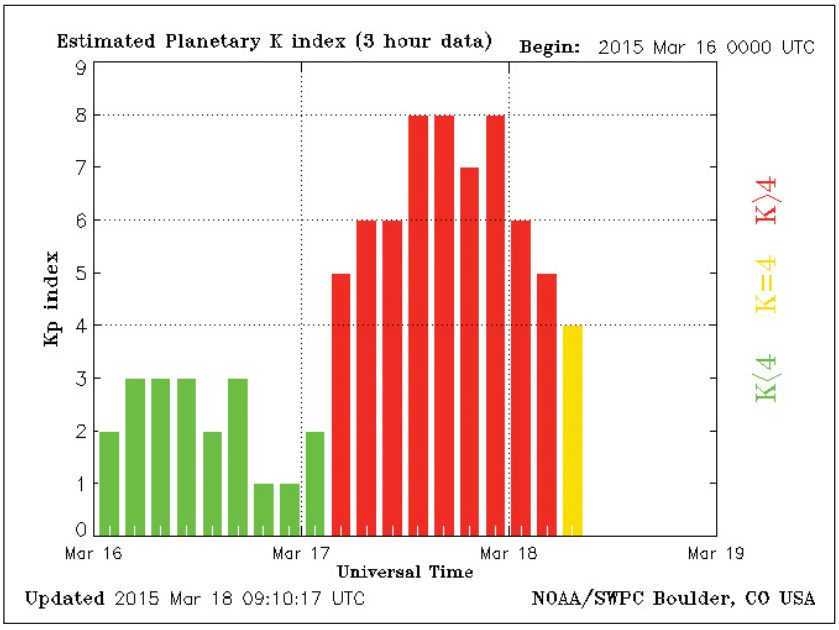

Figure 1 Kp index variation for the selected event (SWPC, 2015)

RINEX files from six GNSS stations located in European middle latitudes were collected for selected days. The IGS stations GRAZ (Graz, Austria), MEDI (Medicina, Italy), ORID (Ohrid, Macedonia), PENC (Penc, Hungary) and WTZA (Wettzell, Germany), as well as local ZGRB station in Zagreb, Croatia were used. Most stations were capable to receive both Global Positioning System (GPS) and Globalnaya Navigazionnaya Sputnikovaya Sistema (GLONASS) signals, while some received only GPS.

Calibrated TEC was calculated using Ciraolo calibration tool. VTEC on IPP of each satellite-receiver pair was selected to be used when the satellite elevation was above 20°. Such a cut-off elevation mask was applied to minimize the errors of mapping function, which was used to derive VTEC from slant TEC. An example of elevation cut-off effects on VTEC deviations for satellites visible from ZGRB station can be seen on Figure 2. Similar effects were observed for other stations in both quiet and disturbed conditions.

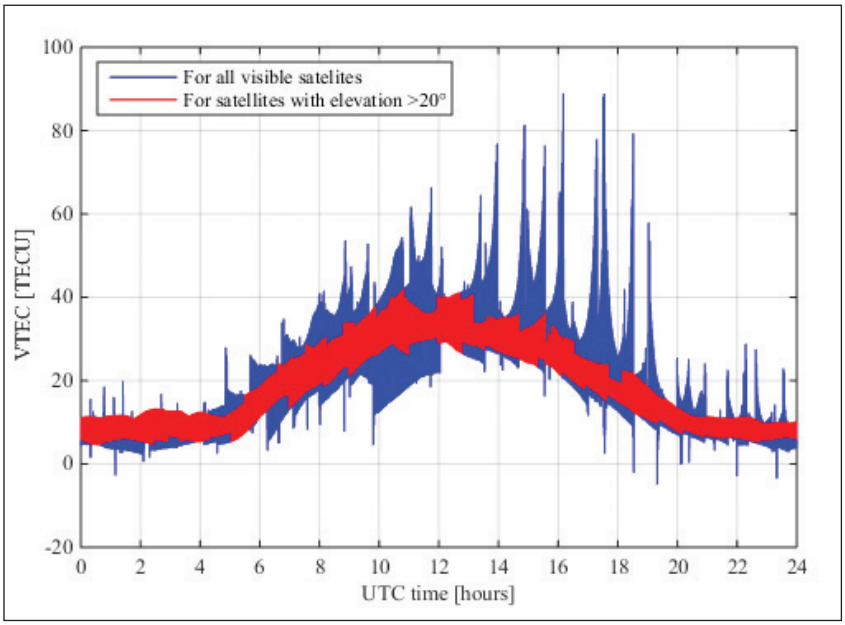

Figure 2 Daily VTEC for 15 March 2015, using all visible satellites (blue) and using only satellites with elevation above 20° (red)

Comparison of diurnal values of TEC on ZGRB station location shown on Figure 3 confirms that the increase in geomagnetic activity on 17 March translated into increased ionisation of the ionosphere with a delay of few hours. Daily peak appeared at the same time of day as it appeared on the quiet day, but was 20 TECU higher. The ionisation level remained high until the late afternoon, but dropped below the level observed on a quiet day by the end of day due the ion recombination on the night-side.

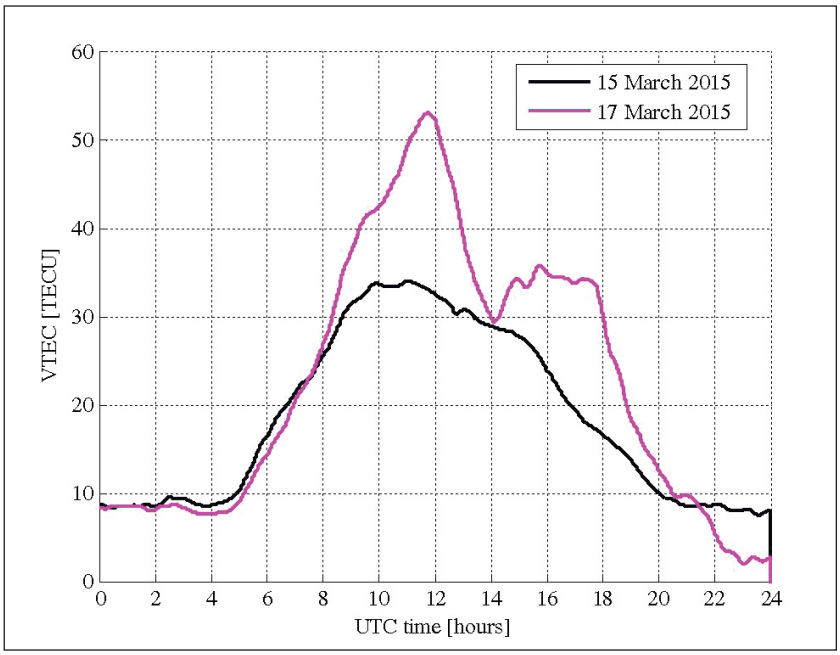

Figure 3 Interpolated VTEC for ZGRB station coordinates on quiet and disturbed day

4 RESULTS

VTEC was interpolated over the observed area using natural neighbour interpolation between the VTEC values located on IPP coordinates. The interpolation results obtained using the developed tool were presented on a map. The covered area changed in each epoch, depending on the satellite visibility and elevation, but remained in European middle latitudes. Figures 4 and 5 show VTEC on 11:10 and 16:30 UTC of 17 March 2015, respectively. IPP coordinates used in each calculation are marked with red dots. Areas with the same VTEC are marked with black contour lines, distanced 2 TECU. Even though the maximum TEC values in the observed area were reached between 11:00 and 12:00 UTC, the gradients were much higher in the afternoon, as the contours are spaced much closer to each other. The narrow observed area included values that reached form 10 to 50 TECU. Gradients were mostly directed as expected, northwest-southeast before the 14:00 local time and from northeast-southwest afterwards. However, on the north-most part of the observed area, where the gradients were highest, they were oriented north-south.

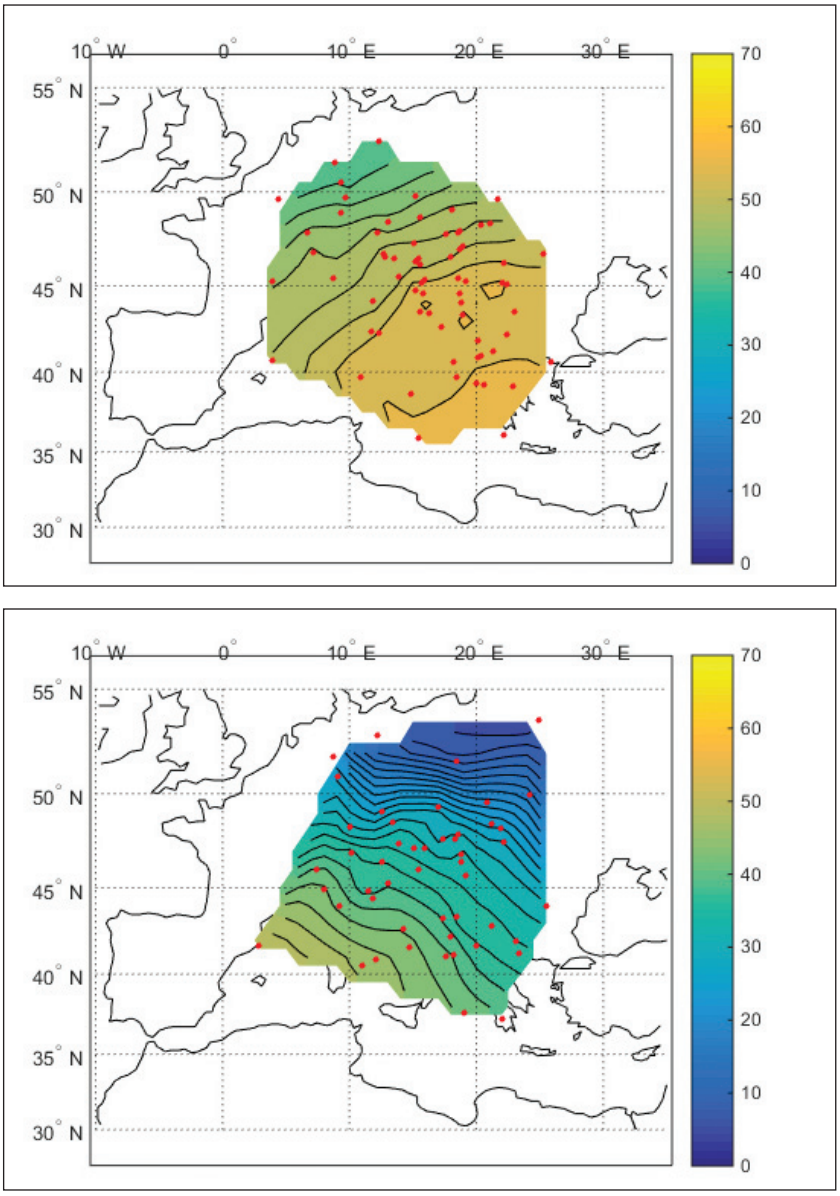

Figure 4 TEC map on 17 March 2015 at 11:10 (top) and 16:30 UTC (bottom)

ROT values for quiet and disturbed day were calculated and its magnitudes compared to determine the degree of perturbations in the ionosphere. Absolute ROT value of all visible satellites (with elevation > 20°) in each epoch was averaged. Example of ROT for satellites visible from ZGRB station on observed

days is depicted on Figure 5 and curves for other stations are almost identical. It is visible that around 8:00 a.m. curves diverge as the ionosphere gets disturbed. At the time of highest TEC on 17 March, ROT is not very high as the change is gradual and consistent over the observed area. Significant increase of ROT takes place in the late afternoon with two distinct peaks at 16:30 and 18:00 hours, with higher one reaching 0.6 TECU/min. From figures 4 and 5 it can be observed that around 16:30 over the observed area both strong spatial and temporal ionospheric gradients exist.

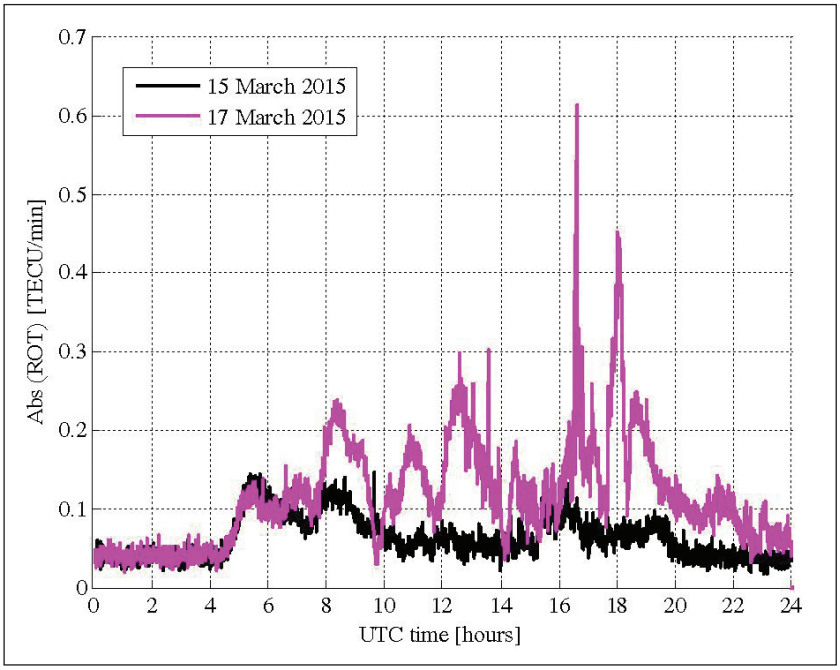

Figure 5 Daily absolute ROT on 15 and 17 March 2015

5 CONCLUSION

Ionosphere has complex dynamics, depending on different solar and geomagnetic precursors. Solar disturbances can cause effects that appear very suddenly and are hard to model. To expand our knowledge of ionospheric physics and its effects to GNSS, we observed spatial and temporal dynamics of ionospheric fluctuations on quiet and disturbed day. TEC data from several GNSS stations situated in European middle latitudes revealed that the ionosphere ionisation increased four

hours after the geomagnetic field got disturbed. Using the tool developed for geographical representation of TEC values, spatial orientation of ionospheric gradients could be revealed. The peak of the storm brought highest gradients to the observed area, even though the TEC reached its peak much earlier during the day. ROT was calculated for each satellite-receiver pair and its average confirmed appearance of high gradients in the late afternoon. Produced tools can be used for analyses of ionospheric disturbances. Further research could focus more on gradient direction and, covering larger area, provide more information on development of ionospheric disturbance and the effects observed on GNSS receivers.

Acknowledgment

The research leading to these results has received funding from the European Community's Seventh Framework Programme (FP7/2007-2013) under grant agreement n° 607081.

REFERENCES

[1] Bothmer V. and Daglis I. A. (2007). Space Weather Physics and Effects, Springer-Verlag Berlin Heidelberg

[2] Carrano C. S. and Groves K. M. (2007). TEC Gradients and Fluctuations at Low Latitudes Measured with High Data Rate GPS Receivers, Proceedings of ION 64rd Annual Meeting, Cambridge, Massachussetts, pp. 156–163.

[3] Shagimuratov I. I., Chernyak Y. V., Zakharenkova I. E., and Yakimova G. A. (2013). Use of Total Electron Content Maps for Analysis of Spatial-Temporal Structures of the Ionosphere, Russian Journal of Physical Chemistry B, Vol. 7, No. 5, pp. 656–662.

[4] Ciraolo L. et al, (2007). Calibration errors on experimental slant total electron content (TEC) determined with GPS, Journal of Geodesy, 81, Issue 2, pp. 111–120.

[5] Wang C., Wang J. and Morton Y., (2014). Regional Ionospheric TEC Gradients Estimation Using a Single GNSS Receiver, China Satellite Navigation Conference (CSNC) 2014, Proceedings: Volume II, Lecture Notes in Electrical Engineering 304, Springer-Verlag Berlin Heidelberg

[6] Mayer C., Jakowski N., Borries C., Pannowitsch T. and Belabbas B. (2008). Extreme ionospheric conditions over Europe observed during the last solar cycle, NAVITEC 2008, 4th ESA Workshop on Satellite Navigation User Equipment Technologies, Noordwijk, Netherland

[7] Space Weather Prediction Center (SWPC), National Oceanic and Atmospheric Administration, Planetary K-index, http://www.swpc.noaa.gov/products/planetary-k-index, accessed on 18 March 2015

Faculty of Maritime Studies
University of Rijeka, Croatia

University of Zagreb
Faculty of Transport
and Traffic Sciences

Royal Institute of Navigation
Science Technology Practice

9th
Annual
Baška GNSS
Conference

A RESEARCH STUDY OF HANDHELD MULTICONSTELLATION GNSS RECEIVERS SATELLITE POSITIONING PERFORMANCE

Ivo Musulin[1], David Brčić[2], Serdjo Kos[2]

[1] Ministry of Defense of the Republic of Croatia
E-mail: musulinivo@gmail.com

[2] Faculty of Maritime Studies, University of Rijeka, Croatia

ABSTRACT. *The rise and development of multi-frequency/multi-modal satellite navigation receivers provides improvements in satellite positioning accuracy and increasing positioning, navigation and timing (PNT) services integrity. The proposed research deals with positioning performance of augmented GNSS devices. Three handheld satellite navigation receivers were used in the study: GPS, GPS/EGNOS and GPS/GLONASS/EGNOS receiver, respectively. The research took place in the Middle Adriatic area, comprising static and dynamic segment. The static segment was carried out at single point location during several continuous hours, tracking obtained positions. The dynamic segment was conducted during sea navigation in confined navigation channel, where the same GNSS receivers were used for the positioning solutions obtaining. The satellite positioning environment analysis confirmed favourable positioning signals' propagation conditions and satellite availability during research periods. Obtained positioning patterns were analysed elaborating positioning errors and deviations, given the time resolution of the data obtained. The analyses were made with reference to precise-positioning service provided by dual-frequency GPS receiver which was used during the research. The reference positioning was augmented by CROPOS networked reference stations system, providing static accuracy of 3-6 mm, and dynamic accuracy of 1 – 3 cm, respectively. The results confirmed positional improvement of augmented devices, showing reduced positioning error and lesser variation scattering in multimodal GNSS receivers, when compared to sole system only. Further research activities were pointed out, originating from the conducted research and conclusions. Various environmental, operational and critical satellite positioning scenarios have to be tested, aiming at new generation satellite navigational receivers' performance studying in sea navigation.*

KEY WORDS: *global Positioning System, Global Navigation Satellite System, GLObalnaya NAvigatsionnaya Sputnikovaya Sistema, European Geostationary Navigation Overlay Service, multi-constellation, satellite positioning performance, sea navigation*

1 INTRODUCTION

The Global Positioning System (GPS) is the first fully operated satellite navigation system (SNS) controlled by the US Department of Defense (DOD). Nominal constellation consists of 24 Satellites in six orbital planes, allowing global coverage and line of sight to at least four satellites (Parkinson & Spilker, Jr. 1996). Another fully operational SNS is Russian GLONASS system (GLObal'naya NAvigatsionnaya Sputnikovaya Sistema) controlled by The Russian Aerospace Defence Forces (RISDE 2008). These two satellites systems are forming part of Global Navigation Satellite System (GNSS), among other global and regional SNSs. European Galileo and Chinese Compass/BeiDou are currently providing regional coverage. A Satellite-Based Augmentation System (SBAS) is civil system that complements GNSS providing open augmentation service from geostationary (GEO) satellites. Examples of existing SBAS are US Wide Area Augmentation Service (WAAS), the European Geostationary Overlay Navigation Service (EGNOS), the Japanese Multifunctional Transport Satellite (MTSAT) & Quasi-Zenith Satellite System (QZSS) and the Indian GPS Aided Geo Augmented Navigation (GAGAN).

The EGNOS system consists of space and ground segment, latter further comprising of control centre and ground stations network. The space segment is composed of three geostationary satellites (Inmarsat III and IV satellites and one ASTRA satellite SES-5). Ground stations gather satellite data and are developing estimates of the positioning signals integrity and accuracy, emitted by GPS. Composed signal containing correction and integrity information is then transmitted to users via GEO satellites. The service area includes most European countries (GSA 2015). EGNOS coverage is shown on Figure 1.

Differential Global Positioning System (DGPS) is another augmentation method with ground-based reference stations which broadcast corrections to improve the PNT performance. Equipped with a GPS receiver at known location, stations are transmitting positional and/or pseudorange corrections. In case of spatial corrections, reference stations are comparing own and observed GPS position, estimating the positioning error which is then provided to the user in the vicinity. In case of pseudorange corrections, reference stations are estimating the differences between measured and actual satellite pseudoranges, broadcasting the differences to the receiver (Kaplan & Hegarty, 2006).

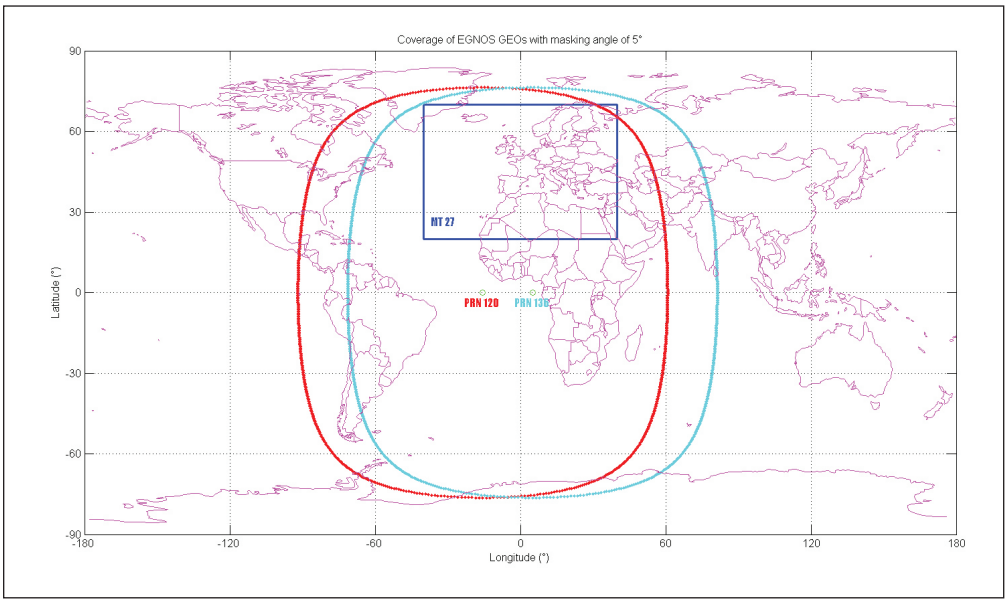

Figure 1 EGNOS satellite coverage; Inmarsat satellite 3-F2 Atlantic Ocean Region-East PRN-120 (red); ASTRA satellite SES-5 PRN-136 (green); European service area (blue) (EGNOS 2015)

The proposed study represents authors' research continuation regarding satellite positioning performance of handheld devices, both standalone and multimodal (Musulin, Kos & Brčić 2014, Kos, Brčić & Musulin 2013). The previous study contained measurements from cell phones with integrated GPS and combined GPS/GLONASS, as well as assisted receivers. Similar analyses were conducted by (Zandbergen & Barbeau 2011) in road navigation. The motivation for the emerged research is increasing usage of SNS services for nautical and similar purposes, by using handheld receivers and mobile phones. Adriatic Sea is the home of numerous types of vessels and crafts, especially during high seasons. Nautical ventures through the basin are geographically limited, especially when sailing in coastal, inter-insular and channel navigation. Considering that private devices are regularly used for non-private purposes, the aim was to prove their actual accuracy and reliability. During the research in whole, the emphasis is on new receivers' generation, where not only new SNSs are represented, but various augmentations in terms of differential and assisted means. The aim of the proposed study was the positioning error estimation in single and multi-constellation receivers (not cell phones) positioning performance, in order to confirm improvements reached with combined receivers and SBAS augmentation respectively, compared to single

frequency GPS receivers. Satellite positioning performance was conducted at a fixed point and in sea navigation. Both measurements have taken place in the littoral area of Middle Adriatic Sea in time of quiet space weather and atmospheric activity and on clear sky locations. The following section describes the methodology of the study with environmental analyses during measurement periods, as well of estimated satellite number, their visibility and relative positions. Results are presented in the third section, after which they are discussed in terms of accuracy and obtained errors estimation. In the conclusion section, the outcomes are shortly summarised, together with plans for further activities.

2 METHODOLOGY

For the purpose of the study, three types of receivers were used:

- Standalone GPS receiver (Garmin GPSmap 76CSx/SiRF STAR III, in autonomous operating mode)
- EGNOS-augmented GPS receiver (Garmin GPSmap 76CSx/SiRF STAR III, in enhanced operating mode), and
- EGNOS-augmented combined GPS/GLONASS receiver (Garmin eTrex 10/ Teseo II, in enhanced operating mode).

As a reference, dual-frequency GPS receiver (GNSS Leica RX 1220) was used further assisted with Croatian Positioning System (CROPOS) network of reference stations (CROPOS 2015). In this way static accuracy of 3–6 mm was enabled, while the positioning error remained in the 1–3 cm radius during dynamic segment of the research.

One-second data were collected at two locations within a time interval of 12 days, stored in GPX file format. Conversion to NMEA 0183 standard format was enabled by using GPSBabel software for GNSS data conversion and transfer (GPSBabel 2012, NMEA 2013). Once prepared, datasets were processed and statistical analysis was made by employing standard descriptive statistics elements, in order to estimate the positioning errors of all used devices. The results are presented after the measurement section.

Absolute horizontal positioning error was calculated as the Euclidean distance between reference and devices' positions, after which standard statistical parameters were used: minimal error, maximal error, average horizontal positioning error (HPE), 50^{th}, 68^{th} and 95^{th} percentiles, variance (VAR), standard deviation (STDEV) and root mean square error (RMSE). Prior to measurements, environmental

elements both near-user and environmental were studied, in order to define possible external effects on satellite positioning. Those are presented in the following text.

2.1 Measurements description

The static (single-point) measurement was performed on December 10th, 2012, in the period 0800-1230 LT (0700-1130 UTC), at a fixed position of φ = 43.524094° N; λ = 016.429175° E; h = 5.5 m. The surrounding was free of obstacles and electrical installations, and the sky around the site was clear in terms of mountains and other possible obstructions.

The sea-going measurement was carried out during 90 minutes (0935-1105 UTC) of navigation in the channel of 150-350 meters width. The boat speed was 3–6 knots, while the sailing route length was 6 nautical miles. The dynamic measurement was carried out on December 22th, 2012. Measurements sites are presented on Figure 2.

Figure 2 Locations of static and dynamic measurement sites

2.2 Environmental conditions and satellite visibility

Atmospheric and space weather conditions were stable and quiet during both periods. On Figures 3 and 4 satellite environment and GOES Solar X-ray Flux during both measurement periods are presented.

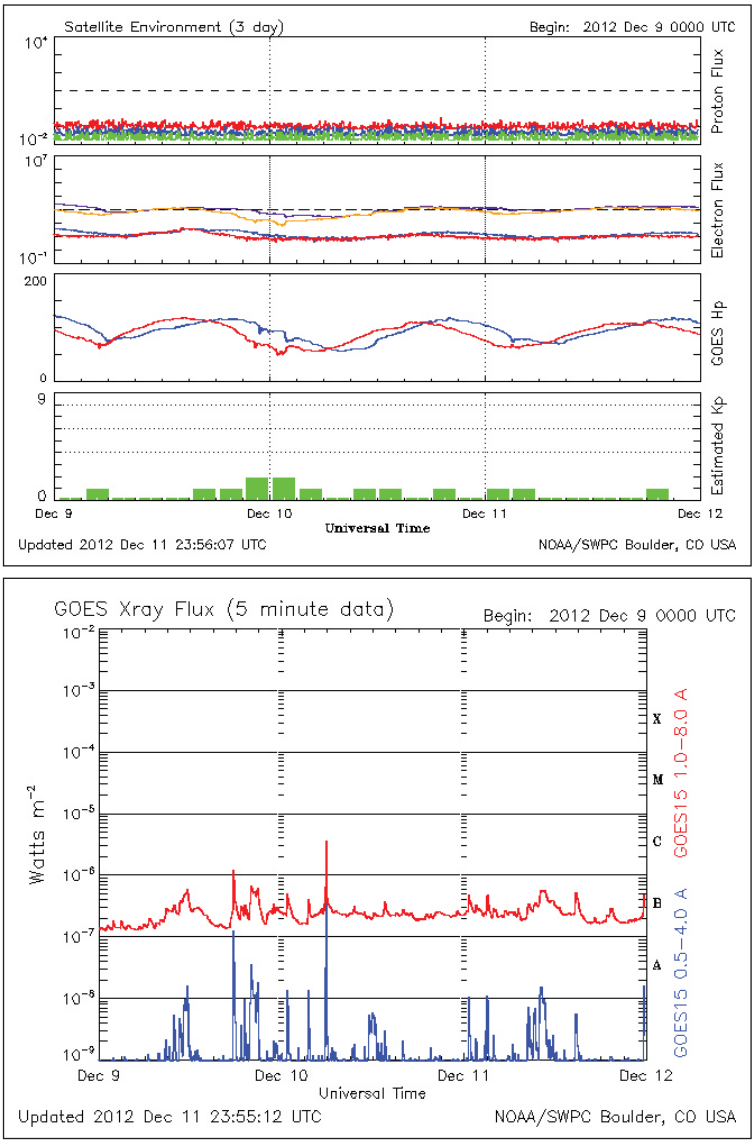

Figure 3 Space weather indices through the static measurement period (NOAA 2012)

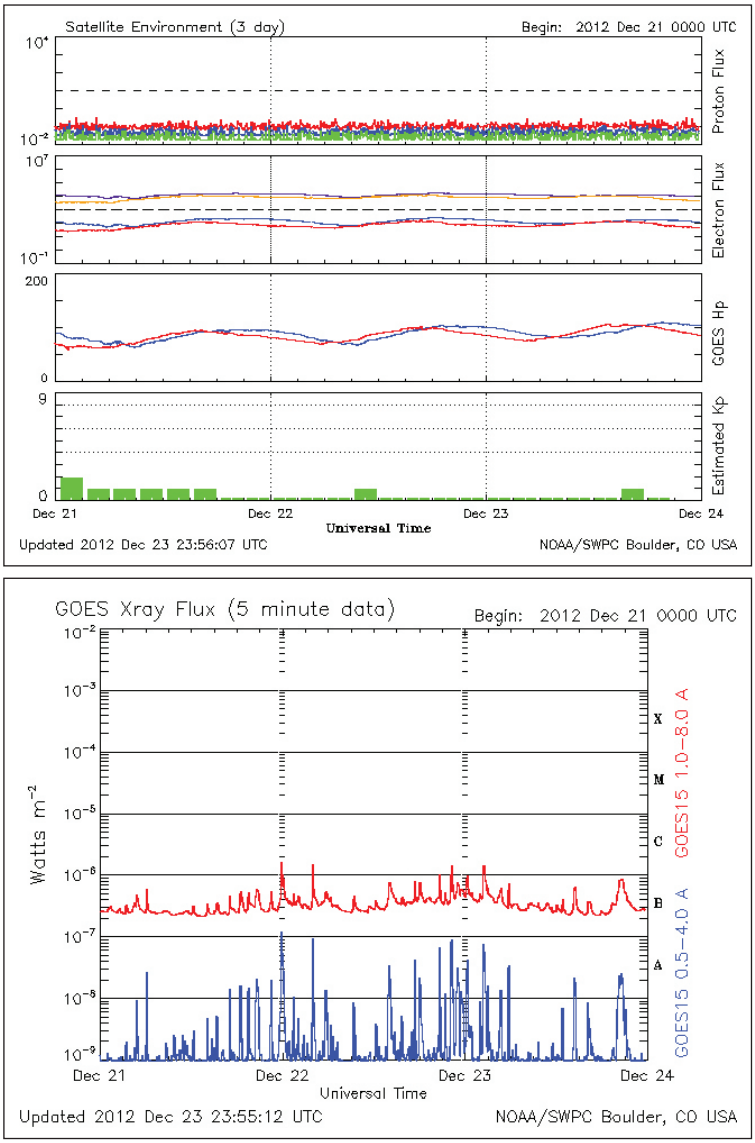

Figure 4 Space weather indices through the dynamic measurement period (NOAA 2012)

Atmospheric conditions during the period of static measurements (December 10th) are presented in Table 1.

Table 1 Atmospheric conditions during the static segment of the research

Weather	Temperature	Atmospheric pressure	Wind	Humidity
Sunny/ 1/3 cloudy	2–4° C	1008 HPa	NE 10–12 m/s	79%

During the measurement period, 5-9 GPS satellites and 4-8 GLONASS satellites were visible, with mask angle settled at 10º. Satellite visibility estimation for the measurement period is presented on Figure 5. Same parameters for dynamic measurement are presented on Figure 6.

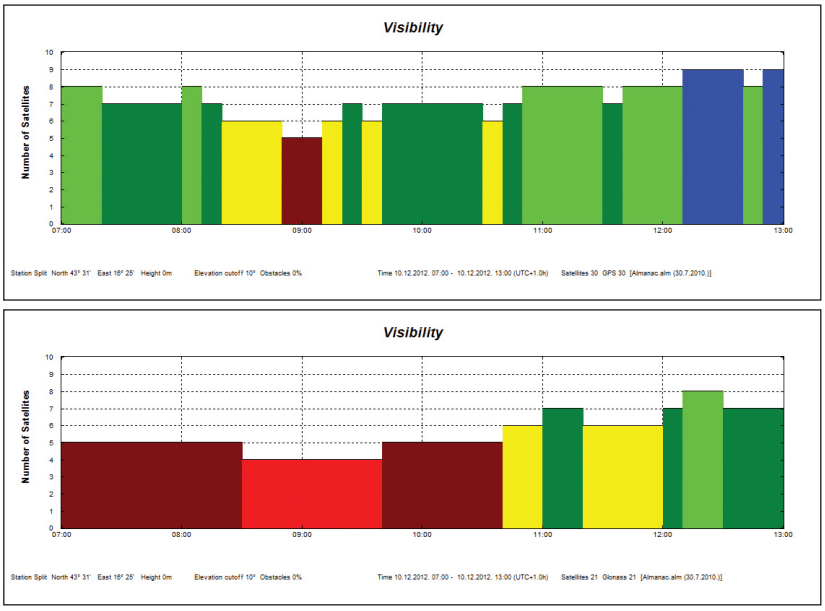

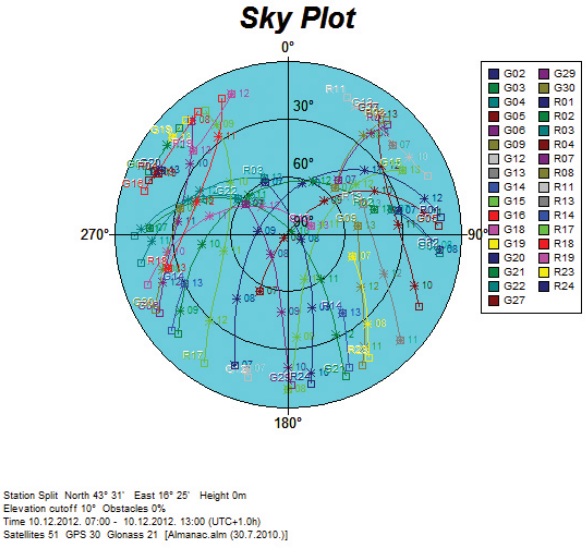

Figure 5 Number (left) and positions (right) of visible satellites during the static measurement period (TMPS 2010)

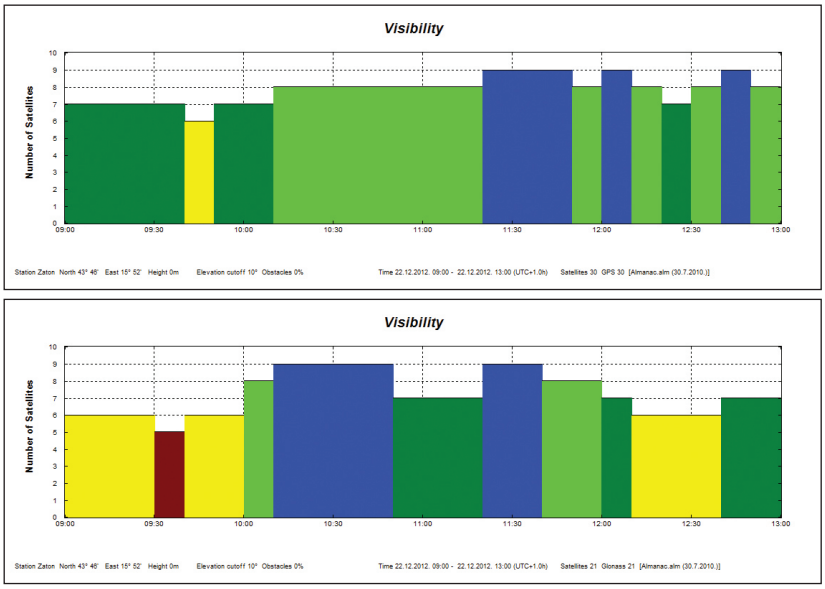

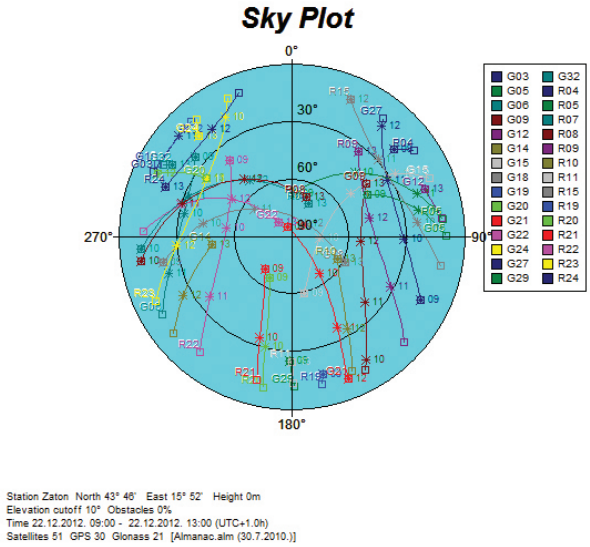

Figure 6 Number (left) and positions (right) of visible satellites during the dynamic measurement period (TMPS 2010)

In Table 2, atmospheric conditions during the sea-going (dynamic) measurement (December 22th) are presented.

Table 2 Atmospheric conditions during the dynamic segment of the research

Weather	Temperature	Atmospheric pressure	Wind	Humidity
Partly cloudy	3º C	1017 HPa	NE 7–10 m/s	67%

The number of monitored SNS satellites and the monitoring status of each satellite are given by the daily EGNOS satellite monitoring status (EGNOS 2015). Those parameters are provided in function of the User Differential Range Error Indicator (UDREI). Satellites with UDREI less than 12 are used for augmentation. On Figures 7 and 8, respectively, the monitoring status for both measurements period is presented.

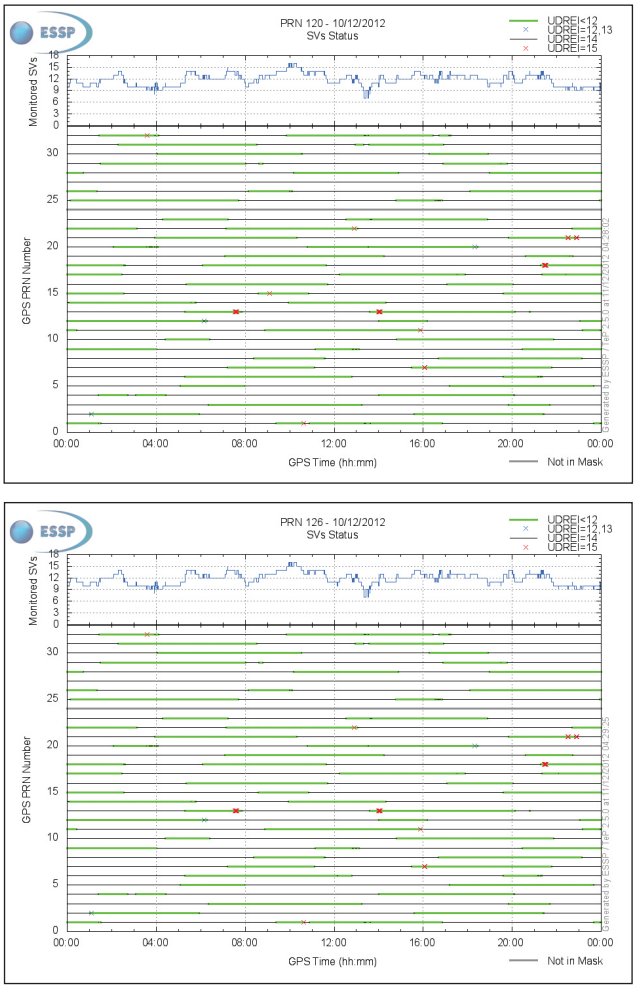

Figure 7 Daily EGNOS satellite (PRN 120 – upper and PRN 126 – lower) monitoring status through the static measurement period (EGNOS 2015)

On Figure 9, components of estimated DOP Dilution of Precision (DOP) values during both measurements' periods are presented. DOP time series were made considering both GPS and GLONASS constellations. During static measurements, DOP value did not exceeded value of 4. In two short occasions during the static measurement (0900 and 1030 LT), DOP factor increased resulting from reduced number of satellites used in positioning solution. However it remained within the permissible limits (US DOD 2008) during the observed period, making no significant effect on positioning performance.

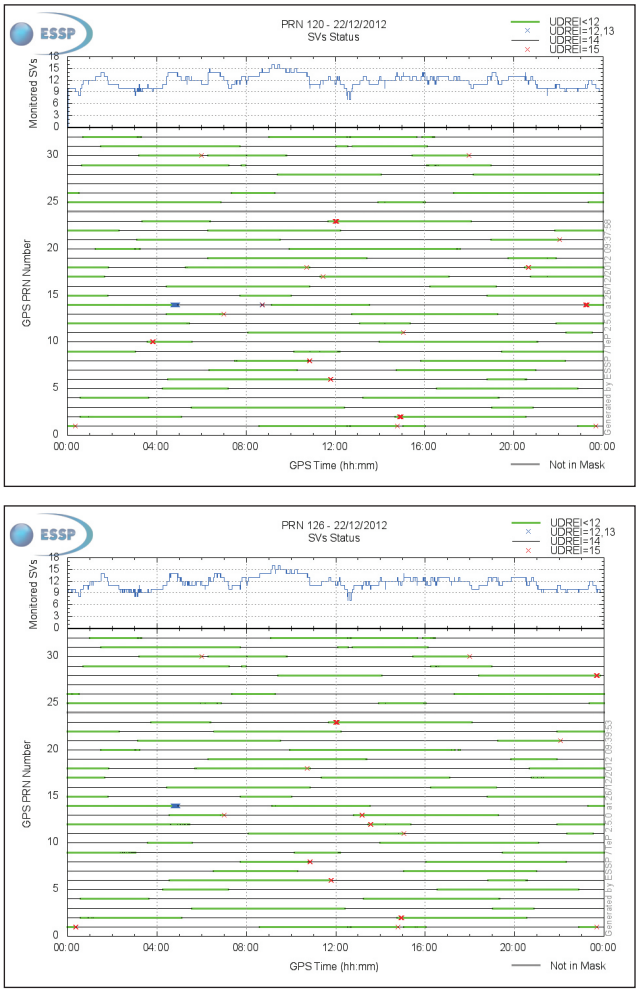

Figure 8 Daily EGNOS satellite (PRN 120 – upper and PRN 126 – lower) monitoring status through the static measurement period (EGNOS 2015)

During the dynamic measurement, DOP values remained within standard limits, in even more favourable means than in the static measurement period (not exceeding value of 3). By considering standalone GPS receiver, 7-8 GPS satellites were visible during the period. As for combined GPS/GLONASS receiver, total number of satellites providing ranging signals ranged from 15-18.

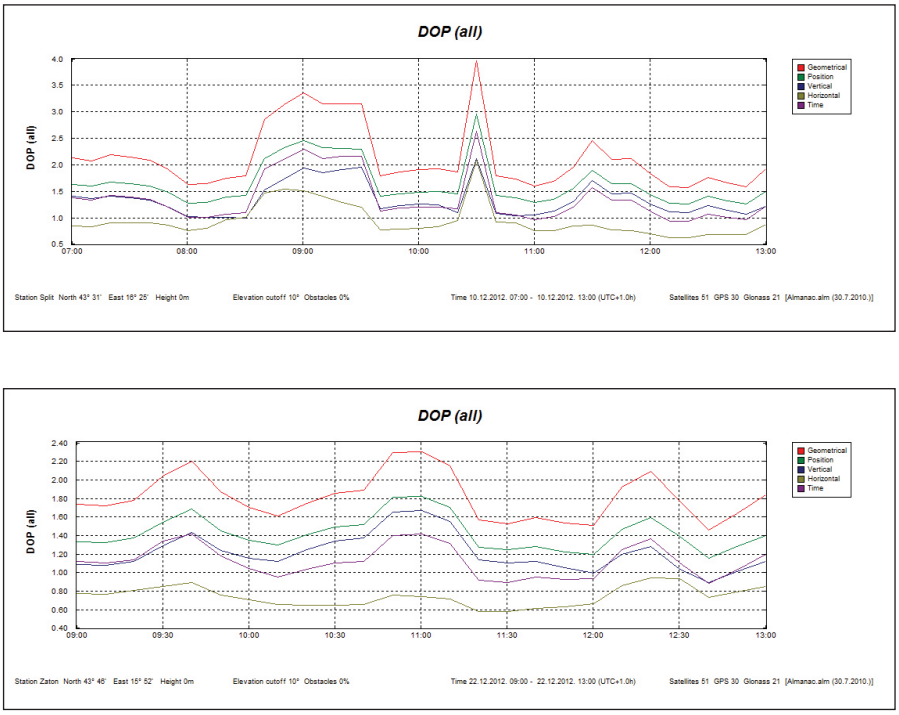

Figure 9 Dilution of precision during the static (upper) and dynamic (lower) measurement period (TMPS 2010)

In a described way, all satellite positioning influential components were elaborated. As for multipath, both location and area of measurement can be considered as free from obstacles and with satisfactory piece of sky above, what was reached with defined mask angle. The aim of this satellite and micro-environment display was to enable the monitoring of the receivers performance solely, without significant external influences which could affect the measurements. The results are presented in the following section.

3 RESULTS

The section is divided in two subchapters; in the first part, results obtained at the single location are presented, while the second part deals with results collected during navigation through the channel.

3.1 Static measurement results and analysis

Static HPE is presented on figure 10, comprising all devices' error patterns, with samples representing seconds and positioning errors given in meters. Ground Track scatterplots of each device's positioning solution during the period ($\varphi \sim \lambda$) is presented on Figure 11.

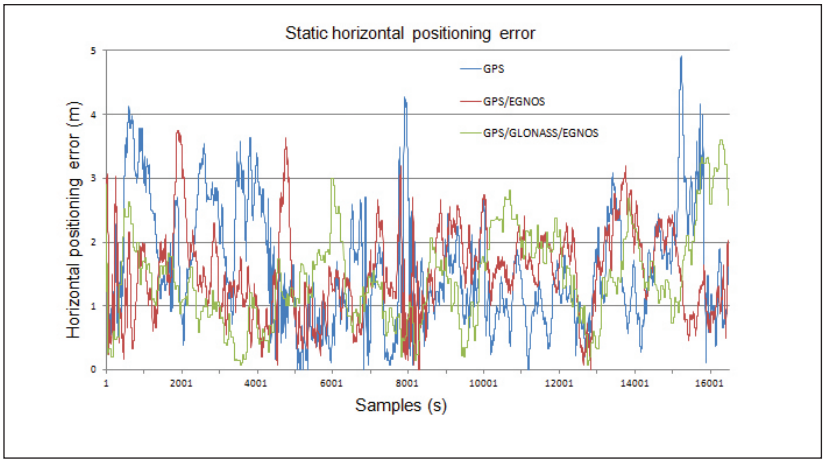

Figure 10 Absolute HPE time series during static measurement period

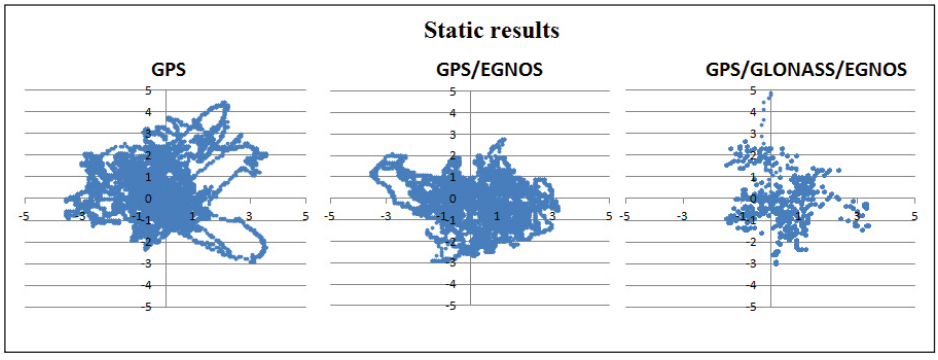

Figure 11 HPE scatterplots of absolute horizontal positioning error during static measurement period

Statistical parameters are presented numerically and graphically in Table 3 and on Figure 12, respectively.

Table 3 Static measurements statistical description

RCV	Type	Min	Max	R	AVE	50%	68%	95%	VAR	MED	RMSE	SD
Garmin 76 CSx	G	0.02	4.91	4.89	1.59	1.37	1.84	3.33	0.86	1.94	1.84	0.93
Garmin 76 CSx	G/E	0.15	3.75	3.6	1.51	1.45	1.78	2.68	0.47	1.29	1.66	0.68
Garmin eTrex10	G/ GL/E	0.08	3.60	3.52	1.42	1.36	1.70	2.82	0.55	1.06	1.60	0.74

R – Receiver; G – GPS; GL – GLONASS; E – EGNOS; R – Range; MED – Median; SD – Standard deviation

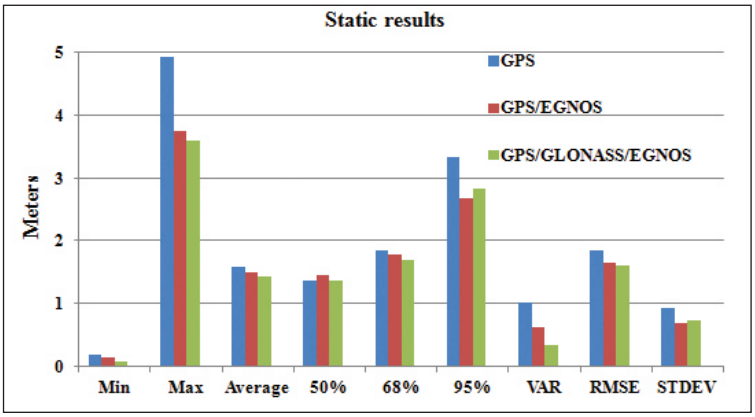

Figure 12 Graphical presentation of statistical parameters

The minimal positioning error varied from 0.08 m (GPS/GLONASS/EGNOS) to 0.2 m (GPS). Maximal error was in the range from 3.60 m (GPS/GLONASS/EGNOS) to 4.91 m (GPS). Average positioning error varied from 1.42 m (GPS/GLONASS/EGNOS) to 1.59 m (GPS). Variance was in the range from 0.34 to 1.01. RMSE varied from 1.60 m (GPS/GLONASS/EGNOS) to 1.84 (GPS). SD varied from 0.68 m (GPS/EGNOS) to 0.93 m (GPS). The range of error was most pronounced in GPS receiver, while combined and augmented receiver showed the smallest range. However, average error scattering (SD) was greater in the GPS/GLONASS/EGNOS receiver than in the combined GPS/GLONASS.

Garmin GPSmap 76CSx receivers have shown better static horizontal positional accuracy using GPS augmented by EGNOS, when compared to autonomous GPS. Statistical analyses have shown increase in horizontal accuracy in eight out of nine statistic tests.

Garmin eTrex10 receiver has shown better static horizontal positional accuracy using GPS augmented by GLONASS and EGNOS in comparison with Garmin GPSmap 76CSx. Statistical analyses have shown increase in horizontal accuracy in all statistic test when comparing Garmin eTrex10 (GPS/GLONASS/EGNOS) with Garmin GPSmap 76CSx (GPS) and in eight out of nine statistic tests when compared with GPS/EGNOS device EGNOS.

3.2 Dynamic measurement results and analysis

Obtained positioning error patterns recorded during navigation are shown on Figure 13.

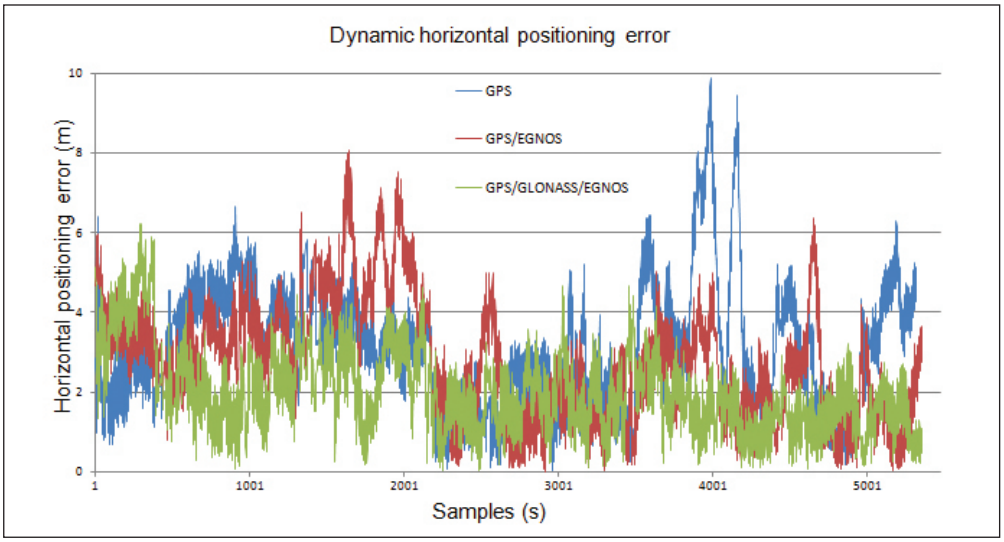

Figure 13 Absolute HPE time series during dynamic measurement period

Statistical parameters of dynamic measurements' results are presented numerically and graphically in Table 4 and on Figure 14, respectively.

Table 4 Dynamic measurements statistical description

RCV	Type	Min	Max	R	AVE	50%	68%	95%	VAR	MED	RMSE	SD
Garmin 76 CSx	G	0.20	9.88	9.68	3.13	3.04	3.79	5.70	2.46	3.03	3.51	1.57
Garmin 76 CSx	G/E	0.15	8.08	7.93	2.79	2.70	3.43	5.51	2.25	2.69	3.17	1.50
Garmin eTrex10	G/ GL/E	0.05	6.24	6.19	2.03	1.88	2.37	4.00	1.08	1.88	2.28	1.04

RCV – Receiver; G – GPS; GL – GLONASS; E – EGNOS; R – Range; MED – Median; SD – Standard deviation

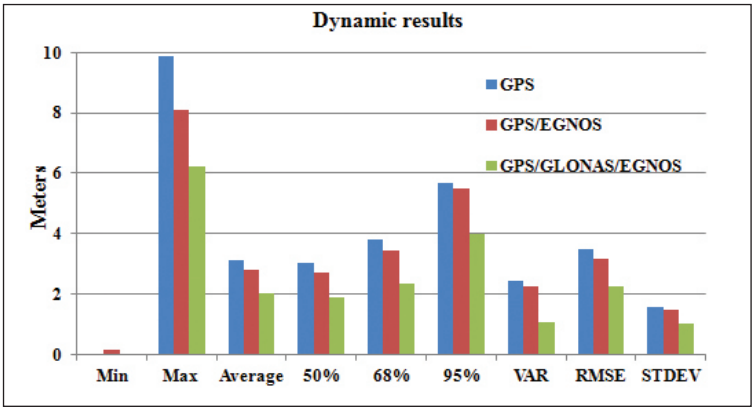

Figure 14 Graphical presentation of statistical parameters

The minimal positioning error varied from 0.08 m (GPS/GLONASS/EGNOS) to 0.2 m (GPS). Maximal error varied from 6.24 m (GPS/GLONASS/EGNOS) to 9.88 m (GPS). Average positioning error varied from 2.03 m (GPS/GLONASS/EGNOS) to 3.13 m (GPS). Variance was in the range from 1.08 m (GPS/GLONASS/EGNOS) to 2.46 m (GPS). RMSE values varied from 2.28 m (GPS/GLONASS/EGNOS) to 3.51 m (GPS). Average error scattering (SD) varied from 1.04 m (GPS/GLONASS/EGNOS) to 1.57 m (GPS). The range of observed error values shows that the positioning error in GPS receiver varied almost 10 meters, while it amounted 6 meters in GPS/GLONASS/EGNOS receiver, which is not negligible.

Garmin GPSmap 76CSx receiver has shown better dynamic horizontal positional accuracy using GPS augmented by EGNOS, when compared to standalone GPS. On Figure 15, distribution of dynamic data is shown comparing all three devices.

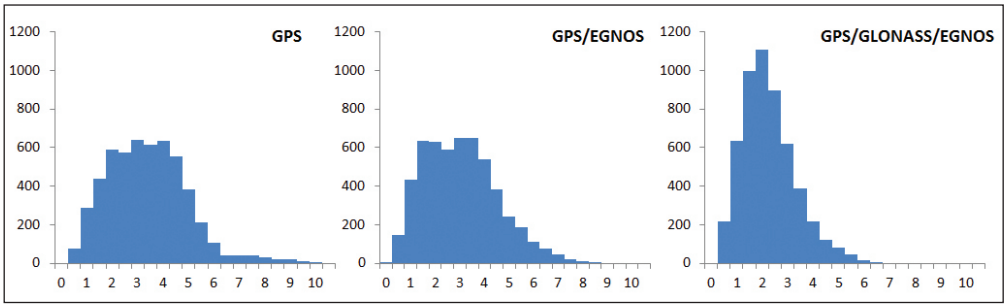

Figure 15 Histograms of used devices' positioning performance through dynamic measurements

Garmin eTrex10 receiver has shown better dynamic horizontal positional accuracy using (GPS/GLONAS/EGNOS) in comparison with Garmin GPSmap 76CSx (GPS). Statistical analyses have shown horizontal accuracy increase in all statistic tests by comparing Garmin eTrex10 (GPS/GLONASS/EGNOS) with Garmin GPSmap 76CSx (GPS/EGNOS).

4 DISCUSSION

In general terms, the outcome of conducted measurements was as expected. Augmented receivers showed more precise satellite positioning performance when compared with standalone single-constellation device, which reflects on all statistical elements employed in analysis.

There were significant differences in obtained position patterns in both cases of measurements, as well as in positioning performance between static and dynamic segment. All three devices have shown better static performance in eight out of nine statistical tests. The maximum error, 50%, 68, 95% percentile and root mean square error have shown two times higher dispersion in dynamic measurement in comparison with the static segment. Statistical test minimal error was remained the same for both measurements. Variance and standard deviation have shown lesser scattering in static measurement. Here, lesser scattering was noticed in GPS/EGNOS device than in combined SBAS augmented receiver. Garmin GPSmap 76CSx has shown better positioning performance augmented with EGNOS in both static and dynamic measurement. New generation handheld GNSS receiver Garmin eTrex10 has shown improvement in positioning precision using two constellation and EGNOS augmented service. Improvements in positioning performance are especially shown during the navigation segment of the research, as presented on Figure 16.

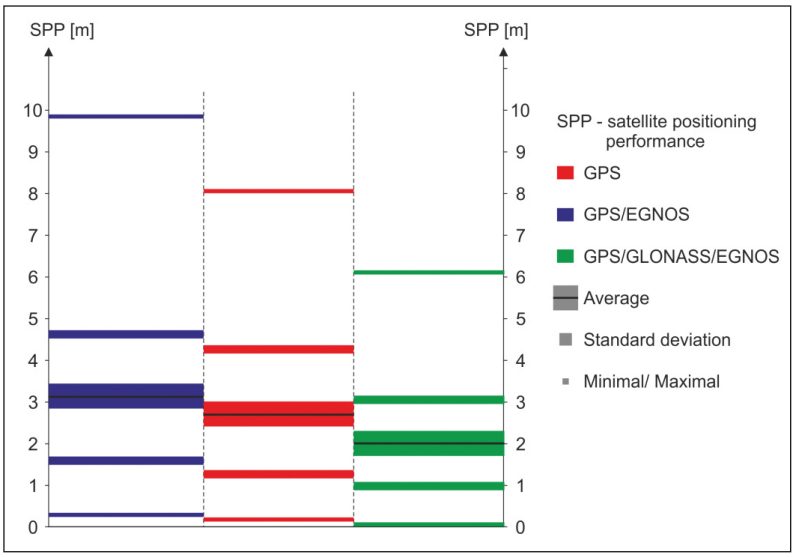

Figure 16 Dynamic satellite positioning performance

The measurements were conducted in a way that all external influential elements were mitigated to the extent possible. This was achieved by choosing favourable measurements' sites and convenient periods where solar and atmospheric activity was at their lowest. On Figure 17, the path of dynamic measurement is shown, as recorded with reference receiver.

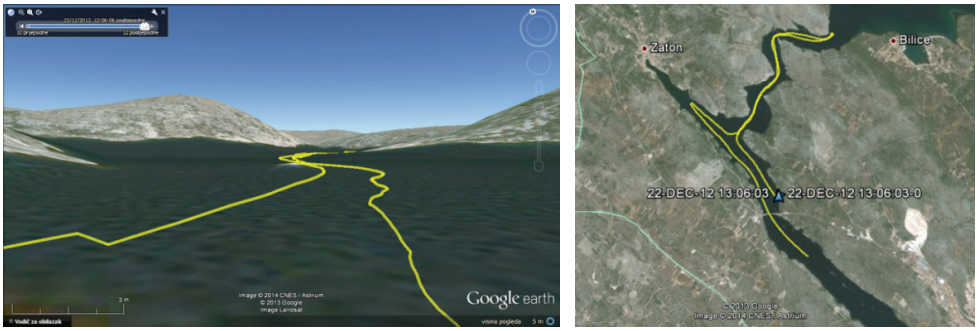

Figure 17 Dynamic measurement path

On Figure 18, a segment of recorded path from all used devices is presented. The following statement can be derived from the figure, but also from numerical statistical results. In general, there are no short-term deviations present; rather all

tracks are following the reference path with greater or lesser offset. However, the offset is constant through the recorded period.

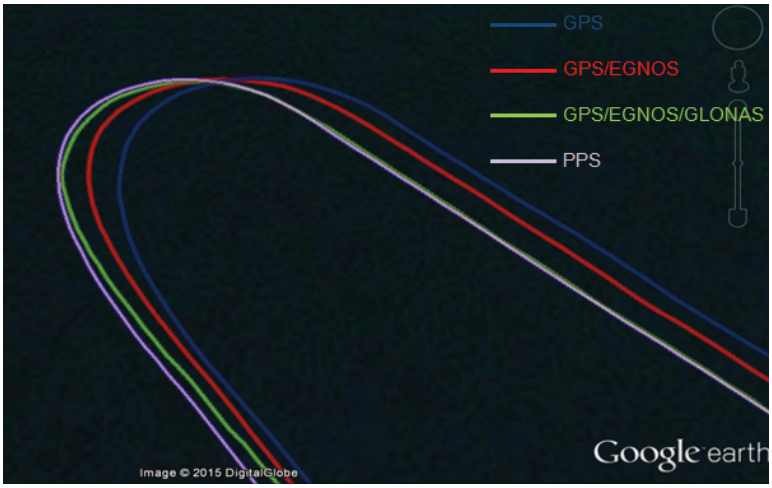

Figure 18 Segment of dynamic measurement positioning patterns: GNSS Leica RX 1220 (Precise Positioning service, purple), Garmin GPSmap 76CSx (GPS, blue), GPSmap 76CSx (GPS/EGNOS, red) and Garmin eTrex 10 (GPS/GLONASS/EGNOS, green)

Finally, the research shows that handheld GNSS receivers' HPE in both tests were significantly reduced using satellite-based augmentation. Improvement in horizontal positioning is even higher using combined GPS and GLONASS satellite navigation systems augmented by EGNOS system.

5 CONCLUSIONS AND PLANNED ACTIVITIES

In the proposed study, satellite positioning performance of three types of handheld devices was elaborated; standalone GPS receiver, combined GPS/GLONASS receiver and EGNOS-augmented combined receiver. Measurements were firstly conducted at a fixed point, after which sea navigation was conducted. Both sites were located in the littoral region of the Adriatic Sea. As a reference positioning source, dual-frequency GNSS receiver with differential augmentation was used, providing accuracy in order of millimetres (static segment) and centimetres (dynamic/navigation segment), respectively.

Analyses of measured data have shown significant improvements of the new-generation multi-constellation receivers, as expected. Differences in recorded

paths were also detected in terms of constant offsets rather than short-terms deviations, always using reference data for comparison.

The research was conducted paying particular attention on possible external influences on satellite positioning performance. All relevant factors which could affect satellite positioning were investigated, the experiment was planned, and the measurements took place in predicted time. This, environmental-preparation methodology represents a framework in monitoring of positioning performance solely, without or with mitigated outer impacts.

Satellite positioning performance presented in the paper is based on single measurement period, divided in static and dynamic segment. The periods of recording were relatively representative, however longer patterns/samples are needed in order to further confirm conclusions derived from the research. For instance, the position scattering during the static segment was more pronounced in EGNOS augmented receiver than in combined receiver only, where one would expect the opposite. Further studies are required in order to detect and positioning performance and possible error patterns' regularities when monitoring the performance with mitigated external influences. By employing several constellations instead of single one, the positioning error height component can be analysed thoroughly. Height error research is enabled given that satellites of each constellation are orbiting at slightly different heights, therefore vertical dilution of precision by using multi-constellation receivers can be significantly reduced.

Further activities imply employment and satellite positioning performance elaboration of developing SNSs not used in previous studies, primarily BeiDou and Galileo systems. Although with partial operation and limited coverage (BeiDou), the signals in space are already present in the Adriatic region.

Acknowledgments

Research activities presented in the paper were conducted under the research project *Research into the Correlation of Maritime-transport Elements in Marine Traffic: Satellite Navigation Segment*, supported by the University of Rijeka, Croatia.

REFERENCES

[1] EGNOS (2015). EGNOS User Support. Available at: http://bit.ly/1O0Ut1n [01.02.2014].

[2] GPSBabel. (2012). Free software for GPS data conversion and transfer. Available at: http://www.gpsbabel.org/ [21.10.2012]

[3] Kaplan, E.D. & Hegarty, C.J. (eds.) (2006). Understanding GPS: Principles and Application. Second edition. Boston: Artech House.

[4] Kos, S, Brčić, D. & Musulin, I. (2013). Smartphone application GPS performance during various space weather conditions: a preliminary study. Proc. 21st International Symposium on Electronics in Transport (ISEP). Ljubljana, Slovenia, March 25–26, 2013.

[5] Musulin, I. Kos, S, & Brčić, D. (2014). A study of smartphone satellite positioning performance at sea using GPS and GLONASS systems. Proc. 24st International Symposium on Electronics in Transport (ISEP). Ljubljana, Slovenia, March 24–25, 2014.

[6] National Geodetic Administration (2015). CROPOS: Croatian Positioning System. Available at: http://www.cropos.hr/ [01.03.2012]

[7] National Marine Electonics Association (NMEA) (2013). Available at: http://www.nmea.org/ [01.04.2013]

[8] National Oceanographic and Atmospheric Organisation (2013). Space Weather Prediction Center. Available at: http://1.usa.gov/1qjc38J [01.04.2013]

[9] Parkinson, B.W. & Spilker Jr., J.J. (eds.) (1996). Global Positioning System: Theory and Applications. Volume I. Washington, DC: AIAA.

[10] RISDE. Russian Institute of Space Device Engineering. (2008). GLONASS Interface Control Document (ICD): Navigation Radiosignal in L1, L2. Moscow: RISDE.

[11] The European GNSS Agency (GSA). (2015). EGNOS Open Service (OS): Service Definition Document. Prague: GSA

[12] Trimble Mission Planning Software (TMPS) (2010). Planning software Trimble social advice. Available at: http://bit.ly/1cKv7DN [31.10.2013.]

[13] USA Department of Defense (US DOD). (2008). Global Positioning System standard positioning service performance standard. Washington, DC: US DOD.

[14] Zandbergen, P.A. & Barbeau, S. J. (2011). Positional Accuracy of Assisted GPS Data from High-Sensitivity GPS-enabled Mobile Phones. The Journal of Navigation, 64(3), pp. 381–399.

Faculty of Maritime Studies
University of Rijeka, Croatia
University of Zagreb
Faculty of Transport
and Traffic Sciences
Royal Institute of Navigation
Science Technology Practice
9th
Annual
Baška GNSS
Conference

POSSIBILITY OF SBAS USAGE IN SUB-SAHARAN AFRICAN REGIONS

H.R. Ngaya[1], O.E. Abe[1,2], C. Paparini[1], X. Otero Villamide[1], S.M. Radicella[1], B. Nava[1]

[1] The Abdus Salam International Centre for Theoretical Physics (ICTP), Trieste, Italy
E-mail: ngahero@ictp.it/NGAYAHer@asecna.org

[2] Department of Physics, Federal University Oye – Ekiti, Nigeria

ABSTRACT. *Satellite Based Augmentation Systems (SBAS) aim to provide safe and reliable use of Global Navigation Satellite Systems (GNSS) in a wide range of applications like aviation, maritime, railway, survey, precision agriculture, road tracking. These systems have to fulfil specific requirements in the designed area of service. At low-latitude regions the ability to use a SBAS system is limited by the particularities of the ionosphere described by the presence large temporal and spatial gradients due to the Equatorial Ionosphere Anomaly (EIA) and the night-time ionospheric irregularities that can originate strong scintillations at user level. The ionosphere at these regions becomes a significant error source at range level when using signals transmitted by GNSS satellites. In addition the level of amplitude and phase fluctuations (scintillation) in those regions can affect the tracking of signals by the users. This paper presents indicative results of a potential SBAS in the Sub-Saharan African region; an area with the penchant on the ionosphere peculiarities.*

The first part of the study is devoted to the evaluation of the SBAS performance obtained using GNSS data from different open access network available in the low-latitude region and its comparison with respect to mid-latitudes. The second part is dedicated to the ionosphere effects on the SBAS performance. The Rate of Change of TEC Index (ROTI) was estimated to examine the irregularities in the region.

The study shows that a potential SBAS system can provide satisfactory level of service for different applications that can have a direct impact on the development of Sub-Saharan Africa. In addition it is revealed that the system performances are well correlated to the variability of the ionosphere irregularities as indicated by ROTI. It is expected that the present study serves as a baseline on future studies on SBAS in the region.

KEY WORDS: *SBAS, Sub-Saharan Africa, ROTI, TEC*

1 INTRODUCTION

The SBAS (Satellite Based Augmentation System) aims to augment the service obtained with standalone GNSS (Global Navigation Satellite System) by providing corrections to user inside a defined service area (Ventura et al, 2006). The current systems in service are: WAAS (Wide Area Augmentation System) for United States and Canada; EGNOS (European GNSS Overlay System) over ECAC (European Civil Aviation Conference) area and neighbouring countries, Multi-functional Satellite Augmentation System (MSAS) in Japan, System of Differential Correction and Monitoring (SDCM) in Russia, and GPS Aided Geo Augmented Navigation system (GAGAN) in India.

This technology is recognised as having a key role to play in maximising safety in the transport of passengers and goods (Roturier et al, 2006). In order to tackle the operational requirement of PBN (Performance-Based Navigation), ICAO (International Civil Aviation Organization) recommends the implementation of SBAS as primary mean of navigation by 2016 in replacement of the actual ground based NAVAIDS (ICAO, 2012).

However, to fulfil those requirements, the system has to overcome the limitations introduced by the environment in which the GNSS signal pass through. The most important limitation comes from the ionosphere because GNSS signal passing through this medium experiences delay and scintillations which complicate the computation of the navigation solution by the receiver. Several studies are on-going to improve the capability of SBAS to face these challenges (Pintor et al, 2014).

The area of interest of the research reported here is the Sub Saharan African region. Lying below the Equatorial Ionosphere Anomaly (EIA), the use of a possible SBAS system will have to deal with the peculiar physics of the area (Chatterjee et al, 2014). Therefore, it is important to study how the ionosphere behaviour impacts on the system. The specific aim of this work is to estimate the performances that a SBAS, as mean of navigation, can reach in the Sub-Saharan area using real data with a test-simulating SBAS platform.

2 TOOLS AND METHODOLOGY USED FOR THIS STUDY

Prior to any SBAS deployment in the area, it is relevant to evaluate the performances that the system can reach and to investigate on all problems relative to the environment that influence on these performances. Particular attention has to be given to geomagnetic conditions.

In order to do so, in absence of a dedicated GNSS network, a service area has been designed based on the available GNSS receivers in the region. The area of investigation comprised -2°N to / +16°N latitude and ±19°N longitude (Figure 1), and the data used in this study are from GNSS stations of different public networks in the area. The GNSS stations used for the study are: ouag (Ouagadougou, IGS), ykro (Abidjan, IGS), fg07 (Sao-Tome, IGS), nklg (Libreville, IGS), dakr (Dakar, IGS); bjco (Nigeria, NIGNET), cggn (Nigeria, NIGNET), bkfp (Nigeria, NIGNET), unec (Nigeria, NIGNET) and futy (Nigeria, NIGNET).

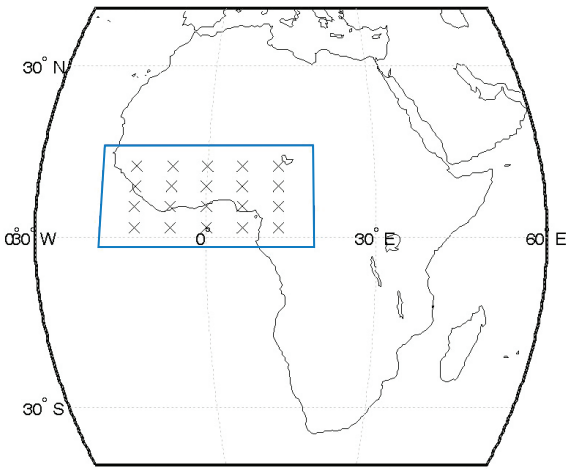

Figure 1 Service area (blue rectangle)

The data of these networks are of different formats because such networks are designed for a wide variety of purposes. Therefore the first task was to fit the data format with the input of the software which is 1Hz (requirement for the SBAS systems).

This study uses measurements of the year 2013. This year has been chosen because it contains large amount of data and also corresponds to the first peak of the solar cycle 24. The months of investigation chosen are January and July 2013 (representing solstice ionosphere); April and October 2013 (representing equinox ionosphere).

The analysis has been conducted using two main tools:

1. A SBAS emulator (MagicSBAS, GMV; Cezon et al, 2014) to produce SBAS messages.

2. Two performance analysis tools: ECLAYR for system performance analysis and MagicGEMINI for user performances analysis.

3 SYSTEM PERFORMANCE ANALYSIS

3.1 APV-I Performances Analysis

In this section, the results corresponding to the requirements of APV-I (Approach with vertical guidance category I) availability performances obtained making use of the simulation platform with real data in the region are presented. The basic concept of APV-I is to provide vertical guidance to an aircraft at a decision height higher than the 200 ft.; decision height traditionally used for Category I precision approaches. By definition, APV-I requirements are related to two concepts often used in this work: HPL (Horizontal Protection Level) and VPL (Vertical Protection Level). HPL can be defined as the radius of a circle in the horizontal plane, with its centre being at the true position, which describes the region assured to contain the indicated horizontal position. While VPL is the half length of a segment on the vertical axis with its centre being at the true position, which describes the region assured to contain the indicated vertical position For APV-I the requirements correspond to HPL below 40m and VPL below 50 m.

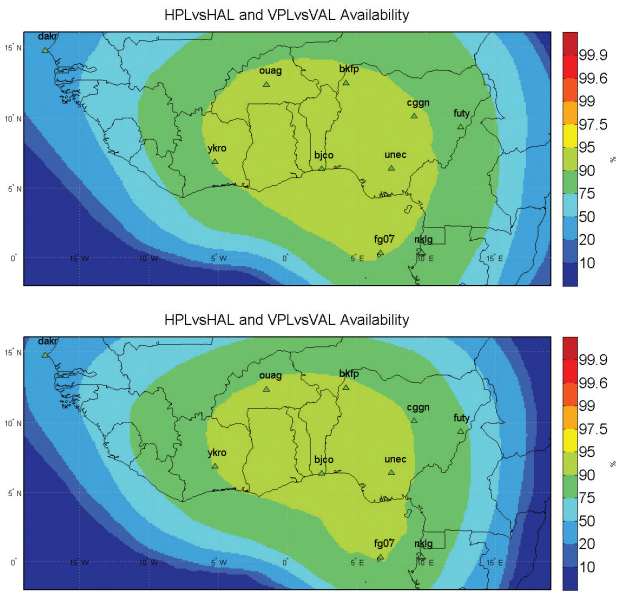

Figure 2 APV-I Availability on April 2013 24h (above), and October 2013 24h (below)

In the Figure 2 (above), the analysis has been made for the month of April 2013. The area is well covered by the stations in terms of density and distribution, the performance is between 90 - 95%, and in more than 60% of the service area the performances are above 75% (light and dark green respectively) during 24 hours.

Similar behaviour is noticed during the month of October with the same level of performance reached (Figure 2 below). As said previously, the two months representing the equinox ionosphere, which means a general increment in gradients and irregularities and therefore some degradation in the performance (see next section).

The Figure 3 (above and below) correspond to the computed performances for January and July 2013. The monthly performance reach 90% (light green) in a great portion of the area and in some part (in red) the performance is above 99%. The performances of these two months are greater than those of April and October.

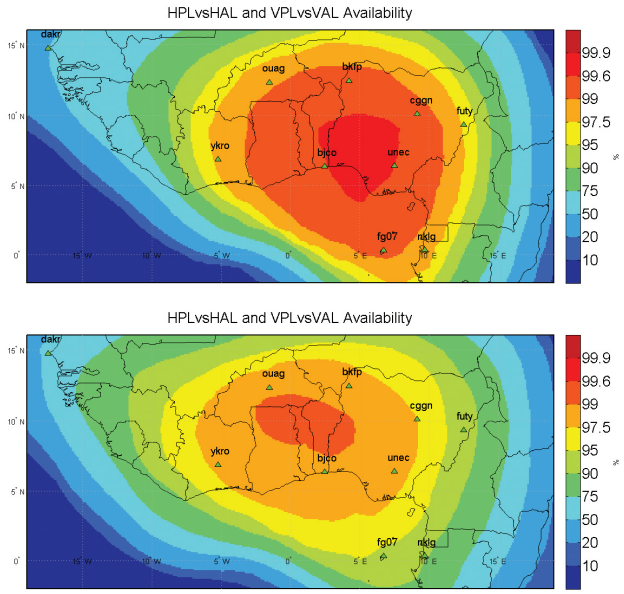

Figure 3 APV-I availability on January 2013 24h (above), and July 2013 24h (below)

The two periods, representing the equinox and solstice ionosphere give different results in term of APV-I performances, and this fact clearly shows that the SBAS performance is seasonal dependent. The difference in terms of performance for the months of the same period is small as it is shown by the two set of Figures 2 and 3.

By focusing the analysis of April and October on the period of the day between 04h and 18h, the results obtained are shown in the Figure 4.

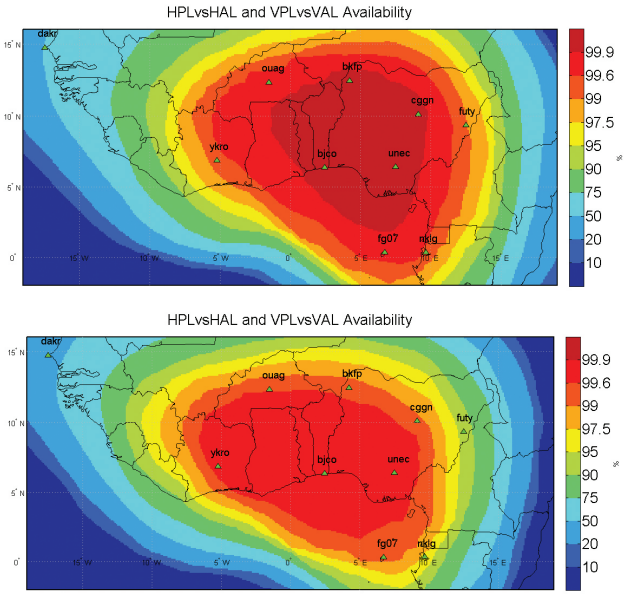

Figure 4 APV-I availability on April 2013 14h (above) October 2013 14h (below)

In the centre of the service area where the density of stations is larger the SBAS performances reaches 99.9% (Figure 4, above and below).

3.2 Analysis of Monitored PRN

Figure 5 presents the average number of monitored satellites by the system along the day during the periods of study.

To be monitored at a given epoch, a satellite has to be seen by at least 3 Ranging Integrity Monitoring Stations (RIMS). Taking into account that to compute position, the receiver needs to have at least 4 satellites in view; the higher is the number of monitored satellite, the higher is the probability to obtain a better performance.

It can be seen that the number of monitored satellites is lower before sunrise and after sunset, in comparison to daytime when the number of satellites is above 9.

During the months of October and April the number of monitored satellites after sunset decreases drastically even below 4 in some period which can lead either to degraded performances of the system or to have no solution.

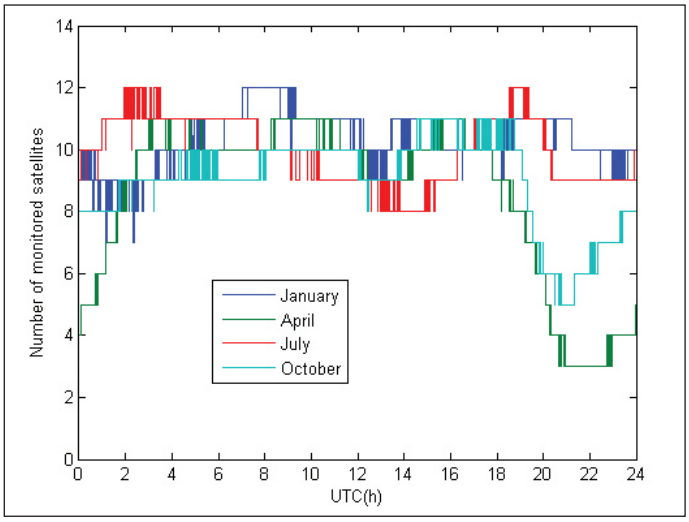

Figure 5 Monitored satellites on different months

3.3 Analysis Of Monitored IGPs

The figure below (Figure 6) shows that, during 24 hours, the number of monitored IGPs (Ionosphere Grid Points) increases from 00h to 04h and remains high during daytime. During April and October the number of IGPs decreases after sunset (Similar behaviour than the one shown in the number of monitored satellites). During January and July the number of monitored IGPs remains high from 04h to 24h.

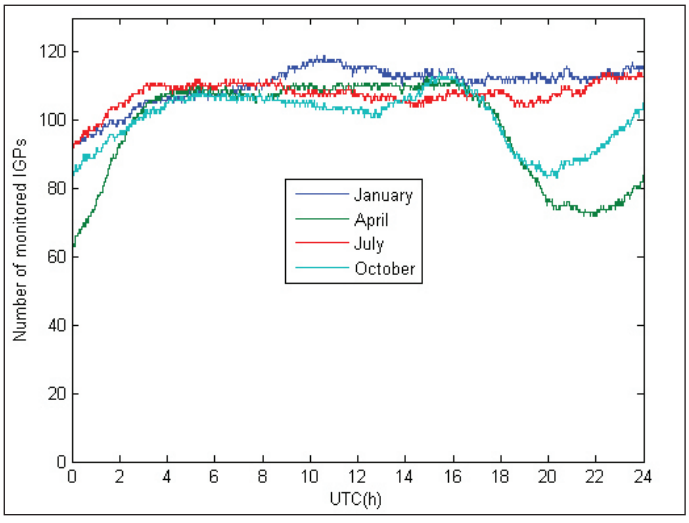

Figure 6 Number of IGPs versus time

3.4 Analysis Of ROTI

ROTI, Rate Of Change of TEC (ROT) Index, has been chosen to understand the ionosphere effects on the SBAS performances over the two selected periods. It can be defined as the standard deviation of ROT and it is used to identify small scale irregularities in the ionosphere. Furthermore ROTI is a well-known index used to predict the presence of scintillation and time gradient in the ionosphere (Pi et al, 1997).

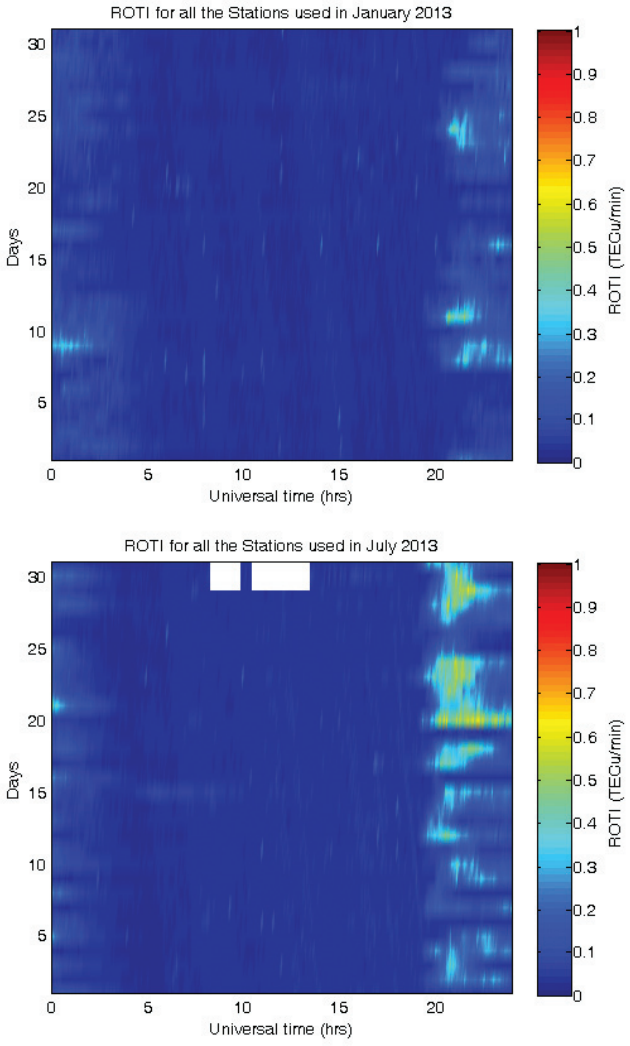

Figure 7 ROTI from January (above) and July (below)

Figure 7 shows the averaged ROTI over all the stations for the period of January (above) and July (below). Figure 8 shows the averaged ROTI over all the stations for the period of April (above) and October (below). ROTI is represented on a 2-D graph with the days of the month in the vertical axis and the hours of the days in the horizontal axis.

It is noticed that during the solstice months of January and July, the ROTI does not experience high values; being in average below 0.4 TECu/min.

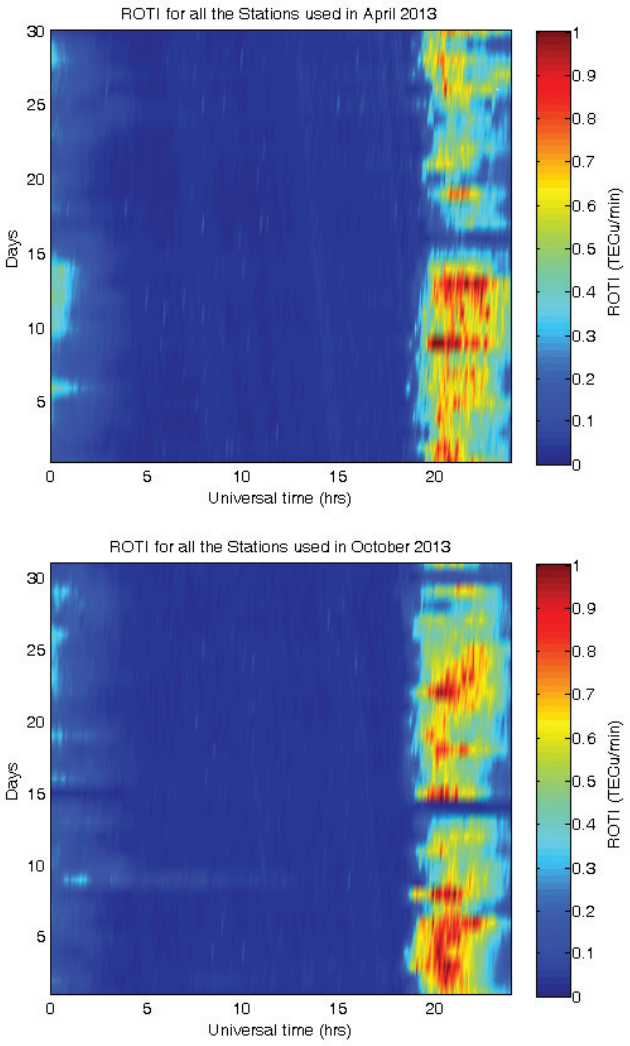

Figure 8 ROTI from April (above) and October (below)

During April and October, it is shown that ROTI values increase after sunset. The averaged value after 18h is above 0.7 TECu/min.

It is clear also that in some particular days of October (October 14th and October 30th) and April (April 16th), ROTI is also very low after sunset. This particular phenomenon is referred as inhibition of irregularities and can be linked to the occurrence of geomagnetic storms and their time development at the stations (Aarons, 1991).

3.5 Discussion

The analysis of ROTI shows that the SBAS performances are better when there are low irregularities in the ionosphere. The solstice months present less irregularities and the corresponding performances are increased, while during the equinoctial months the performances are degraded (particularly in the period with high level of irregularities). In a 24 hours basis performances are lower than during the day (See Figure 4, APV-1 is above 99% in a large part of the area, compliant with ICAO APV-I requirement for the usage in civil aviation for navigation).

This aspect is shown also by ROTI. During the day, the ROTI values are low so the performance is not degraded by ionosphere irregularities.

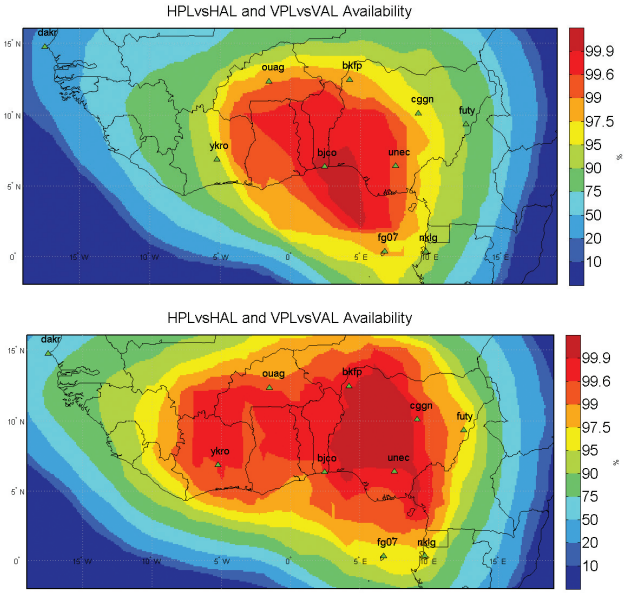

Figure 9 24h APV-I average October 14th, 2013 (above) 24h APV-I availability October 30th, 2013 (below)

Thanks to ROTI analysis, it is also noticed that during some particular days, when there are not irregularities in the ionosphere in contrary of what is usually expected (high time gradient after sunset during equinoxes months), the performance of the system is not degraded after sunset (See Figure 9).

This case illustrates that the performances of the system are linked to the ROTI behaviour.

4 USER PERFORMANCE ANALYSIS

4.1 Stanford Diagrams

A user located inside the service area, at Accra (Ghana), has been considered for the analysis of performances focusing on availability.

The Stanford diagram has been chosen to have a quick and simplified idea of the integrity and the performances of the system at user level. In this diagram, it is plotted the error versus the protection level for each epoch.

Figures 10 and 11 depict the Stanford Diagrams at this position during two different days of October 2013 (October 9th, a day with high level of ionospheric irregularities after sunset and October 30th, a day with inhibition of irregularities as seen in the previous section). The figures on the above represent the results of 24h analysis whereas figures on the below represent the results of 14h interval (from 4:00 to 18:00).

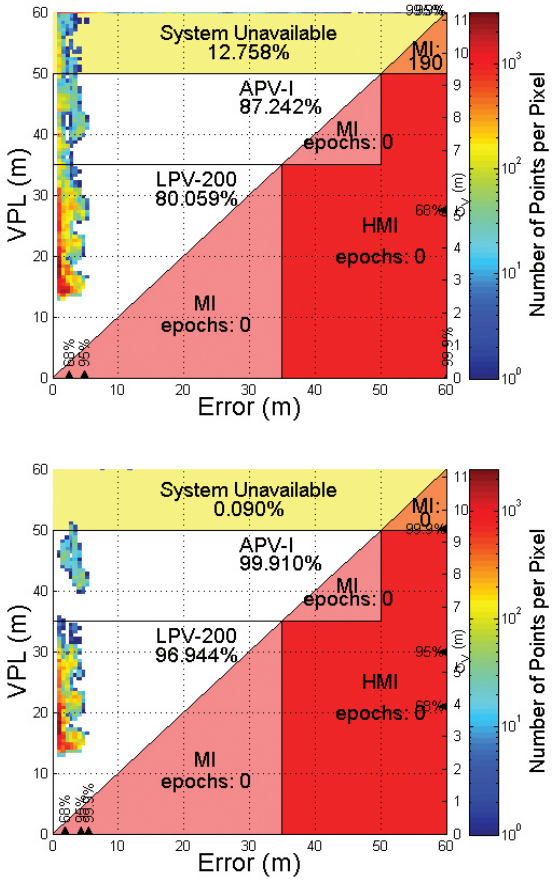

Figure 10 Stanford diagram of the user on October 9th 24h (above) and October 9th 14h (below)

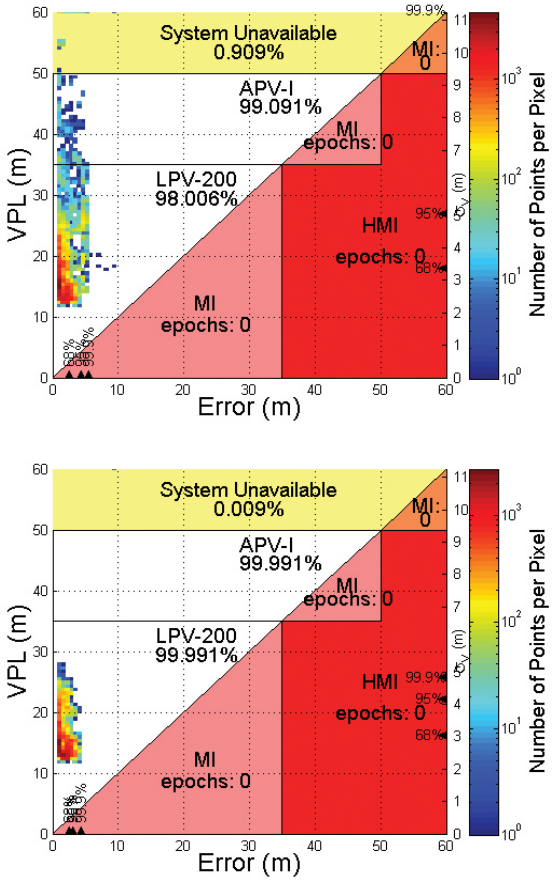

Figure 11 Stanford diagram of the user on October 30th 24h (above) and October 30th 14h (below)

During October 9th, the user reaches 87% of APV-I availability over 24 hours, while it reaches 99% in a 14 hours daily basis. In October 30th, APV-I availability is reachable over 24 hours due to the inhibition phenomena (same as Figure 9 below).

In all the cases the user does not experiences any hazardous event even though in some period the system is not available.

4.2 Positioning Error

The accuracy maps are presented in the Figures 12 and 13. These maps represent, for each user position, the 95 percentile of the Position Error. In EGNOS performance these maps are used to show the Open Service performance (defined as HPE<3m and VPE<4m).

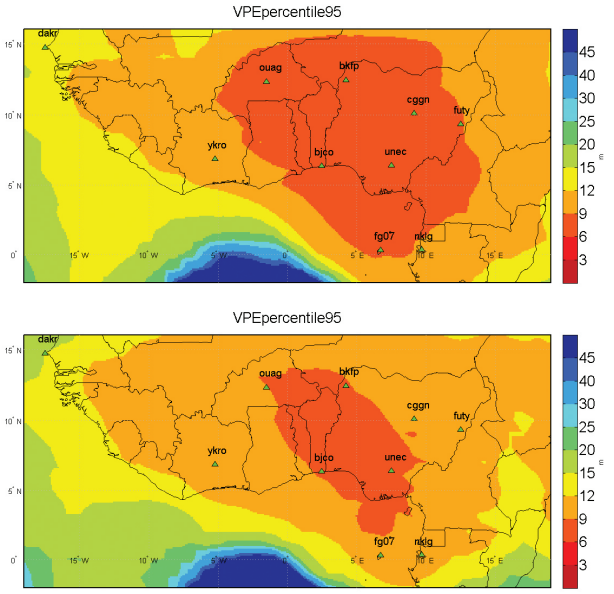

Figure 12 Accuracy maps of April (above) October 2013 (below)

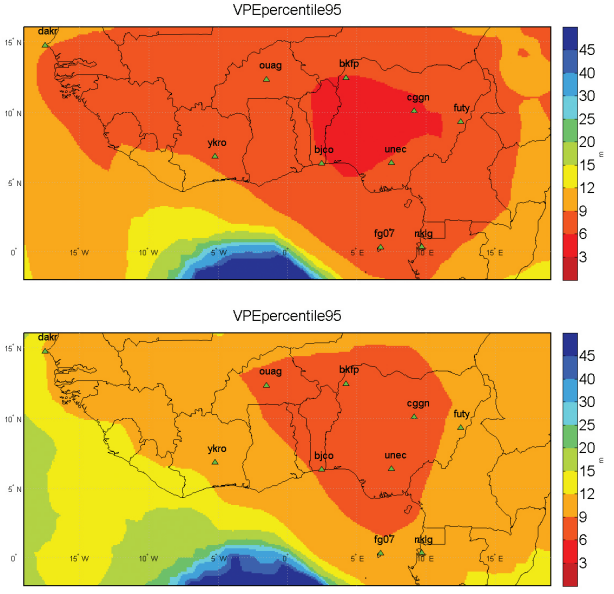

Figure 13 Accuracy maps of January (above) and July (below) 2013

In the cases of no stringent applications, the aim is to have just higher accuracy than with standalone GPS solution. During equinox's months, it is possible to reach levels of 6 – 9m accuracy, while in solstice months, particularly in January, less than 6m can be obtained.

5 CONCLUSION

This study has indicated the possibility that the system could work to some level in Sub-Saharan area. The simulation has been made with GNSS real data collected by different receivers installed in the area. It has been shown that the system performances are strongly dependent on the ionosphere behaviour**.** The study also stresses that, in some particular conditions, the SBAS system can show different performance results respect to an expected one. These particular cases present an enhancement in performances which is due to an inhibition of ionosphere irregularities, especially present after sunset (14th and 30th of October 2013, and 16th of April). The SBAS performances for these particular days follow the trend of ROTI, which can be considered not only as a good proxy for the ionosphere irregularities but also as a representative index for SBAS system availability.

The year 2013 belongs to solar cycle 24 which is not so high with respect to the previous cycles; it is evident that the study can be consolidated with more data.

It is also clear that the area of interest can be extended to eastern part of the region if GNSS stations are available.

According to the obtained results, the use of SBAS for navigation in Sub-Saharan Africa is possible; however efforts remain to be put on algorithm improvement, GNSS data network densification and the understanding of the peculiar physics of the ionosphere in the region.

REFERENCES

[1] Aarons, J. (1991) The role of the ring current in the generation or inhibition of equatorial F layer irregularities during magnetic storms", Radio Science, Volume 26.

[2] Cezon A.,Cueto M., Ramirez E, Ostolaza J, Izquierdo V, Perez D., Sardon E. (2014), "SBAS performance analysis in equatorial regions", ION-GNSS.

[3] Chatterjee S, Chakraborty S.K, Veenadhari B., and. Banola S. (February 2014) A study on ionospheric scintillation near the EIA crest in relation to equatorial electrodynamics, published by journal of Geophysical Research: space physics.

[4] GMV, magicSBAS, http://www.gmv.com/en/space/magicSBAS/.

[5] International Civil Aviation Organization (ICAO), Authority of the Secretariat of APIRG (March 2012), Global Navigation System (GNSS) implementation strategy for the ICAO Africa-Indian Ocean (AFI) region.

[6] International Civil Aviation Organization (ICAO) Asia and Pacific Office (5–7 February 2014), Report of the fourth meeting of ionospheric studies task force (ISTF/4), New Delhi, India.

[7] Pintor, P., Roldan, D., Gomez, J., de la Casa, C., Fidalgo, R.M. (2014), The impact of the high ionospheric activity in the EGNOS performance 2013. European Navigation Conference (ENC-GNSS) 2014, April 14 – 17, Rotterdam.

[8] Roturier B,. Chatre E., Ventura-Traveset J. (2006), The SBAS integrity Concept standardised by ICAO: Application to EGNOS.

[9] Ventura-Traveset, J., Flament, D. (2006), SBAS standards: EGNOS – The European Geostationary Navigation Overlay System. European Space Agency, ESA SP1303.

[10] SBAS standards: EGNOS – The European Geostationary Navigation Overlay System (EGNOS) – A cornerstone of GALILEO, ESA SP1303.

[11] AFREF Network – GPS data: http://www.afrefdata.org/

[12] NIGNET Network – GPS data: www.nignet.net-NIGNET

[13] SONEL Network – GPS data: http://www.sonel.org/-GPS-.html?lang=en

[14] Pi, X., Mannucci, A. J., Lindqdwister, U. J., Ho, C. M. (1997), Monitoring of Global Ionospheric Irregularities using the worldwide GPS, Geophys, Res. Letters, 24, (18), 2283–2286. Dio/10.1029/97GL02273.

Faculty of Maritime Studies
University of Rijeka, Croatia

University of Zagreb
Faculty of Transport
and Traffic Sciences

Royal Institute of Navigation
Science Technology Practice

9th
Annual
Baška GNSS
Conference

OPTIMAL EKF FOR QUASI-TIGHTLY COUPLED GNSS/INS INTEGRATION

Giacomo Pojani, Marco Bartolucci, Matteo Conti, Giovanni E. Corazza

Department of Electrical, Electronic and Information Engineering,
University of Bologna, Bologna, Italy

E-mail: {giacomo.pojani2, marco.bartolucci4, giovanni.corazza}@unibo.it,
matteo.conti9@studio.unibo.it

ABSTRACT. *In this paper, we investigate a navigation technique based on a modified optimization method for the operation of an extended Kalman filter. The algorithm presented recursively adapts the noise covariance matrices that characterize the model at each iteration. This optimization technique is intended to be an add-on for classical localization processing, in order to fulfill demanding accuracy specifications even in the presence of large dynamics. More specifically, we target the development of a particular quasi-tightly coupled GNSS/INS integration, which enables an cost-effective positioning solution, regardless of the receiver internal architecture. In this respect, we also describe a novel realization of this coupling in the form of the model used for Kalman filtering.*

Our goal is to provide the precision gain that is required to address the critical constraints of modern automotive applications in real-time. We finally show that the development of such a navigation method could be appropriate for a real-world scenario by evaluating the algorithm performance in tracking a fast-moving vehicle. A set of numerical simulations compares the results achieved either with or without optimization, testing different common racetracks. This comparison exhibits that the position estimates RMSE can be reduced at least by a factor of about 4.

KEY WORDS: *GNSS/INS, tracking, quasi-tight coupling, Kalman filter, noise covariance optimization*

1 INTRODUCTION

As many emerging automotive applications (e.g. autonomous navigation, dynamic control, driving assistance, route guidance, etc.) rely on localization services, enhanced reliability of vehicles positioning is becoming a crucial constraint. However, requirements in terms of both accuracy and availability turn out to be challenging in typical vehicular scenarios. The position solution is indeed potentially subject to harsh electromagnetic environments (e.g. urban canyons), where ranging signals are hindered or disturbed, and to large dynamics, whenever high speeds occur. With an increasing number of sensors being made available in modern vehicles, large amounts of data can be used to aid in the localization process together with satellite systems. Because of their complementary features, Global Navigation Satellite Systems (GNSS) are often employed together with Inertial Navigation Systems (INS) in order to improve the localization reliability [1]. On the one hand, the satellite constellation provides unbiased and repeatable position estimates, which are however available at slow rates and with limited precision. On the other hand, inertial sensors (such as accelerometers, magnetometers, and gyros) continuously allow for position updates at high rates, but their inner drift grow progressively into potentially unbounded errors. With the aim of balancing out these drawbacks, the received GNSS information is exploited to periodically calibrate the more precise INS, thus preventing the overall accuracy from degrading with time. As a result, this fusion effectively increases the average performance of a navigation system over long periods as well as its robustness to temporary service blockage or outage.

In this study, we present a navigation technique that enables the tracking of vehicles moving at high speeds with limited complexity. In particular, we consider the development of a precise telemetry system for Formula SAE (Society of Automotive Engineers) prototypes as our exemplary application. For this purpose, we resort ot a particular *quasi-tight* GNSS/INS integration [2] that blends the final positioning estimate computed by the receiver and several raw measurements collected by an inertial platform in a closed-loop form. Unlike more complex *tight* and *ultra-tight* couplings [3], this method works with no modification of the GNSS engine, since it combines coordinates and sensing data in a single solution, as shown in Fig. 1. At the same time, a configuration of this kind can potentially achieve a higher accuracy than a simpler *loose* level of integration, which is instead characterized by a weighted average of two independent solutions.

In brief, the system we target is capable of performing well with moderate complexity in order to be within the reach of a low-cost implementation. At this

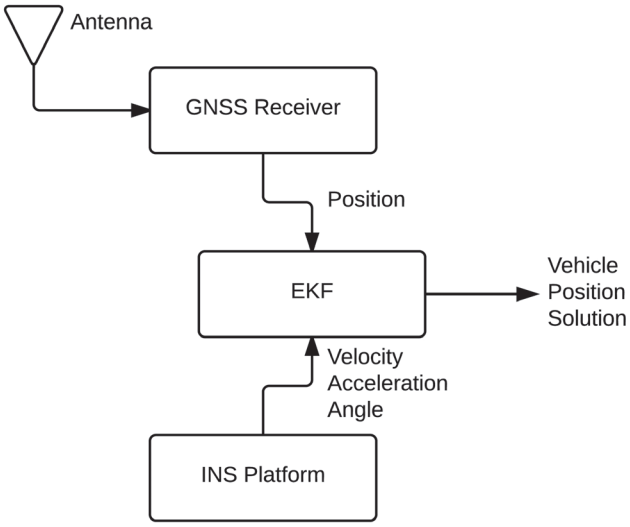

Figure 1 Quasi-tight GNSS/INS integration

regard, we carry out a specific quasi-tight coupling by adopting suitable deterministic description of the model that estimates the vehicle position in real-time. The mathematical formulation we propose represents a novel realization of this integration. An Extended Kalman Filter (EKF) is used to merge GNSS and INSS information, as velocities and accelerations of the tracked vehicle are described through time-variant relationships that are nonlinear [4], [5].

This paper addresses the optimization of the stochastic properties of the mathematical model underlying the estimation process. The noise covariance matrices are indeed tuning parameters of the Kalman filter and their identification increases the quality of the state estimation. Therefore, our goal is to achieve a quasi-optimal performance (i.e. approaching the Cramer-Rao bound) of the EKF, thus maximizing the accuracy of its final positioning estimate. For this task, we choose the Bayesian approach proposed in [6] by P. Matisko and V. Havlena, since it can provide more information about the entering noise parameters than other procedures reported in the literature (e.g. Autocovariance Least Squares [7]). This technique numerically approximates the probability distributions of noise matrices from output measurements along an important sampling method.

Even though the formulation of the principle underlying this approach results straightforward, its implementation was once impractical due to its demand for high computational power. Nowadays, the processing requirements of this Bayesian method can be handled even by entry-level devices. In [4], its

computation complexity and time consumption are compared to those given for Autocovariance Least Squares, highlighting the obtained advantages in terms of memory saving. Hence, a real-time execution of such a recursive algorithm is then expected to be already feasible into current GNSS/INS navigation systems like the proposed quasi-tight integration.

In this paper, we develop a modified version of this optimization algorithm, thus making possible to exploit this technique in the localization of fast-moving vehicles. This new capability represents an added value to the general method based on the Bayesian approach.

2 SYSTEM MODEL

The Kalman filter is a linear recursive Minimum Mean Square Error (MMSE) estimator of a hidden system state (i.e. not measurable) as a function of the previous estimate and of multiple sequential observations [4]. It relies on the quality characterizing the mathematical modeling of its deterministic linear dynamic system and of its stochastic inputs.

A. Model geometry

The deterministic model we use to describe the motion of the vehicle under test is based on the following assumptions. First of all, the dynamic physical quantities identifying the current state (i.e. position, velocity, and acceleration) are related to a so-called *main* two-dimensional reference system XY with the Y axis pointing to North of a geodetic system East-North-Up (ENU), as illustrated in Fig. 2. Hence, the vehicle is supposed to move on a flat surface, as the Z axis corresponding to the Up direction is not taken into account. Such an hypothesis proves to be realistic as we consider the scenario of a typical Formula SAE racetrack, which usually does not feature either significant altitude differences or large dimensions. The curvature of the earth in each point may be consequently neglected.

Further, the orientation of the motion with respect to the main axes is taken into account by defining a two-dimensional *body* reference system $X_{body}Y_{body}$, which is in-built with the vehicle and the inertial platform. This has a tangential Y_{body} axis along the trajectory and a perpendicular X_{body} axis outgoing from the right side. The instantaneous rotation angle between Y and Y_{body} is denoted by θ and its measure is available thanks to the magnetometer on board. Before starting the simulation, when the vehicle is still stationary, we assume to align the two reference systems through the initial value θ_0.

Without loss of generality, we also set the first position coordinates into the origin of the main reference system and we finally sketch the vehicle size as a point-like particle.

With the goal of testing the situations that may occur in classic FSAE racetracks, we design some basic types of motions for our particle-like vehicle:

1. straight lines with uniform acceleration;

2. quick turns at constant velocity;

3. circular hairpins at constant velocity;

4. slaloms at constant velocity.

These trajectories can be generated separately or rather be assembled together to arrange a whole circuit.

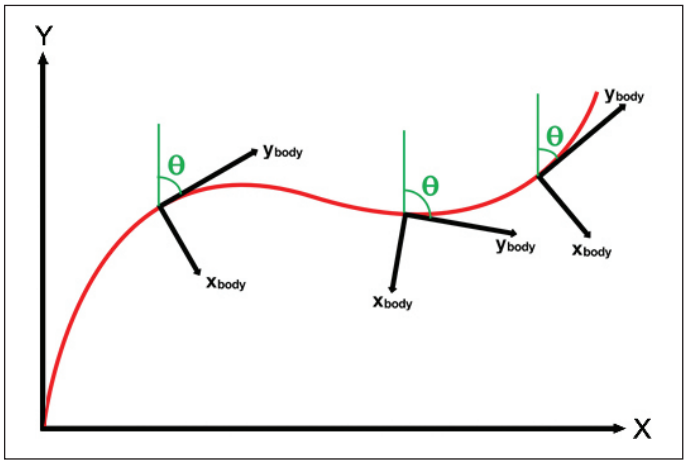

Figure 2 Main and body reference systems

B. Model dynamics

The vehicle dynamics are modeled according to the kinematic equations of a point-like particle motion over time. They are described through several time-varying interdependent variables: the coordinates (*X, Y*) and the ground speed fv_{GNSS} read from the GNSS receiver with respect to the main reference system and the velocity magnitude v_{INS} and the acceleration components ($a_{x_{body}}$, $a_{y_{body}}$) respectively measured by a gyroscope and an accelerometer in the body reference system.

The values computed through the kinematic equations describe ideal trajectories, whereas the data read from the GNSS/INS unit are realistically affected by inevitable errors. In order to statistically model the reality, a certain degree of imprecision is added in form of Gaussian random variables with zero mean and different standard deviations. We assume the errors to be mutually uncorrelated and to form white time-sequences, which is an effect of the GNSS correction on the slowly drifting inertial measurements. The value of positional dilution of precision actually depends on the GNSS technology and the visible satellites constellation.

C. Estimation state

Since the task of the Kalman filter is a position reckoning as accurate as possible, it suitably combines redundant sequential observations to average out the estimate errors. For this reason, in addition to the position coordinates of interest, the *actual* state vector **x** includes also four variables related to the axial velocities and accelerations, which aid the estimation process, since they contain useful positional information that are extracted through the deterministic model.

Hence, according to a discrete-time formulation, at each *k*-th iteration the state has six components that are all related to the main reference system *XY*:

$$\mathbf{x}_k = \begin{bmatrix} X_k \\ Y_k \\ v_{X_k} \\ v_{Y_k} \\ a_{X_k} \\ a_{Y_k} \end{bmatrix} \tag{1}$$

By denoting the *estimated* state vector as $\hat{\mathbf{x}}$, the relative error covariance matrix **P** is:

$$\mathbf{P}_k = E[(\mathbf{x}_k - \hat{\mathbf{x}}_k)(\mathbf{x}_k - \hat{\mathbf{x}}_k)^T] \tag{2}$$

where $E[.]$ is the expected value operator.

Due to the assumptions concerning the starting position, the initially estimated *a-priori* $\hat{\mathbf{x}}_{\bar{0}}$ and *a-posteriori* $\hat{\mathbf{x}}_0$ state vectors are defined by:

$$\hat{\mathbf{x}}_{\bar{0}} = \begin{bmatrix} 0 \\ 0 \\ 0 \\ 0 \\ 0 \\ 0 \end{bmatrix} \qquad \hat{\mathbf{x}}_0 = \begin{bmatrix} 0 \\ 0 \\ v_{X_0} \\ 0 \\ a_{x_{body_0}} \\ a_{y_{body_0}} \end{bmatrix} \tag{3}$$

This means we suppose that at first the vehicle lies in the *XY* origin, the measured velocity vector is along the *X* axis, and the accelerations correspond to those that are recorded along the x_{body} and y_{body} axes, which are initially aligned to the main ones.

As far as the error covariance matrix is concerned, the estimation error components are assumed statistically uncorrelated at first:

$$\mathbf{P}_0 = \rho \cdot \mathbf{I}_6 \tag{4}$$

where **I** denotes the unit matrix and $\rho \in \mathrm{R}^+$ is arbitrary small as we suppose to have precise initial estimations.

D. Deterministic model

In general, the so-called extended Kalman filter is an efficient method for nonlinear estimation that can be applied to a discrete-time nonlinear dynamic system [5], in the form:

$$\mathbf{x}_k = f_k(\mathbf{x}_{k-1}, \mathbf{u}_{k-1}, \mathbf{w}_{k-1}) \tag{5}$$

$$\mathbf{y}_k = h_k(\mathbf{x}_k, \mathbf{v}_k) \tag{6}$$

where **y** is the output observed vector collecting the measurements, ***f*** and ***h*** denote nonlinear differentiable functions, **u** is the input control vector, and vectors **w** and **v** represent the zero-mean noise affecting the state and the observation respectively.

At each step k, this filter essentially provides first-order approximations (Taylor series expansion) to the actual state $\mathbf{x}$ and observation $\mathbf{y}$ terms around their respective predicted mean values $\overline{\mathbf{x}}$ and $\overline{\mathbf{y}}$, according to:

$$\mathbf{x}_k \approx \overline{\mathbf{x}}_k + \mathbf{A}_k(\mathbf{x}_{k-1} - \hat{\mathbf{x}}_{k-1}) + \mathbf{w}_{k-1} \tag{7}$$

$$\mathbf{y}_k \approx \overline{\mathbf{y}}_k + \mathbf{H}_k(\mathbf{y}_k - \hat{\mathbf{y}}_k) + \mathbf{v}_k \tag{8}$$

where $\mathbf{A}$ and $\mathbf{H}$ are computed as Jacobian matrices of f and h, respectively, and so describe the local linear deviations from the mean values, which in turn are expressed by:

$$\begin{aligned} &\overline{\mathbf{x}}_k \approx E[f_k(\hat{\mathbf{x}}_{k-1}, \mathbf{u}_{k-1}, \mathbf{w}_k)] = \\ &f_k(\hat{\mathbf{x}}_{k-1}, \mathbf{u}_{k-1}, \mathbf{0}) = \hat{\mathbf{x}}_k^- \end{aligned} \tag{9}$$

$$\begin{aligned} &\overline{\mathbf{y}}_k \approx E[h_k(\overline{\mathbf{x}}_k, \mathbf{v}_k)] = \\ &h_k(\overline{\mathbf{x}}_k, \mathbf{0}) = h_k(\hat{\mathbf{x}}_k^-, \mathbf{0}) = \hat{\mathbf{y}}_k \end{aligned} \tag{10}$$

It can be noted that the EKF operation is based on a deterministic model that is fully described through $\mathbf{A}$ and $\mathbf{H}$, which are also known as transition model and observation model, respectively.

In our case of interest, we omit the forced response (conventionally indicated by matrix $\mathbf{B}$) as no control input is driving the system. Hence, the transition model comes out to be the free-evolution of the dynamic system.

In order to find the general expression of the matrix A_k predicting the current state $\mathbf{x}_k$ based on the previous estimate $\mathbf{x}_{k-1}$, let us consider a linear motion with uniform acceleration. The k-th a-priori estimated state then becomes:

$$\hat{\mathbf{x}}_k^- = f(\hat{\mathbf{x}}_{k-1}, \mathbf{0}, \mathbf{0}) = \mathbf{A}\hat{\mathbf{x}}_{k-1} = \begin{bmatrix} X_{k-1} + v_{X_{k-1}} dt + \frac{1}{2} a_{X_{k-1}} dt^2 \\ Y_{k-1} + v_{Y_{k-1}} dt + \frac{1}{2} a_{Y_{k-1}} dt^2 \\ v_{X_{k-1}} + a_{X_{k-1}} dt \\ v_{Y_{k-1}} + a_{Y_{k-1}} dt \\ a_{X_{k-1}} \\ a_{Y_{k-1}} \end{bmatrix} \tag{11}$$

Here *dt* represents the time between the two consecutive steps *k* and *k*–1. As long as this time interval results short enough, we assume this matrix $\mathbf{A} \in \mathbf{M}_{6\times6}(\mathbf{R})$ to be constant at each iteration. In other words, the transitional model can be considered as time-invariant as long as the kinematic equations (and so the function *f*) between two close instants are those of a linear motion with uniform acceleration. This aspect characterizes our description of the deterministic model used by the EKF.

We finally formulate the transition model as:

$$\mathbf{A}_{[i,j]} = \frac{\partial f_{[i]}}{\partial x_{[j]}}(\hat{\mathbf{x}}_{k-1}, \mathbf{0}, \mathbf{0}) = \begin{bmatrix} 1 & 0 & dt & 0 & \frac{dt^2}{2} & 0 \\ 0 & 1 & 0 & dt & 0 & \frac{dt^2}{2} \\ 0 & 0 & 1 & 0 & dt & 0 \\ 0 & 0 & 0 & 1 & 0 & dt \\ 0 & 0 & 0 & 0 & 1 & 0 \\ 0 & 0 & 0 & 0 & 0 & 1 \end{bmatrix} \quad \textbf{(12)}$$

Such a simple matrix is valid for all the possible motions and kinematic equations that might be taken in consideration for the vehicle.

As far as the observation model is concerned, the output measurements are predicted by the filter through the Eq. (10) and become:

$$\hat{\mathbf{y}}_k = \begin{bmatrix} X_k \\ Y_k \\ v_{GNSS_k} \\ v_{INS_k} \\ a_{X_k} \\ a_{Y_k} \end{bmatrix} = \begin{bmatrix} X_k \\ Y_k \\ \sqrt{v_{X_k}^2 + v_{Y_k}^2} \\ \sqrt{v_{X_k}^2 + v_{Y_k}^2} \\ a_{X_k} \\ a_{Y_k} \end{bmatrix} \quad \textbf{(13)}$$

where a_{x_k} and a_{x_k} are the accelerations measured by the accelerometers on board and rotated from the body reference system to the main one at each iteration as follows:

$$\begin{bmatrix} a_{X_k} \\ a_{X_k} \end{bmatrix} = \begin{bmatrix} \cos\theta_k & -\sin\theta_k \\ \sin\theta_k & \cos\theta_k \end{bmatrix} \begin{bmatrix} a_{x_{body_k}} \\ a_{y_{body_k}} \end{bmatrix} \tag{14}$$

Hence, the matrix $\mathbf{H} \in \mathbf{M}_{6\times6}(\mathbf{R})$ relating the current observed vector state $\hat{\mathbf{y}}_k$ to the correspondent state estimate $\hat{\mathbf{x}}_k$ is defined by:

$$\mathbf{H}_{k[i,j]} = \frac{\partial h_{[i]}}{\partial x_{[j]}}(\hat{\mathbf{x}}_{\bar{k}}, \mathbf{0}) = \begin{bmatrix} 1 & 0 & 0 & 0 & 0 & 0 \\ 0 & 1 & 0 & 0 & 0 & 0 \\ 0 & 0 & \frac{v_{X_k}^2}{\sqrt{v_{X_k}^2 + v_{Y_k}^2}} & \frac{v_{Y_k}^2}{\sqrt{v_{X_k}^2 + v_{Y_k}^2}} & 0 & 0 \\ 0 & 0 & \frac{v_{X_k}^2}{\sqrt{v_{X_k}^2 + v_{Y_k}^2}} & \frac{v_{Y_k}^2}{\sqrt{v_{X_k}^2 + v_{Y_k}^2}} & 0 & 0 \\ 0 & 0 & 0 & 0 & 1 & 0 \\ 0 & 0 & 0 & 0 & 0 & 1 \end{bmatrix} \tag{15}$$

However, unlike the transition model, the observation model cannot be the same for each iteration, but it should rather change over time. Indeed, the data received from satellites are not synchronized with that coming from the INS, as the inertial sensors reach higher update rates. In order to take into account this issue, we use the following alternative version of the matrix **H** for those time steps in which the GNSS information are not refreshed and become obsolete:

$$\mathbf{H}_{k[i,j]} = \frac{\partial h_{[i]}}{\partial x_{[j]}}(\hat{\mathbf{x}}_k^-, \mathbf{0}) = \begin{bmatrix} 0 & 0 & 0 & 0 & 0 & 0 \\ 0 & 0 & 0 & 0 & 0 & 0 \\ 0 & 0 & 0 & 0 & 0 & 0 \\ 0 & 0 & \frac{v_{X_k}^2}{\sqrt{v_{X_k}^2 + v_{Y_k}^2}} & \frac{v_{Y_k}^2}{\sqrt{v_{X_k}^2 + v_{Y_k}^2}} & 0 & 0 \\ 0 & 0 & 0 & 0 & 1 & 0 \\ 0 & 0 & 0 & 0 & 0 & 1 \end{bmatrix} \tag{16}$$

In other words, whenever the up-to-date GNSS position is available, it is then used to calibrate the intertial platform. Otherwise the sensing measurements would lead to wrong estimates after a while, due to their growing biases.

We finally point out that an observation model as such combines the solution (X, Y, v_{GNSS}) computed by the receiver together with rough mixed data provided by various sensors (v_{INS}, $a_{x_{body}}$, $a_{y_{body}}$, θ). Hence, a GNSS/INS integration built on the mathematical formulation proposed above represents a quasi-tight coupling by definition.

E. Stochastic model

The stochastic model represents the uncertainties that characterize the dynamic system. As usual in the reference literature, we consider both the state noise and the observation noise to be mutually independent to each other and to have multivariate Gaussian N distributions with zero mean:

$$p(\mathbf{w}_k) = N(\mathbf{0}; \mathbf{Q}_\mathbf{k}), \forall k \quad \textbf{(17)}$$

$$p(\mathbf{v}_k) = N(\mathbf{0}; \mathbf{R}_\mathbf{k}), \forall k \quad \textbf{(18)}$$

where $\mathbf{Q} \in \mathbf{M}_{6\times6}(\mathbf{R})$ and $\mathbf{R} \in \mathbf{M}_{6\times6}(\mathbf{R})$ denote the state and observation noise covariance matrices respectively. They reflect the degree of confidence that we put in the deterministic model expressed by Eq. (5) and (6).

While the matrix $\mathbf{Q}$ is intended to be recursively optimized by the proposed algorithm, the matrix $\mathbf{R}$ is instead assumed to be known at each time step. This latter results diagonal and its elements are the variances of the uncorrelated observation errors that are reported in Table 1. Coherently with the definition of $\mathbf{H}$ for the observation model, this noise covariance matrix has two alternative formulations. The first definition is valid whenever the GNSS information are up-to-date:

$$\mathbf{R_k} = \begin{bmatrix} \sigma^2_X & 0 & 0 & 0 & 0 & 0 \\ 0 & \sigma^2_Y & 0 & 0 & 0 & 0 \\ 0 & 0 & \sigma^2_{v_{GNSS}} & 0 & 0 & 0 \\ 0 & 0 & 0 & \sigma^2_{v_{INS}} & 0 & 0 \\ 0 & 0 & 0 & 0 & \sigma^2_{a_{x_{body}}} & 0 \\ 0 & 0 & 0 & 0 & 0 & \sigma^2_{a_{y_{body}}} \end{bmatrix} \quad \textbf{(19)}$$

On the contrary, the following expression is built so that the Kalman filter relies more on the other measurements coming from the inertial sensors:

$$\mathbf{R_k} = \begin{bmatrix} \Sigma & 0 & 0 & 0 & 0 & 0 \\ 0 & \Sigma & 0 & 0 & 0 & 0 \\ 0 & 0 & \Sigma & 0 & 0 & 0 \\ 0 & 0 & 0 & \sigma^2_{v_{INS}} & 0 & 0 \\ 0 & 0 & 0 & 0 & \sigma^2_{a_{x_{body}}} & 0 \\ 0 & 0 & 0 & 0 & 0 & \sigma^2_{a_{y_{body}}} \end{bmatrix} \quad \textbf{(20)}$$

where $\Sigma \in \mathrm{R}^+$ indicates an arbitrary large value.

F. Optimal estimation

If the model is ideally identified in both its deterministic and stochastic properties, the Kalman filter performance is *optimal*: it minimizes the covariance of the state estimation error. When this happens, it may be verified that the output prediction errors form a white innovation sequence. Unfortunately, this cannot be achieved in practice.

Once a suitable deterministic model is found, then the estimation quality depends directly on the knowledge of the covariances of the state and observation noise. This implies the matrices **Q** and **R** become tuning parameters for the filter.

It can be proved that the linear approximations of the EKF could lead to a sub-optimal performance and even divergence of the estimation process [5]. In order to address this issue, the noise covariance matrices must be tuned so that the measurements residuals feature the desired statistical distribution, which should be white and Gaussian in accordance with the entering noise vectors **w** and **v** [8]. This result can be achieved by means of the optimization algorithm discussed in next section.

3 OPTIMIZATION ALGORITHM

In this paper, we try to ensure that the extended Kalman filter performance is close to the optimum by getting an insight into the optimal noise covariance matrices. For this purpose, we recursively compute at every iteration the matrices **Q** and **R** that maximize the probability of observing the current and past output measurements. The advantage of a recursive algorithm is that it performs an *adaptive* filtering, which is necessary if the true noise covariance matrices are time-varying.

A. Bayesian method

In brief, this technique returns the noise covariance matrices that are characterized by the maximal probability density function (pdf) [6].

Let us define a *likelihood function* as the probability distribution of the actual output observed vector $\mathbf{y}_k$ conditioned by the previous measured data $\mathbf{Y}^{k-1}$ and by the current matrices $\mathbf{Q}_k$ and $\mathbf{R}_k$. Since the entering noise is assumed white and Gaussian as usual, this function results a multivariate Gaussian N distribution with the mean vector $\overline{\mathbf{y}}_k$ and the covariance matrix $\mathbf{P}_{\mathbf{k}}^{\mathbf{y}}$ that are predicted for the current output $\mathbf{y}_k$:

$$\mathbf{Y}^k = \{\mathbf{y}_0, \mathbf{y}_1, ..., \mathbf{y}_k\} \tag{21}$$

$$p(\mathbf{y}_k \mid \mathbf{Y}^{k-1}, \mathbf{Q}_\mathbf{k}, \mathbf{R}_\mathbf{k}) = N(\overline{\mathbf{y}}_k; \mathbf{P}_\mathbf{k}^\mathbf{y}) = N(\hat{\mathbf{y}}_k; \mathbf{P}_\mathbf{k}^\mathbf{y}) \tag{22}$$

The posterior conditional pdf of $\mathbf{Q}_\mathbf{k}$ and $\mathbf{R}_\mathbf{k}$ conditioned on the observed data $\mathbf{Y}^k$ (up to the current k-th time step) is updated by recursively multiplying the likelihood function with the prior conditioned pdf, as follows:

$$p(\mathbf{Q_k}, \mathbf{R_k} \mid \mathbf{Y}^k) = \frac{p(\mathbf{y}_k \mid \mathbf{Y}^{k-1}, \mathbf{Q_k}, \mathbf{R_k})}{p(\mathbf{y}_k \mid \mathbf{Y}^{k-1})} \cdot p(\mathbf{Q_k}, \mathbf{R_k} \mid \mathbf{Y}^{k-1}) \quad \textbf{(23)}$$

In other words, the most probable pair of noise covariances matrices is found by numerically approximating the Bayes formula at every iteration. This approach is employed in a recursive algorithm that is in order of optimizing the statistical model.

B. Recursive algorithm

1) Parametrization: chosen a suitable parameters vector **Ù**, we define a set *S* of state noise covariance matrices according to the prior knowledge about the stochastic model. The initial parameters have usually a logarithmic scale to assure a higher density for smaller covariances. For the sake of simplicity, the matrix **Q** is parametrized as a multiplier of the unit matrix:

$$\mathbf{\Omega}_k = (\Omega_k^1, \Omega_k^2, ..., \Omega_k^N), N \in \mathsf{N} \quad \textbf{(24)}$$

$$S_k = S(\mathbf{\Omega}_k) = \{\mathbf{Q}(\Omega_k^i) = \Omega_k^i \cdot \mathbf{I}_6, \forall i\}, \Omega^i \in \mathsf{R}^+ \quad \textbf{(25)}$$

As far as the observation noise covariance is concerned, the matrix **R** is instead fixed according to Eq (19) and (20), because we assume to know the exact measurements statistics.

2) Parallel estimation with iterative optimization: given a grid of noise covariances matrices, the algorithm executes multiple EKFs at every iteration, one for each pair $\mathbf{Q}(\mathbf{\Omega}_k^i)$, $\mathbf{R}_k$), parallelizing the state estimation.

In the meanwhile, the conditional posterior probability distribution $p(\mathbf{Q}(\mathbf{\Omega}_k^i), \mathbf{R}_k | \mathbf{Y}^k)$ is also recursively computed using Eq. (23) for all the covariances covered by the grid at the current time step. After all the desired matrices have been processed, the optimal state noise covariance matrix to be used by the filter is selected according to the *Maximum A-posteriori Probability* (MAP) criterion:

$$\hat{\mathbf{Q}}_k = \underset{\Omega_k^i}{\operatorname{argmax}}\, p(\mathbf{Q}(\Omega_k^i), \mathbf{R_k} \mid \mathbf{Y}^k) \quad \textbf{(26)}$$

Before the next iteration, the algorithm generates new points for the set S_{k+1} from the last posterior pdf values by resorting to the importance sampling method, which belongs to the Monte Carlo family. Then, a prior pdf is assigned to these points and the whole estimation and optimization process is repeated again.

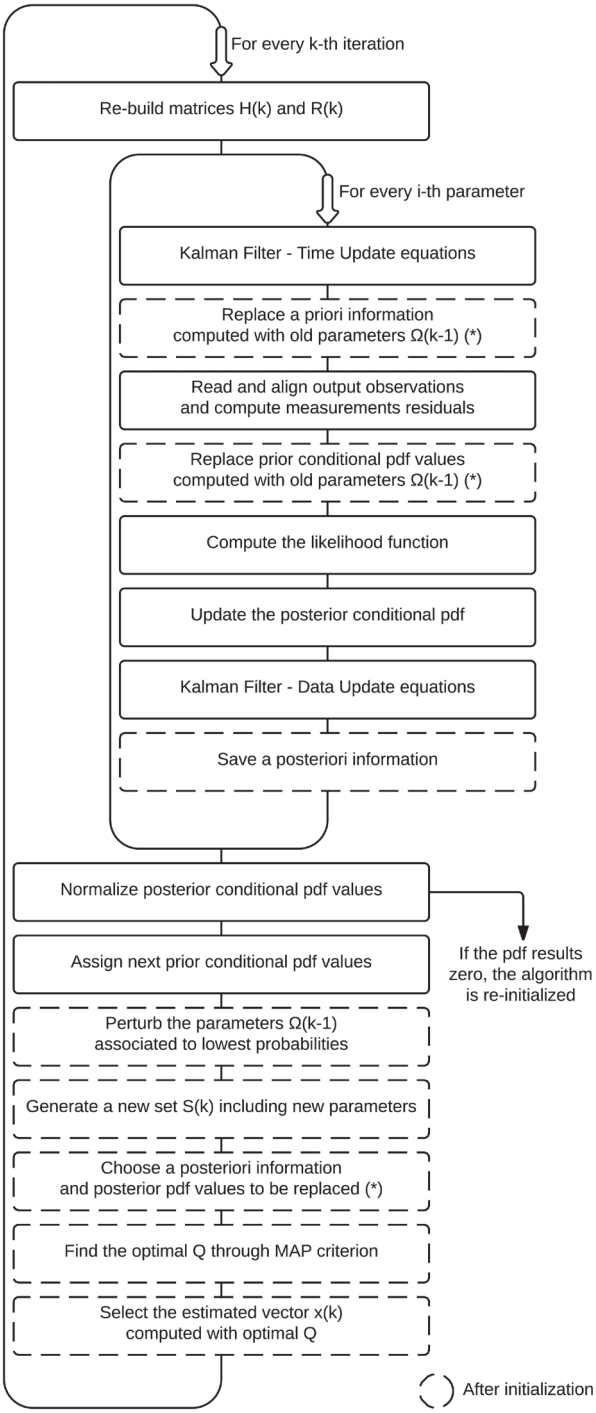

Figure 3 Algorithm flowchart

3) Algorithm phases: at first, the algorithm enters an initialization phase to train the conditional posterior probability distribution through the Bayesian approach, without updating the grid of parameters and thus keeping the first set S_0. The length of this starting period depends on the dynamic system order and the available measured data.

Afterwards, the iterative generation of new sets of state noise covariances is also enabled in order to improve the search for the maximum by the MAP criterion. Since parameters with high posterior pdf are desired, those with low probability are suitably replaced at each time step.

The optimization of the matrix **Q** therefore aims at identifying and selecting the current optimal (i.e. best possible) estimate among all the possible state vectors $\hat{\mathbf{x}}$ that are computed through parallel EKFs.

We implemented an algorithm that is an improved version of the recursive estimation method described in [6]. Indeed, we devised a mechanism to prevent the probabilities of all the possible noise covariances from being nullified when the deterministic model undergoes a fast change in the measured dynamics, as it may happen with high speeds along critical trajectories. If the conditional posterior pdf results to be zero for each point of the parametrization grid, the initialization phase is run again and a new probability distribution shape is then re-formed.

The iterative operation of the algorithm we used is summarized in the diagram of Fig. 3. The static configuration (e.g. the transition model, initial conditions, etc.) is omitted as it is illustrated in previous sections.

4 NUMERICAL RESULTS

Previous sections describe in detail the deterministic and stochastic properties of the model we assume for numerical simulations.

The overall performance of the presented navigation system is evaluated by simulating the tracking of a fast-moving vehicle on different trajectories as well as on a whole circuit. In this regard, the chosen figure of merit is the Root Mean Square Error (RMSE) of the position estimates that are computed by our quasi-tight GNSS/INS implementation based on EKF.

In order to verify the benefit of recursively adapting the state noise covariance matrix, the RMSE is calculated both with and without the proposed optimization process and parallel estimation.

For all the tests, the simulations are repeated 100 times sweeping through the following initial logarithmic parametrization:

$$\grave{\mathbf{U}}_0 = (0.0010, 0.0017, 0.0028, 0.0046, 0.0077, 0.0129, 0.0215, 0.3590, 0.0599, 0.1000) \quad \textbf{(27)}$$

The simulation configuration is briefly characterized as follows. The specific parameters that shape the uncertainty affecting the output observations are listed in Table 1, where $\mathbf{e}_\alpha$ is the error vector on the measurement α. We choose them to comply with the common specifications of receivers and inertial sensors.

Then, we consider an update frequency factor of 10 between the measured data coming from the GNSS and the INS.

As far as the estimation process is concerned, we assume to identify the exact transition model and observation model for the Kalman filter. This means the deterministic information are known.

A. Single racetracks

Four different types of trajectories are generated, each one has a simulation time of 10 seconds, as shown in Fig. 4, 5, 6, and 7. The aim of these tests is to separately analyze the algorithm efficiency while tracking the basic motions of a particle-like vehicle.

The GNSS/INS estimation process is run with two configurations: a recursively optimized matrix $\mathbf{Q}_{opt}$ based on parallel filtering and a single filter with fixed minimal noise covariance matrix that is defined as:

$$\mathbf{Q}_{min} = \mathbf{Q}(\Omega^1) = \mathbf{Q}(0.001) \quad \textbf{(28)}$$

Table 1 First order statistics of measurement errors

	μ	σ
e_X, e_Y	0	10 m
e_{GNSS}, e_{INS}	0	1 m/s
$e_{a_{x_{body}}}$, $e_{a_{y_{body}}}$	0	0.03 m/s^2
e_θ	0	0.044 rad

Table 2 Single racetracks results

	$RMSE(\hat{\mathbf{Q}}_{opt})$		$RMSE(\mathbf{Q}_{min})$	
	X	Y	X	Y
1) $a_x = 9.4\ m/s^2$	0.46 m	0.2 m	1.92 m	0.3 m
2) $\|v\| = 20\ m/s$	0.98 m	0.58 m	9.98 m	11.64 m
3) $\|v\| = 10\ m/s$	0.64 m	0.35 m	7.07 m	6.1 m
4) $\|v\| = 10\ m/s$	1.28 m	1.88 m	15.47 m	12.58 m

In other words, we compare the positional accuracy of the optimizing technique with those achieved with minimum state noise, which hence is associated to a well-identified deterministic model. The constants characterizing the kinematic equations and the RMSE values along the *X* and *Y* axes for both the configurations are reported in Table 2. The obtained results demonstrate that adapting the noise covariance enhances the average performance in terms of tracking accuracy, even if there is just a little uncertainty left on the state, which already represents an advantageous situation. In the simplest case of a linear motion, the RMSE is reduced by a factor of about 4, but the improvement significantly grows as trajectory become more intricate.

Whenever the transition and observation models do not fit the reality, optimizing the filter statistic inputs is expected to be necessary. As far as the state is concerned, different degrees of uncertainty are investigated by examining the vehicle moving on a circuit, as discussed in the next paragraph.

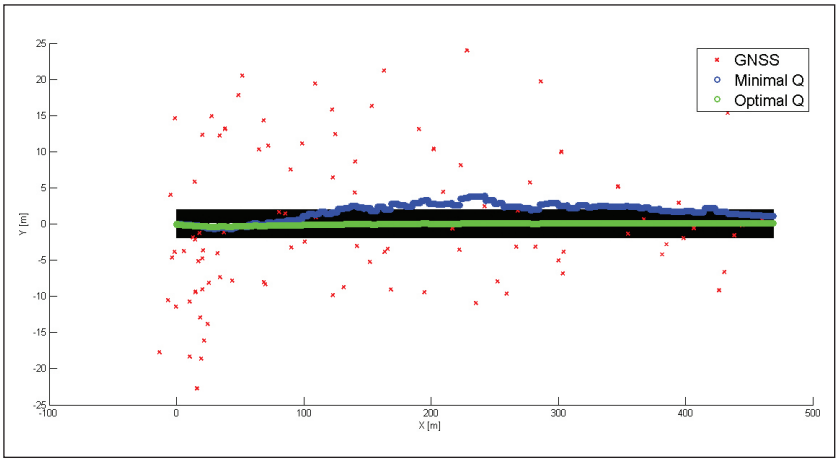

Figure 4 Example of straight line (1)

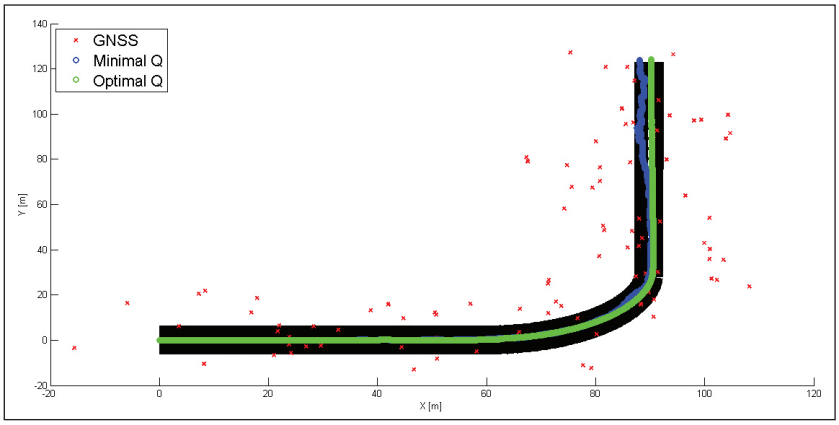

Figure 5 Example of quick turn (2)

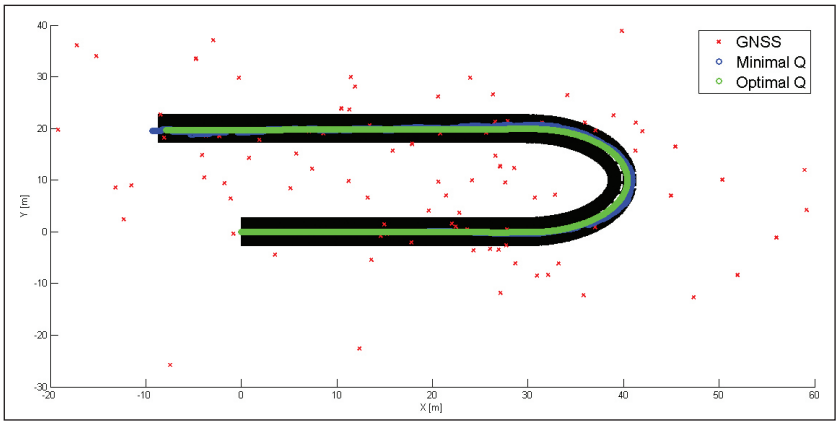

Figure 6 Example of circular hairpin (3)

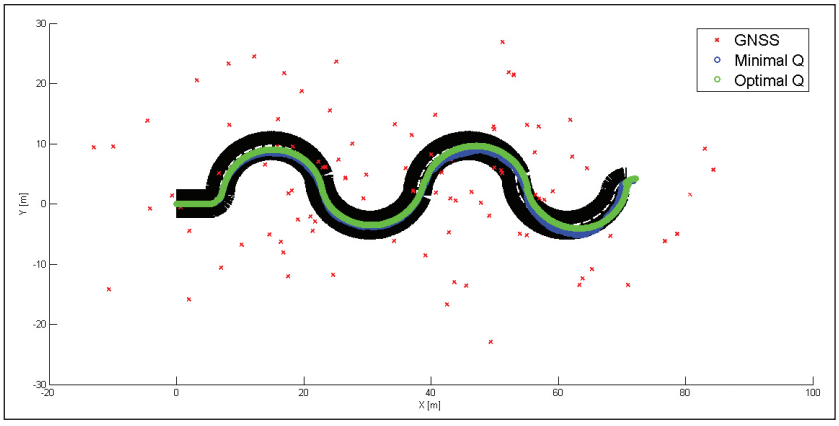

Figure 7 Example of slalom (4)

B. Complete track

A final test is carried out on a circuit clearly inspired inspiration from a typical scenario of a FSAE competition. The route is designed to assemble all the analyzed segments with either uniform accelerations or constant velocities, as depicted in Fig. 8.

In addition to the two previous configurations, we also consider the case of a matrix $\mathbf{Q}_{rand}$ that is randomly chosen in the set based on the parameters of Eq. (27). At each simulation, a different state noise covariance is thus entering the Kalman filter. This event could happen when the deterministic model is poorly characterized over time.

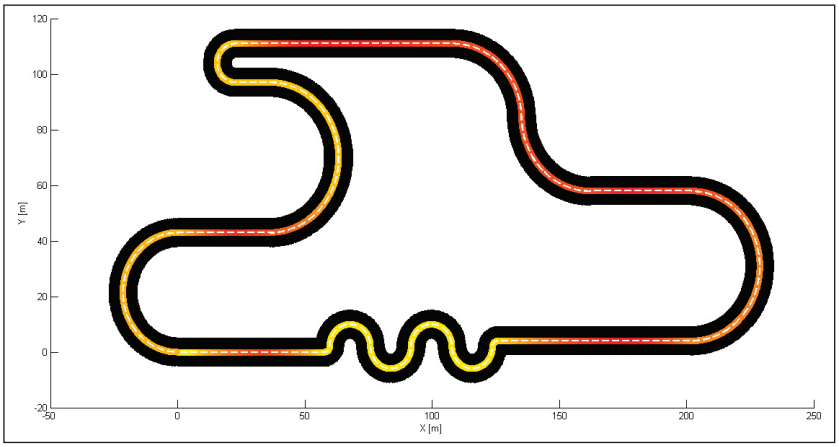

Figure 8 Circuit design with colored vehicle speed

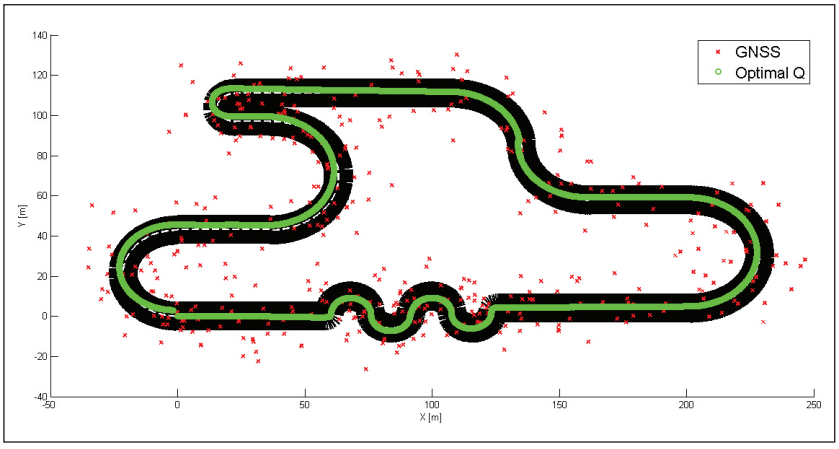

Figure 9 Optimized tracking on the circuit under test

The performance achieved after one lap of 44.06 seconds are summarized in Table 3. As expected, the best accuracy of about 1-2 meters is enabled by selecting $\mathbf{Q}_{opt}$ (Fig. 9), whereas $\mathbf{Q}_{min}$ ensures a decent precision on average, and a random $\mathbf{Q}_{rand}$ can cause the EKF to diverge from the actual positions. Here the improvements reaches again a factor of 4. These results show the great potentiality of implementing the presented optimization method for a quasi-tightly coupled GNSS/INS telemetry system as well as other automotive applications.

Table 3 Complete circuit results

$RMSE(\hat{\mathbf{Q}}_{opt})$		$RMSE(\mathbf{Q}_{min})$		$RMSE(\mathbf{Q}_{rand})$	
X	Y	X	Y	X	Y
.17 m	2.39 m	9.29 m	5.94 m	71.5 m	39.63 m

5 CONCLUSION

We explained and tested a quasi-tight GNSS/INS integration, which is aided by the recursive adaptation of the state noise covariance entering multiple parallel EKFs. Both the particular deterministic model description and the optimization algorithm feature some major changes with respect to the reference literature. We demonstrated that our implementation is capable of a very precise tracking in real-time, on the order of few meters, even in presence of large dynamics. To this end, we evaluated the localization of a vehicle moving at high speeds and we specifically considered the prototypes taking part to the Formula SAE competitions as our exemplary vehicular scenario.

A navigation system entailing our modified version of the optimization technique described is expected to address the challenging requirements imposed by advanced automobile applications. In this paper, the performance benefit is exploited for an accurate telemetry system, but many other applications are enabled by this algorithm.

Furthermore, we adopted a suitable mathematical formulation of the quasi-tight coupling, with the aim of allowing a cost-effective final integration of a receiver together with several inertial sensors.

Future plans regard the real-world development of such a low-cost high-precision GNSS/INS device mounting a commercial GPS receiver and Inertial Measurement Unit (IMU).

Moreover, the adaptation of the observation noise covariance matrix should be also investigated.

REFERENCES

[1] M.S. Grewal, L.R. Weill, and A.P. Andrews, *Global positioning systems, inertial navigation, and integration*. John Wiley & Sons, 2007.

[2] B. M. Scherzinger, "Quasi tightly coupled GNSS-INS integration process", Sept. 2 2014. US Patent 8,825,396.

[3] C. Palestini, L. Deambrogio, F. Bastia, and G.E. Corazza, "An insider view on tracking loops: A novel ultra-tight GNSS/INS hybridization approach", *IEEE/ION Position Location and Navigation Symposium (PLANS)*, pp. 1093–1099, May 2010.

[4] R.E. Kalman, "A new approach to linear filtering and prediction problems", *Journal of Fluids Engineering*, vol. 82, no. 1, pp. 35–45, 1960.

[5] H.W. Sorenson, "Least-squares estimation: from Gauss to Kalman", *IEEE Spectrum*, vol. 7, no. 7, pp. 63–68, July 1970.

[6] P. Matisko and V. Havlena, "Noise covariance estimation for Kalman filter tuning using bayesian approach and Monte Carlo", *International Journal of Adaptive Control and Signal Processing*, vol. 27, no. 11, pp. 957–973, 2013.

[7] B. J. Odelson, M. R. Rajamani, and J. B. Rawlings, "A new autocovariance least-squares method for estimating noise covariances", *Automatica*, vol. 42, no. 2, pp. 303–308, 2006.

[8] P. Matisko and V. Havlena, "Optimality tests and adaptive Kalman filter", *System Identification*, vol. 16, no. 1, pp. 1523–1528, 2012.

Technical co-sponsors

Media coverage